Neural coding of finger movements in human posterior parietal cortex and motor cortex

Thesis by

Charles Guan

In Partial Fulfillment of the Requirements for
the Degree of
Doctor of Philosophy

CALIFORNIA INSTITUTE OF TECHNOLOGY
Pasadena, California

2023
Defended March 29, 2023

Charles Guan
ORCID: 0000-0002-8040-8844

Acknowledgements

This work would not have been possible without the invaluable support and guidance of my mentors, Richard Andersen and Tyson Aflalo. I am thankful to Richard for welcoming me into the talented community of researchers he has created. Tyson encouraged me to approach research with creativity and critical thinking. His friendship showed that making sense of confusing data could be enjoyable.

Our lab's graduate student cohort, Isabelle Rosenthal, Kelly Kadlec, Sarah Wandelt, Whitney Griggs, created a kind and collaborative environment that helped me grow as a scientist. Special thanks to Kelly Kadlec for being a wonderful collaborator and office mate.

Many other lab members supported me throughout my time here. Jorge Gámez de Leon was always there to listen and provide insightful feedback. Xinyun Zou provided engaging new perspectives into our work. Sumner Norman, Carey Zhang, Matiar Jafari, Viktor Scherbatyuk, and Spencer Kellis warmly welcomed me to the lab during my rotation and helped me get started. Our lab manager, Kelsie Pejsa, managed countless administrative tasks, allowing us to focus on the core experiments and analysis. Our wider team of collaborators were a pleasure to work with: Ausaf Bari, Emily Rosario, Nader Pouratian, and Elena Amoruso.

JJ and NS, the study participants, were amazingly dedicated to our research. They are the true pioneers in this field. Working with JJ and NS was a highlight of my research experience, and I will miss our regular time together. They continuously pushed me to think about how we could advance the clinical applications of our work.

My program cohort became the friends who kept me going throughout the past five years. Kadina Johnston, David Goertsen, Shirin Shivaei, and many others kept me balanced with late-night hangouts and trips to the outdoors.

My family has continued to support me throughout my life. Mom and Dad instilled in me a sense of curiosity from a young age, and they sacrificed a lot for us. Darwin was the best childhood companion I could have had, and he inspires me to think about the bigger picture. Kayla's kindness reminds me to always think of others. My aunties, uncles, and cousins cheered me on during every endeavor.

Finally, I am grateful to have met my best friend and life partner at Caltech. Renée, your passion for science and your dedication to hard work continue to impress me. I have grown so much with you, and I am excited for our many adventures to come.

Abstract

We use our hands constantly in our everyday lives. This seemingly simple ability is disrupted in individuals with cervical spinal cord injuries. By circumventing injured signal pathways, brain-computer interfaces (BCIs) promise to enable such individuals to control artificial limbs for everyday use. However, existing BCI limb control remains coarse and inflexible, because we do not understand how the recorded neural activity relates to dexterous movement. As a result, BCI control in physical settings remains frustratingly difficult for paralyzed users. To improve dexterous BCI control, I studied the neural coding of individual finger movements in the posterior parietal cortex and motor cortex of tetraplegic participants. These regions are directly involved in dexterous hand movements and are candidates for BCI recording implants. Finger coding matched the correlation structure and dynamics of able-bodied usage, reflecting preserved motor circuits even after paralysis. Individual finger movements of each hand were coded in a factorized, correlated manner that still allowed decoding. Participants controlled artificial fingers with state-of-the-art accuracy. Finally, we studied the temporal dynamics of neural control to understand how existing models of neural activity extend to BCI control. These findings contribute to the understanding of human hand movements and advance the development of dexterous BCIs.

Published Content and Contributions

Guan, C., Aflalo, T., Zhang, C.Y., Amoruso, E., Rosario, E.R., Pouratian, N., Andersen, R.A., 2022. Stability of motor representations after paralysis. *eLife* 11. doi:10.7554/eLife.74478

- Contributions: Conceptualization, Methodology, Formal analysis, Funding acquisition, Investigation, Software, Data curation, Validation, Visualization, Writing
- Included here as Chapter 2

Guan, C., Aflalo, T., Kadlec, K., Gámez de Leon, J., Rosario, E.R., Bari, A., Pouratian, N., Andersen, R.A., 2022. Compositional coding of individual finger movements in human posterior parietal cortex and motor cortex enables ten-finger decoding. *medRxiv*. doi:10.1101/2022.12.07.22283227

- Contributions: Conceptualization, Methodology, Formal analysis, Funding acquisition, Investigation, Software, Data curation, Validation, Visualization, Writing
- Adapted here as Chapter 3

Table of Contents

List of Figures

Nomenclature

BA: Brodmann Area
BCI: brain-computer interface, also known as a brain-machine interface (BMI)
calibrate/train: calculate decoding algorithm's parameters based on a dataset
closed-loop: online
contralateral: side of the body opposite to the implant or condition
crossnobis: cross-validated squared Mahalanobis dissimilarity
decode: predict a variable from recorded neural activity
dynamics: temporal structure of neural activity patterns
factorized: explained by multiple independent factors, without their interaction effects
firing rate: frequency of action potentials
fMRI: functional magnetic resonance imaging
geometry: organization / distance structure of neural representations
ipsilateral: side of the body same as the implant or condition
JJ: one participant in our studies
M1: primary motor cortex
MC: motor cortex
neuroprosthetics: prosthetics using brain signals
NHP: non-human primate
NS: one participant in our studies
offline: analyzed after the experiment
online: decoded or analyzed in real-time during the experiment, often with visual feedback
open-loop: performed without direct feedback of the neural activity
PC-IP: junction of the postcentral (PC) and intraparietal (IP) sulci.
plasticity: ability of the nervous system to change or reorganize
population: a group of related neurons, often the group being recorded
PPC: posterior parietal cortex
RDM: representational dissimilarity matrix
representation: pattern of neural activity correlated with given content, and hypothesized to cause behavior
RSA: representational similarity analysis
SCI: spinal cord injury
SD: standard deviation
SEM: standard error of the mean
spike: action potential
spike sort: identify and cluster action potentials into putative single neurons
tetraplegia: paralysis affecting all limbs
tuned: hypothesized to represent specific information
unit: neuron
voxel: pixel in a three-dimensional space

1 Introduction

1.1 Neural prostheses to restore movement

Many of us take for granted our ability to interact and move through our physical surroundings. However, for more than 5 million Americans and millions more people globally, paralysis impairs this ability (Singh et al., 2014; Armour et al., 2016). Many of these cases stem from stroke, spinal cord injury, multiple sclerosis, or cerebral palsy. For many people living with paralysis, activities of daily living, such as feeding yourself or getting out of bed, are challenging or impossible without assistance (Anderson, 2004; Snoek et al., 2004; Collinger et al., 2013a).

One emerging class of medical devices that could assist paralyzed individuals are brain-machine interfaces (BMI), also known as brain-computer interfaces (BCI) or neural prostheses. BMIs record neural activity and decode motor intent to actuate an output device, such as a robotic arm. This technology could improve the quality of life of paralyzed individuals by restoring motor function and communication.

Early preclinical studies with non-human primate subjects have used BMIs to control computer cursors (Gilja et al., 2012) and robotic limbs (Carmena et al., 2003; Velliste et al., 2008). Since then, human tetraplegic participants in preliminary clinical trials have provided a number of case-study applications, including: keyboard typing (Jarosiewicz et al., 2015; Pandarinath et al., 2017; Nuyujukian et al., 2018; Willett et al., 2021), speech generation for people with anarthria (Anumanchipalli et al., 2019; Moses et al., 2021; Sarah K Wandelt et al., 2022; Willett et al., 2023)f, robotic arm control (Hochberg et al., 2012; Collinger et al., 2013c; Wodlinger et al., 2015), and controlling the individual's own paralyzed limb (Ajiboye et al., 2017). This wide range of applications and customizability will be necessary to match the diversity of BCI users' motor abilities and lifestyles.

Neural prostheses work with many underlying disability causes, in large part because they work by bypassing injured regions. In the example of spinal cord injuries, volitional motor commands from the brain no longer reach the intended effectors. However, motor regions of the brain remain intact, allowing neural prosthetic systems to record from the brain and output to a prosthetic limb. This brain-effector interface creates a distinct signal path, bypassing the injured spinal cord. Other motor disabilities may require circumventing different injured areas, such as a specific brain region for stroke patients.

1.2 Components of neural prosthetic systems

A neural prosthetic system consists of three core components: acquisition of neural activity ("recording"), translating neural activity to motor intent ("decoding"), and the output effector. My work has focused on neural decoding, understanding how the brain commands movement, and then designing algorithms to best separate that signal from the noise. Much of this dissertation is devoted to advances in this domain.

For the other two components, recording and output, my experiment design follows standard setups in this field. Regarding recording technology, here, I focus only on neuron action potentials recorded by intracortical microelectrode arrays. Action potentials and their consequent

neurotransmitter release are the main form of communication in the nervous system. Action potentials provide informative, low-latency input features and have controlled the most impressive typing and arm BMIs to date (Wodlinger et al., 2015; Willett et al., 2021). With regard to the design of the output effector, I demonstrate control of a keyboard interface and a discrete-selection robot hand, as well as the computer cursor task that has become a de facto standard in this field (Gilja et al., 2012; Jarosiewicz et al., 2015). Although I do not push the boundaries of recording and output effector technologies here, I hope that improved decoding can inspire more effective output designs in the future. These areas pose important challenges and are the work of many promising interdisciplinary collaborations, as reviewed elsewhere (Collinger et al., 2013b, 2018; Bockbrader, 2019; Kleinfeld et al., 2019; Luan et al., 2020).

1.3 Barriers to clinical usage

Despite impressive proof-of-concept demonstrations, neural prostheses face a number of barriers to clinical adoption. These issue categories range from scientific or technological to affordability and ethics. Here, I describe existing limitations and the scientific studies working to overcome them.

One of the core limitations is the relatively short usable device lifetime, a few years. This is a particular issue because the Utah array, the most widely available BMI implant with high signal quality, requires expensive, invasive neurosurgery. Signal quality degrades over time, so occasional reimplantation surgery would be necessary to keep recording quality at an operable level for longer periods. Ongoing materials science enhancements, such as flexible electrodes, may improve the electrodes' lifetimes while also reducing the foreign body response that obstructs the recorded neurons (Luan et al., 2020). In the meantime, neurotech companies are attempting to minimize surgery risk and cost through precise robotic surgery (Musk and Neuralink, 2019) or minimally invasive procedures (Ho et al., 2022).

A second limitation of existing BMIs is their relatively burdensome (re-)calibration requirements. Neural prosthetic systems are calibrated by learning a mapping from neural activity to intended movement. Calibration can take more than 5 minutes for 2-D point-and-click (Jarosiewicz et al., 2015) and up to 25 minutes for a prosthetic arm (Collinger et al., 2013c; Wodlinger et al., 2015). Calibration time quickly multiplies if we also want to dissociate confounding factors like hand position or visual responses from intended movement velocity, as described above. Moreover, the relationship between neural activity to intended movement can change over the time-scale of hours or days, due to electrodes shifting or changes in neurons' baseline firing rates and tuning properties (Chestek et al., 2011; Perge et al., 2013; Nuyujukian et al., 2014). The change in mapping, from neural activity to intent, degrades the performance of previously calibrated decoders. Without recalibration, neural prosthetics become less usable for patients over time. However, recalibration disrupts usage, limiting BMI usefulness (Huggins et al., 2015). To minimize disruption, it is imperative to shorten the calibration routine while still learning an accurate, long-term mapping from neural activity to intended movement. BMI researchers have proposed methods to extend the time between recalibrations, including: self-supervised retraining (Jarosiewicz et al., 2015), manifold alignment (Degenhart et al., 2020; Dabagia et al., 2022; Karpowicz et al., 2022; Ma et al., 2022), and extracting longer-lasting features from broadband data (Flint et al., 2013; Haghi et al., 2021).

A final limitation is the lack of control over physical effectors. Despite the field's interest in communication (Moses et al., 2021; Willett et al., 2021) and arm reaching (Hochberg et al., 2012;

Collinger et al., 2013c), no studies have developed prosthetic controllers that can interact with physical objects robustly enough to assist patients in their day-to-day activities. Restoring hand function is a top priority for people with tetraplegia (Anderson, 2004; Snoek et al., 2004; Collinger et al., 2013a). In particular, dexterous control of individual fingers is essential for daily activities such as opening doors, feeding oneself, and dressing. However, control of BMI hands remains coarse (Collinger et al., 2013c; Hotson et al., 2016), because we do not yet understand how the recorded brain signals relate to intended hand movements. To compare with another movement category, reaching studies have described how multiple factors can modulate neural activity (Omrani et al., 2017): movement direction (Georgopoulos et al., 1982), posture (Aflalo and Graziano, 2006), sensory feedback (Scott, 2016), and effector dynamics (Shadmehr et al., 2010; McNamee and Wolpert, 2019; Kalidindi et al., 2021). Hand movements involve different neural processes from arm reaching (Suresh et al., 2020; Sobinov and Bensmaia, 2021), so we are just beginning to understand how the brain integrates the multitude of factors for hand movements. Some work has been done to understand grasping in preclinical non-human primate models (Schaffelhofer and Scherberger, 2016; Michaels et al., 2020) and even basic human grasps (Gallivan and Culham, 2015; Klaes et al., 2015; Sarah K Wandelt et al., 2022). These studies usually narrowed their scope to offline analysis of a few basic grasp templates, limiting their applicability to everyday settings. Future studies should eventually allow flexible control to pick up and manipulate a diverse array of objects. To improve dexterous decoding, we need to better understand the neural principles of hand movements, and this challenge motivates my dissertation research.

1.4 Dissertation outline

In this dissertation, I study the cortical coding of finger movements and apply these findings to improve neuroprosthetic control. By understanding the fundamentals of dexterous movements, I believe that we can advance neural decoding to the point that BMIs can substantially improve quality of life of tetraplegic individuals. This dissertation is organized as follows:

The remainder of **Chapter 1** summarizes the relevant prior research on the neural control of hand movements.

Chapter 2 examines whether and how individual finger movements are encoded in the posterior parietal cortex. The neural coding principles followed the kinematics of able-bodied natural hand use, even years after the participant was paralyzed. These representations are stable after paralysis and throughout BMI usage, allowing us to tap into the pre-existing neural code.

Chapter 3 extends our study of finger movements to include both the posterior parietal cortex and motor cortex. A participant used neural signals in both regions to control finger movements at a state-of-the-art level. I compare the information content of both regions, calculating what improvements in recording quality would be necessary to control prosthetic fingers with high accuracy. Furthermore, I analyze finger movements of both hands and describe how their neural codes are correlated and factorized, which has important implications for bilateral neuroprosthetic control.

Chapter 4 considers the temporal dynamics of BCI finger movements. To better understand how short, corrective movements might differ from their sustained counterparts, I extended BMI movement durations to dissociate the movement-onset dynamics from the relatively stationary movement intent. I found that we could separate BCI movements into phases: initial onset, sustained

intent, and offset. This work merges the classical understanding of movement parameter representations with modern concepts of the brain as a dynamical system.

Chapter 5 concludes with a summary of our results and their broader impacts. I discuss promising future directions that could improve the functional utility of BMIs. These directions take advantage of both our improved neuroscientific understanding and parallel technological advances.

1.5 Neural coding of hand movements

1.5.1 Manual dexterity

The human hand is unique in its dexterity (Sobinov and Bensmaia, 2021). Humans can learn to solder microscopic components to a circuit board or execute hundreds of video game actions per minute. Even everyday hand movements require complex coordination. We make take these skills for granted, but the difficulty of everyday actions is clear when we try to teach a robot to handle objects (Billard and Kragic, 2019) or when observing a young toddler trying to pick up a grain of rice. Our dexterity is further highlighted by the fact that humans can move individual fingers more independently than other primates (Schieber, 1991; Häger-Ross and Schieber, 2000). This feature, along with our fully opposable thumbs, allows flexible control over a variety of objects.

Despite this unique flexibility, hand movements do exhibit structure as well. Although the thumb moves quite independently, the other fingers tend to move in a coordinated manner (Schieber, 1991; Häger-Ross and Schieber, 2000). This in part reflects biomechanical coupling, both passive and active, between the other fingers (Lang and Schieber, 2004a). These biomechanical patterns can also be reflected in neural patterns, as I discuss further in Section 1.5.2 and Chapter 2.

1.5.2 Neural control of hand movements

Our impressive hand dexterity requires a coordinated effort across neural systems. Volitional hand movements involve the motor cortex, parietal cortex, cerebellum, basal ganglia, corticospinal tracts, and peripheral nerves, as well as sensory regions. Here, we specifically review the roles of the motor cortex and posterior parietal cortex, given their central roles in hand dexterity.

The primary motor cortex (M1) plays a crucial role in dexterous hand control, as demonstrated by several lines of evidence. More than 20% of M1 generates finger movements in response to electrical stimulation, even though M1 contains representations for the entire body and the hand only weighs 0.6% of body mass (Sobinov and Bensmaia, 2021). Functional magnetic resonance imaging (fMRI) studies find selective activation of the primary motor cortex and primary somatosensory cortex (S1) in response to finger movements (Allison et al., 2000; Ejaz et al., 2015). Lesions of M1 or its descending pyramidal tracts disrupt grasping and permanently disrupt individual finger movements (Lawrence and Kuypers, 1968; Lang and Schieber, 2003, 2004b). In addition, the corticomotoneuronal cells, a subpopulation of M1, synapse directly onto spinal motoneurons innervating upper limb muscles, connecting M1 directly to fine muscle control (Rathelot and Strick, 2009). This evidence positions M1 as a central node for dexterous hand control.

M1 is known to be coarsely somatotopic, with overlapping regions of M1 controlling movements of specific body parts. In the hand area, the somatotopy is even more coarse, with small cortical areas mixing between different fingers and even control of the wrist (Schieber and Hibbard, 1993; Schieber, 2001). Neurons in the hand region of M1 code for a combination of finger posture

(Goodman et al., 2019) and velocity signals (Nason et al., 2021), although other factors could also influence their modulation.

Our understanding of human M1 largely comes from studies of non-human primate subjects, and we are still in the early stages of understanding how these studies translate to human M1. The commonly cited hand region of human M1 is the precentral gyrus area known as the "hand knob," due to its common visual similarity to the Greek letter Ω (Yousry et al., 1997). However, a recent study found that the hand knob codes movements in a manner more consistent with the premotor cortex, arguing that the hand region of M1 may lie deeper in the sulcus (Willett et al., 2020). An alternative explanation may be that the hand knob is more heterogeneous than originally thought (Simone et al., 2021), with certain areas still homologous to the non-human primate M1.

Primate manual dexterity is supported by a distributed set of nervous systems beyond M1, such as the posterior parietal cortex (PPC). The posterior parietal cortex (PPC) plays a central role in sensorimotor integration, with PPC regions representing visual stimulus locations (Andersen et al., 1985), eye movements (Andersen et al., 1987), task context (Gail et al., 2009), planned reaches (Snyder et al., 1997), and object grasping (Murata et al., 2000; Schaffelhofer and Scherberger, 2016). Lesions of different PPC subregions can lead to diverse behavioral deficits, including optic ataxia (inability to grasp objects under visual guidance) (Andersen et al., 2014) and loss of awareness of body parts (Whitlock, 2017). The PPC is also involved in fine finger dexterity. Electrical stimulation of PPC subregions can induce individual finger movements (Cooke et al., 2003; Rathelot et al., 2017; Baldwin et al., 2018), and single neurons respond to tactile stimuli at individual fingers (Seelke et al., 2012).

The PPC transforms information from the visual cortex into motor plans. Visual processing is essential to interacting with the world, to know where and how to move. The anterior intraparietal area (AIP) within PPC has been identified as important for hand dexterity for non-human primates. AIP processes visual information about object shape and position and transforms that information into grip type (Schaffelhofer and Scherberger, 2016) to send it to the ventral premotor cortex (PMv) and onto M1 (Figure 1.1). Reaching is processed through a separate pathway: the parietal reach region (PRR), then to the dorsal premotor cortex (PMd), and then to M1. Consequently, when AIP is inactivated, subjects can still reach normally, but they fail to preshape grasps (Gallese et al., 1994). Recent work has found that some AIP corticospinal neurons synapse onto spinal interneurons that connect directly to hand motor neurons (Rathelot et al., 2017). Furthermore, electrical microstimulation of AIP elicits wrist and finger movements (Rathelot et al., 2017; Baldwin et al., 2018), indicating that AIP supports fine manual control. Functional magnetic resonance imaging (fMRI) studies have identified a potential homolog in humans in the anterior intraparietal sulcus (aIPS) (Gallivan and Culham, 2015). Human electrophysiology studies, including my own, usually record only the gyri around aIPS. These studies find slightly different coding schemes from AIP and find that the usual anatomical markers (intersection between postcentral and intraparietal sulci, here abbreviated PC-IP) can vary by subject. Therefore, it remains unclear exactly how NHP studies inform the coding principles of the area around human aIPS.

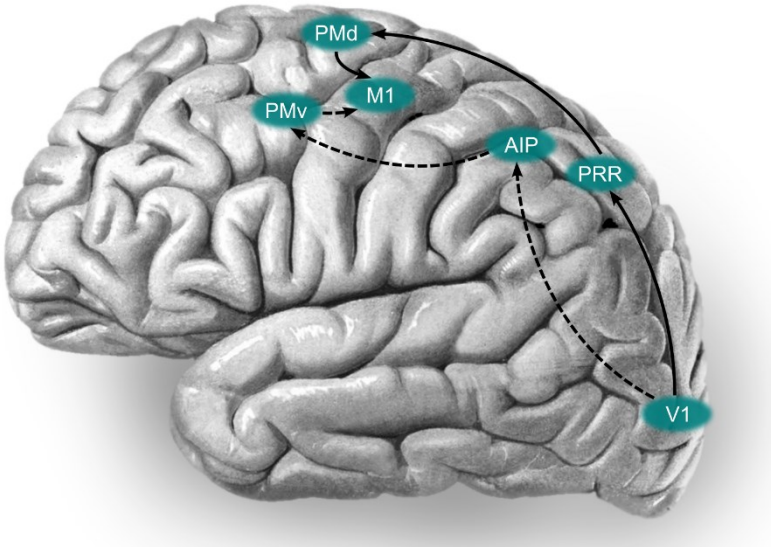

Figure 1.1 Cortical control of visually guided hand movements.
The anterior intraparietal area (AIP) transforms object information from the visual cortex (V1) into the appropriate grasp type to send on to the ventral premotor area (PMv) and then to the primary motor cortex (M1). The parietal reach region (PRR) transforms object location into a reach plan to send on to the dorsal premotor area (PMd) and then to M1. These regions have been studied most thoroughly in non-human primates, but their putative homologs are highlighted on this human brain.
Adapted from Frank Gaillard, Radiopaedia.org, used under CC BY-NC-SA.

1.5.3 Somatosensory feedback for object manipulation

Precise object manipulation relies on sensory feedback. Loss of proprioception, which tracks our own posture and movements, impairs multi-joint movements like reaching, especially when vision is obstructed (Ghez et al., 1995; Sainburg et al., 1995). Loss of touch, which describes the objects we interact with, impairs fine manipulation, such as striking a match (Johansson and Flanagan, 2009). Here, we review somatosensory feedback and how it relates to hand dexterity and BMIs.

Tactile sensation is generated by four sets of mechanoreceptors in the palm of the hand, responding to skin vibrations, texture, pressure, and stretch. Proprioception mainly emerges from thousands of muscle spindles that convey posture and Golgi tendon organs that convey force (Sobinov and Bensmaia, 2021). These signals are sent via nerve fibers to cuneate nucleus in the brainstem, on to the ventral posterolateral nucleus of the thalamus, and then to the primary somatosensory cortex.

The primary somatosensory cortex (S1) is located on the postcentral gyrus, just posterior to M1 and just anterior to PPC. S1 is somatotopic, forming a defined map of body parts each subpopulation responds to. Like in M1, the hand area of S1 takes up a large area (20%) of the primary somatosensory cortex (Sobinov and Bensmaia, 2021), underscoring the utility of rich tactile feedback for manual dexterity. Within S1's hand region, finger representations are separate to allow distinct percepts per finger (Pons et al., 1985). These tactile signals are tightly coupled with M1

circuits, with strong tactile connections to the hand area of M1, while the arm region receives stronger proprioceptive signals (Friel et al., 2005).

Tactile feedback is essential for manual dexterity during all phases of object manipulation (Johansson and Flanagan, 2009; Sobinov and Bensmaia, 2021). First, when reaching to grasp an object, initial contact starts the transition from reaching to grasping. Second, when lifting the object, information on mass and friction enables us to apply the appropriate grip force. This force margin allows us to hold the object securely without crushing it (Billard and Kragic, 2019). Third, tactile signals provide quick information on perturbations and how to accommodate them, such as an accidental bump into the table when feeding. Fourth, sensory input informs our predictive model of object dynamics, so that we can lift the object more precisely next time. To support manual dexterity, tactile processing is enhanced during active object manipulation, when compared to passive perception (Pruszynski et al., 2018).

For individuals with spinal cord injuries, sensory signals from the hand do not reach the cortex. Most existing BMI systems cannot provide somatosensory input, so BMI users must rely on visual feedback. While vision provides some utility, it does not replace the richness and speed of tactile and proprioceptive feedback (Ghez et al., 1995). This is clear when observing individuals with intact motor control yet disrupted sensory pathways, who are unable to perform many simple actions (Miall et al., 2019). Additionally, touch provides far more robust information about contact timing, texture, mass, and vibration than vision does.

To overcome this barrier, bidirectional BMI systems aim to restore both motor control and somatosensory input (Collinger et al., 2018). The most promising directions currently use intracortical microstimulation (ICMS) in S1 to elicit isolated sensations in the arm, hand, or fingers (Flesher et al., 2016; Armenta Salas et al., 2018). The localized sensory input improves grasping by signaling object contact (Flesher et al., 2021). However, multiplexing touch input and preventing interference with motor decoding have been difficult. These challenges remain for future studies to tackle, and they may also inspire alternative paradigms of overcoming the lack of somatosensory feedback.

Sometimes, the lack of sensory feedback can actually benefit basic neuroscience studies; we can decouple motor control and sensory feedback, allowing us to dissociate these processes in our experiments (Golub et al., 2016). In Chapter **4**, I use this paradigm to study how motor control changes over the time course of a movement. We can use these paradigms to better understand the motor and sensory systems, tuning these parameters in a way not possible with able-bodied subjects, to advance design of neuroprosthetic systems.

2 Stability of motor representations after paralysis

2.1 Summary

Neural plasticity allows us to learn skills and incorporate new experiences. What happens when our lived experiences fundamentally change, such as after a severe injury? To address this question, we analyzed intracortical population activity in the posterior parietal cortex (PPC) of a tetraplegic adult as she controlled a virtual hand through a brain-computer interface (BCI). By attempting to move her fingers, she could accurately drive the corresponding virtual fingers. Neural activity during finger movements exhibited robust representational structure similar to fMRI recordings of able-bodied individuals' motor cortex, which is known to reflect able-bodied usage patterns. The finger representational structure was consistent throughout multiple sessions, even though the structure contributed to BCI decoding errors. Within individual BCI movements, the representational structure was dynamic, first resembling muscle activation patterns and then resembling the anticipated sensory consequences. Our results reveal that motor representations in PPC reflect able-bodied motor usage patterns even after paralysis, and BCIs can re-engage these representations to restore lost motor functions.

2.2 Introduction

A central question in neuroscience is how experience affects the nervous system. Studies of this phenomenon, plasticity, were pioneered by Hubel and Wiesel, who found that temporary visual occlusion in kittens can induce lifelong reorganization of the visual cortex (Hubel and Wiesel, 1970). Their results demonstrated that the developing brain, rather than being genetically preprogrammed, is surprisingly malleable to external inputs.

Subsequent studies showed that other brain regions are also plastic during early development, but it is unclear how plastic the nervous system remains into adulthood. Visual occlusion in adult cats does not reorganize the visual cortex, and lesion studies of the adult visual cortex have arrived at competing conclusions of reorganization and stability (Gilbert and Wiesel, 1992; Smirnakis et al., 2005; Keck et al., 2008; Baseler et al., 2011). A similar discussion continues regarding the primary somatosensory cortex (S1). Classical studies posited that amputation and spinal cord injury modify the topography of body parts in S1, with intact body parts taking over cortical areas originally dedicated to the amputated part (Merzenich et al., 1984; Pons et al., 1991; Qi et al., 2000; Jain et al., 2008). However, recent human neuroimaging studies (Makin and Bensmaia, 2017; Kikkert et al., 2021) and sensory BCI studies (Flesher et al., 2016; Armenta Salas et al., 2018) have challenged the extent of this remapping, arguing that sensory topographies largely persist even after complete sensory loss. Thus, the level of plasticity in the adult nervous system is still an ongoing investigation.

Understanding plasticity is necessary to develop brain-computer interfaces (BCIs) that can restore sensorimotor function to paralyzed individuals (Orsborn et al., 2014). First, paralysis disrupts movement and blocks somatosensory inputs to motor areas, which could cause neural reorganization (Pons et al., 1991; Jain et al., 2008; Kambi et al., 2014). Second, BCIs bypass supporting cortical, subcortical, and spinal circuits, fundamentally altering how the cortex affects movement. Do these

changes require paralyzed BCI users to learn fundamentally new motor skills (Sadtler et al., 2014), or do paralyzed participants use a preserved, pre-injury motor repertoire (Hwang et al., 2013)? Several paralyzed participants have been able to control BCI cursors by attempting arm or hand movements (Hochberg et al., 2006, 2012; Collinger et al., 2013c; Gilja et al., 2015; Bouton et al., 2016; Ajiboye et al., 2017; Brandman et al., 2018), hinting that motor representations could remain stable after paralysis. However, the nervous system's capacity for reorganization (Pons et al., 1991; Jain et al., 2008; Kambi et al., 2014; Kikkert et al., 2021) still leaves many BCI studies speculating whether their findings in tetraplegic individuals also generalize to able-bodied individuals (Flesher et al., 2016; Armenta Salas et al., 2018; Stavisky et al., 2019; Willett et al., 2020; Fifer et al., 2021). A direct comparison, between BCI control and able-bodied neural control of movement, would help address questions about generalization.

Temporal dynamics provide another lens to investigate neural organization and its changes after paralysis. Temporal signatures can improve BCI classification (Willett et al., 2021) or provide a baseline for motor adaptation studies (Stavisky et al., 2017a; Vyas et al., 2018). Notably, motor cortex activity exhibits quasi-oscillatory dynamics during arm reaching (Churchland et al., 2012). More generally, the temporal structure can depend on the movement type (Suresh et al., 2020) and the recorded brain region (Schaffelhofer and Scherberger, 2016). In this study, we recorded from the posterior parietal cortex (PPC), which is thought to compute an internal forward model for sensorimotor control (Wolpert et al., 1998; Desmurget and Grafton, 2000; Mulliken et al., 2008a; Li et al., 2022). A forward model overcomes inherent sensory delays to enable fast control by predicting the upcoming states. If PPC activity resembles a forward model even after paralysis, this would suggest that even the temporal details of movement are preserved after injury.

Here, we investigate the neural representational structure of BCI finger movements in a tetraplegic participant. In able-bodied individuals, the cortical representational structure of finger movements follows the natural statistics of movements (Lillicrap and Scott, 2013; Ejaz et al., 2015). In a BCI task, the experimenter can instruct movement patterns unrelated to biomechanics or before-injury motifs. In this study, we tested whether the neural representational structure of BCI finger movements by a tetraplegic individual matches that of able-bodied individuals performing similar, overt movements, or whether the structure follows the task's optimal representational structure (Bonnasse-Gahot and Nadal, 2008). If the BCI finger organization matches that of able-bodied movement, participants likely activated pre-injury motor representations, indicating that motor representations were preserved after paralysis.

We report that the neural representational structure of BCI finger movements in a tetraplegic individual matches that of able-bodied individuals. This match was stable across sessions, even though the measured representational structure contributed to errors in the BCI task. Furthermore, the neural representational dynamics matched the temporal profile expected of a forward model in able-bodied individuals, first resembling muscle activation patterns and then resembling expected sensory outcomes. Our results suggest that adult motor representations in PPC remain even after years without use.

2.3 Results

2.3.1 Intracortical recordings during finger flexion

We recorded single and multi-neuron activity (95.8 +/- s.d. 6.7 neurons per session over 10 sessions) from participant NS while she attempted to move individual fingers of the right hand. We recorded from a microelectrode array implanted in the left (contralateral) posterior parietal cortex (PPC) at the junction of the postcentral and intraparietal sulci (PC-IP, Supplementary Figure 2.1). This region is thought to specialize in the planning and monitoring of grasping movements (Orban and Caruana, 2014; Gallivan and Culham, 2015; Klaes et al., 2015; Andersen et al., 2019).

Each recording session started with an initial calibration task (Supplementary Figure 2.2, Methods). On each trial, we used a computer screen to present a text cue (e.g., "T" for thumb), and the participant immediately attempted to flex the corresponding finger, as though pressing a key on a keyboard. Because participant NS previously suffered a C3-C4 spinal cord injury resulting in tetraplegia (AIS-A), her movement attempts did not generate overt motion. Instead, participant NS attempted to move her fingers as though she was not paralyzed.

These attempted movements resulted in distinct neural activity patterns across the electrode array. To enable BCI control, we trained a linear classifier (Methods) to identify finger movements from neural firing rates. The participant subsequently performed several rounds of a similar finger flexion task, except that 1) the trained classifier now provided text feedback of its predicted finger and 2) the task randomized the visual cue location (Figure 2.1a and Methods). We repeated this online-control finger flexion task over multiple sessions (408 +/- s.d. 40.8 trials/session over 10 sessions) and used this data for our offline analyses. Participant NS also performed a control task, identical in structure except that she attended to cues without performing the instructed movements.

2.3.2 Accurately decoding fingers from PPC single-neuron activity

High classification accuracy during online control (86% +/- s.d. 4% over 10 sessions; chance = 17%) (Figure 2.1b) and offline cross-validated classification (92% +/- s.d. 2%; Supplementary Figure 2.3a) demonstrated that the finger representations were reliable and linearly separable. During the calibration task, cross-validated classification was similarly robust (accuracy = 96% +/- s.d. 3%; Supplementary Figure 2.3b).

At the single-neuron level, most (89%) neurons were significantly tuned to individual finger press movements (significance threshold: $P < 0.05$, FDR corrected) (Supplementary Figure 2.4). The example neurons in Figure 2.1c-f show that neurons could be tuned to one or more fingers and that tuning profiles could change in time.

To confirm that the observed neural responses could not be explained by visual confounds, we verified that we could not discriminate between fingers during the control task (Supplementary Figure 2.5). Furthermore, we could not decode the gaze location during the finger classification time window in the standard online-control task (Supplementary Figure 2.5). Thus, reliable finger representations emerged from the participant's movement attempts.

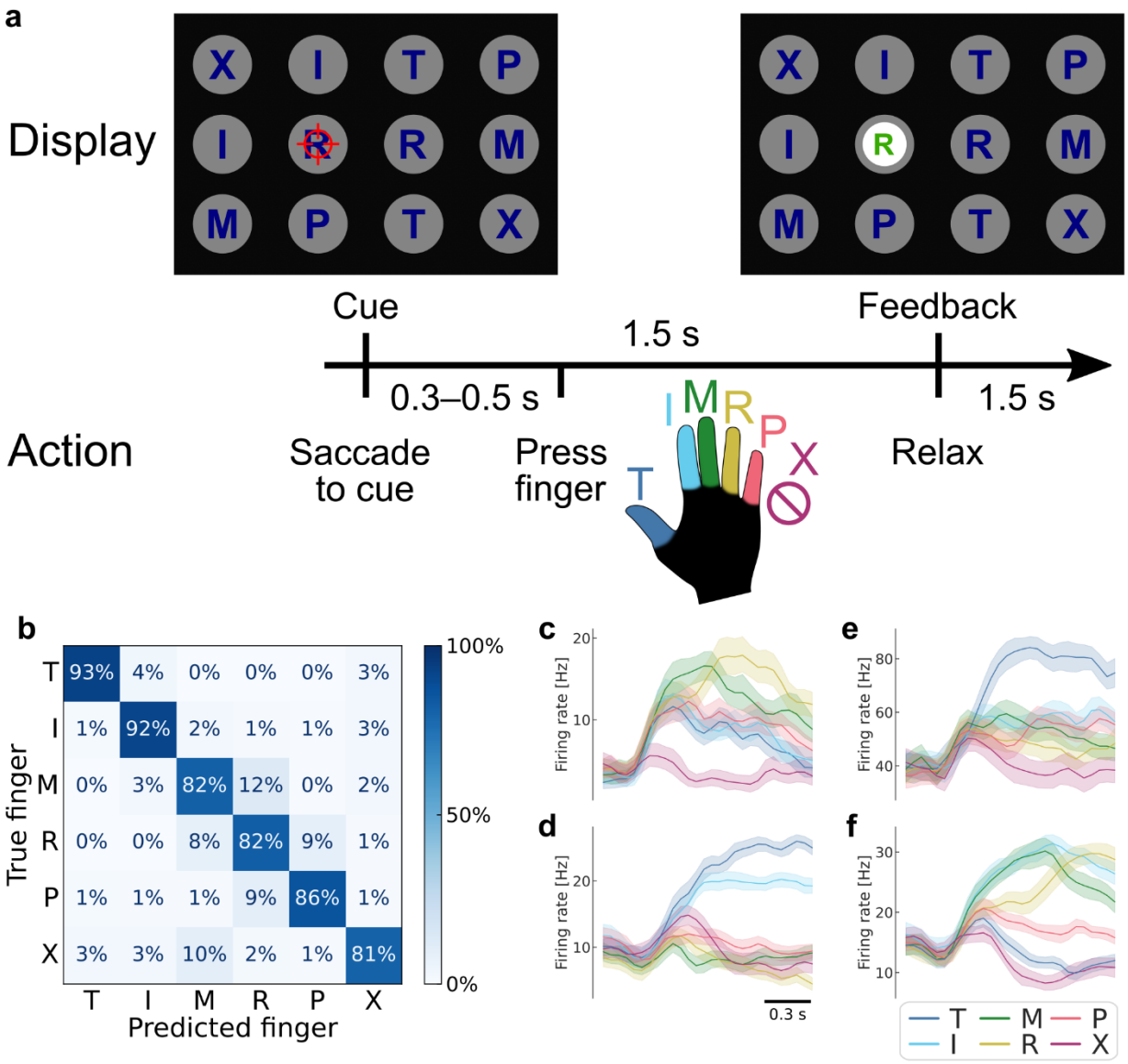

Figure 2.1 Robust brain-computer interface (BCI) control of individual fingers.
(**a**) Main finger flexion task. When a letter was cued by the red crosshair, the participant looked at the cue and immediately attempted to flex the corresponding digit of the right (contralateral) hand. We included a null condition "X," during which the participant looked at the target but did not move her fingers. Visual feedback indicated the decoded finger 1.5 seconds after cue presentation. To randomize the saccade location, cues were located on a grid (3 rows, 4 columns) in a pseudorandom order. The red crosshair was jittered to minimize visual occlusion.
(**b**) Confusion matrix showing robust in-session BCI finger control (86% overall accuracy, 4016 trials aggregated over 10 sessions). Each entry (*i*, *j*) in the matrix corresponds to the ratio of movement *i* trials that were classified as movement *j*.
(**c-f**) Mean firing rates for 4 example neurons, color-coded by attempted finger movement. Shaded areas indicate 95% confidence intervals (across trials of one session). Gaussian smoothing kernel (50-ms SD).

2.3.3 Finger representational structure matches the structure of able-bodied individuals

Having discovered that PC-IP neurons modulate selectively for finger movements, we next investigated how these neural representations were functionally organized and how this structure related to pre-injury movements. Here, we turned to the framework of representational similarity analysis (RSA) (Kriegeskorte et al., 2008a; Diedrichsen and Kriegeskorte, 2017). RSA quantifies neural representational structure by the pairwise distances between each finger's neural activity patterns (Figure 2.2a). These pairwise distances form the representational dissimilarity matrix (RDM), a summary of the representational structure. Importantly, these distances are independent of the original feature types (for example, electrode or voxel measurements), allowing us to compare finger organizations across subjects and across recording modalities (Kriegeskorte et al., 2008b).

We used RSA to test three hypotheses: 1) the BCI finger representational structure could match that of able-bodied individuals (Ejaz et al., 2015; Kieliba et al., 2021) (Figure 2.2b and Supplementary Figure 2.6), which would imply that motor representations did not reorganize after paralysis. This hypothesis would be consistent with recent fMRI studies of amputees, which showed that sensorimotor cortex representations of phantom limb finger movements match the same organization found in able-bodied individuals (Kikkert et al., 2016; Wesselink et al., 2019). We note that our able-bodied model was recorded from human PC-IP using fMRI, which measures fundamentally different features (millimeter-scale blood oxygenation) than microelectrode arrays measure (sparse sampling of single neurons). Another possibility is that 2) the participant's pre-injury motor representations had de-specialized after paralysis, such that finger activity patterns are unstructured and pairwise-independent (Figure 2.2c). However, this hypothesis would be inconsistent with results from fMRI studies of amputees' sensorimotor cortex (Kikkert et al., 2016; Wesselink et al., 2019). Lastly, 3) the finger movement representational structure might optimize for the statistics of the task (Lillicrap and Scott, 2013; Clancy et al., 2014). Our BCI task, as well as previous experiments with participant NS, involved no correlation between individual fingers, so the optimal structure would represent each finger independently to minimize confusion between fingers. In other words, the task-statistics hypothesis (3) would predict that, with BCI usage, the representational structure would converge towards the task-optimal, unstructured representational structure (Figure 2.2c).

Does the finger representational structure in a tetraplegic individual match that of able-bodied individuals? We quantified the finger representational structure by measuring the cross-validated Mahalanobis distance (Methods) between each finger pair, using the firing rates from the same time window used for BCI control. The resulting RDMs are shown in Figure 2.2d (average across sessions) and Supplementary Figure 2.7 (all sessions). For visual intuition, we also projected the representational structure to two dimensions in Figure 2.2e, which shows that the thumb is distinct, while the middle, ring, and pinky are close in neural space. We then compared the measured RDMs against the able-bodied fMRI and unstructured models, using the whitened unbiased RDM cosine similarity (WUC) (Diedrichsen et al., 2021). The measured representational structure matched the able-bodied representational structure significantly over the unstructured model ($P = 5.7 \times 10^{-5}$, two-tailed t-test) (Figure 2.2f), ruling out the de-specialization hypothesis (2). Our findings were robust to different choices of distance and model-similarity metrics (Supplementary Figure 2.8).

We note that we constructed the able-bodied fMRI model from the mean of PC-IP fMRI RDMs across multiple able-bodied participants (N = 29). Participant NS's average PC-IP RDM was

also statistically typical among the RDM distribution of individual able-bodied participants (permutation shuffle test, P = 0.55), in part because PC-IP fMRI RDMs were relatively variable across participants (Supplementary Figure 2.9).

We also compared the PC-IP BCI RDM with able-bodied fMRI motor cortex (MC) RDMs, which have been previously shown to match the patterns of natural hand use (Ejaz et al., 2015). The able-bodied MC and PC-IP fMRI finger organizations are similar in that they represent the thumb distinctly from the other fingers, but PC-IP represents each of the non-thumb fingers similarly while MC distinguishes between all five fingers (Supplementary Figure 2.6). Interestingly, PC-IP BCI finger representations matched the able-bodied fMRI finger representational structure in the motor cortex (MC) even better than that of able-bodied PC-IP (Supplementary Figure 2.10). The WUC similarity with the MC RDM was close to the noise ceiling (Methods), indicating that the MC RDM matches participant NS's data better than almost any other model (see Discussion).

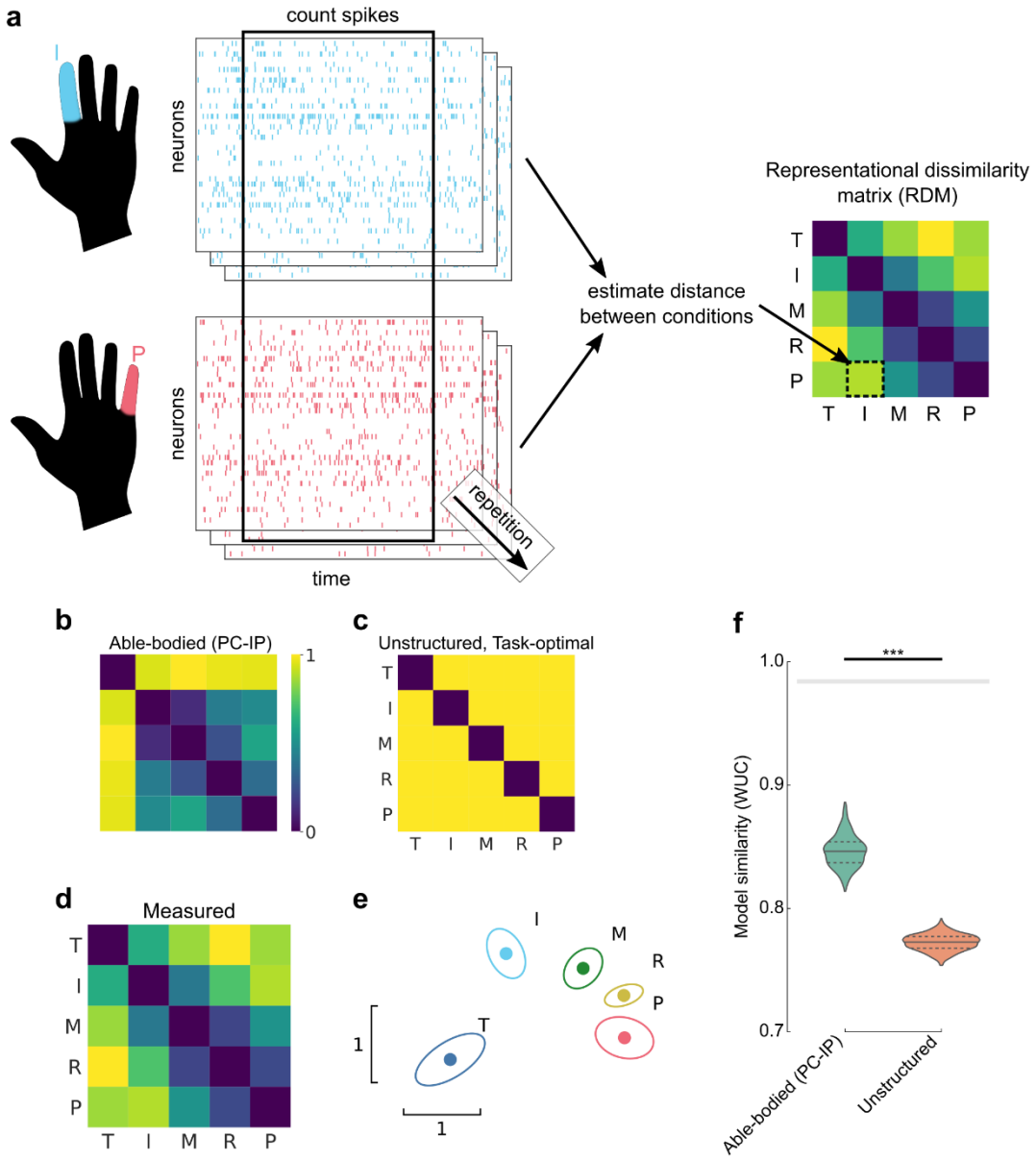

Figure 2.2. Representational structure during BCI finger control matches the structure of able-bodied individuals.

(**a**) To construct the representational dissimilarity matrix (RDM), a vector of firing rates was constructed for each trial. Repetitions were collected for each condition. Then, pairwise distances were estimated between conditions using a cross-validated dissimilarity metric. This process was repeated to generate an RDM for each session. We drop the No-Go condition (X) here to match previous finger studies (Ejaz et al., 2015; Kikkert et al., 2016).

(**b**) Representational structure hypothesized by the preserved-representation hypothesis: average PC-IP RDM for a finger-press task using fMRI in 36 able-bodied individuals (Ejaz et al., 2015; Kieliba et al., 2021). Max-scaled to [0, 1].

(**c**) Representational structure hypothesized by the de-specialization and task-optimal hypotheses: pairwise-equidistant RDM. Max-scaled to [0, 1].
(**d**) Finger representational structure measured in tetraplegic participant NS: cross-validated Mahalanobis distances (Methods) between neural activity patterns, averaged across 10 recording sessions. Max-scaled to [0, 1].
(**e**) Intuitive visualization of the distances in (d) using multidimensional scaling (MDS). Ellipses show mean +/- s.d. (10 sessions) after Generalized Procrustes alignment (without scaling) across sessions.
(**f**) Measured RDMs (d) match the able-bodied PC-IP fMRI RDM (b) better than they match the task-optimal, unstructured model (c), as measured by the whitened unbiased cosine similarity (Diedrichsen et al., 2021) (WUC) (Methods). Mean differences were significant (able-bodied vs unstructured, $P = 5.7 \times 10^{-5}$; two-tailed t-test, 1000 bootstrap samples over 10 sessions). Violin plot: solid horizontal lines indicate the median WUC over bootstrap samples, and dotted lines indicate the first and third quartiles. Noise ceiling: gray region estimates the best possible model fit (Methods). For convenience, a similar figure using a correlation-based similarity metric is shown in Supplementary Figure 2.8.

2.3.4 Representational structure did not trend towards task optimum

Next, we investigated whether the BCI finger representational structure matched that of able-bodied individuals consistently or whether the representational structure changed over time to improve BCI performance. The task-optimal structure hypothesis (3) predicted that the BCI RDMs would trend to optimize for the task statistics (unstructured model, Figure 2.2c) as the participant gained experience with the BCI task. However, we did not find conclusive evidence for a trend from the able-bodied model towards the unstructured model (linear-model session × model interaction: $t(6) = 0.50$, one-tailed t-test P = 0.32, Bayes factor (BF) = 0.66) (Figure 2.3a). Indeed, participant NS's finger RDMs were largely consistent across different recording sessions (average pairwise correlation, excluding the diagonal: r = 0.90 +/- s.d. 0.04, min 0.83. max 0.99).

We considered whether learning, across sessions or within sessions, could have caused smaller-scale changes in the representational structure. The observed representational structure, where middle-ring and ring-pinky pairs had relatively small distances, was detrimental to classification performance. The majority (70%) of the online classification errors were middle-ring or ring-pinky confusions (Figure 2.1b). Due to these systematic errors, one might reasonably predict that plasticity mechanisms would improve control by increasing the inter-finger distances between the confused finger pairs. Contrary to this prediction, the middle-ring and ring-pinky distances did not increase over the course of the experiment (across sessions: $t(8) = -4.5$, one-tailed t-test P > 0.99, BF = 0.03; across runs within sessions: $t(82) = -0.45$, one-tailed t-test P = 0.67, BF = 0.12) (Figure 2.3b). When analyzing all finger pairs together, the inter-finger distances also did not increase (across sessions: $t(8) = -4.0$, one-tailed t-test P = 0.98, BF = 0.01; across runs within sessions: $t(74) = -2.4$, one-tailed t-test P = 0.99, BF = 0.02), as visualized by the similarity between the average early-half RDM and the average late-half RDM (Figure 2.3c). These analyses demonstrate that the representational structure did not trend towards the task optimum (Figure 2.2c) with experience, ruling out the task-statistics hypothesis (3).

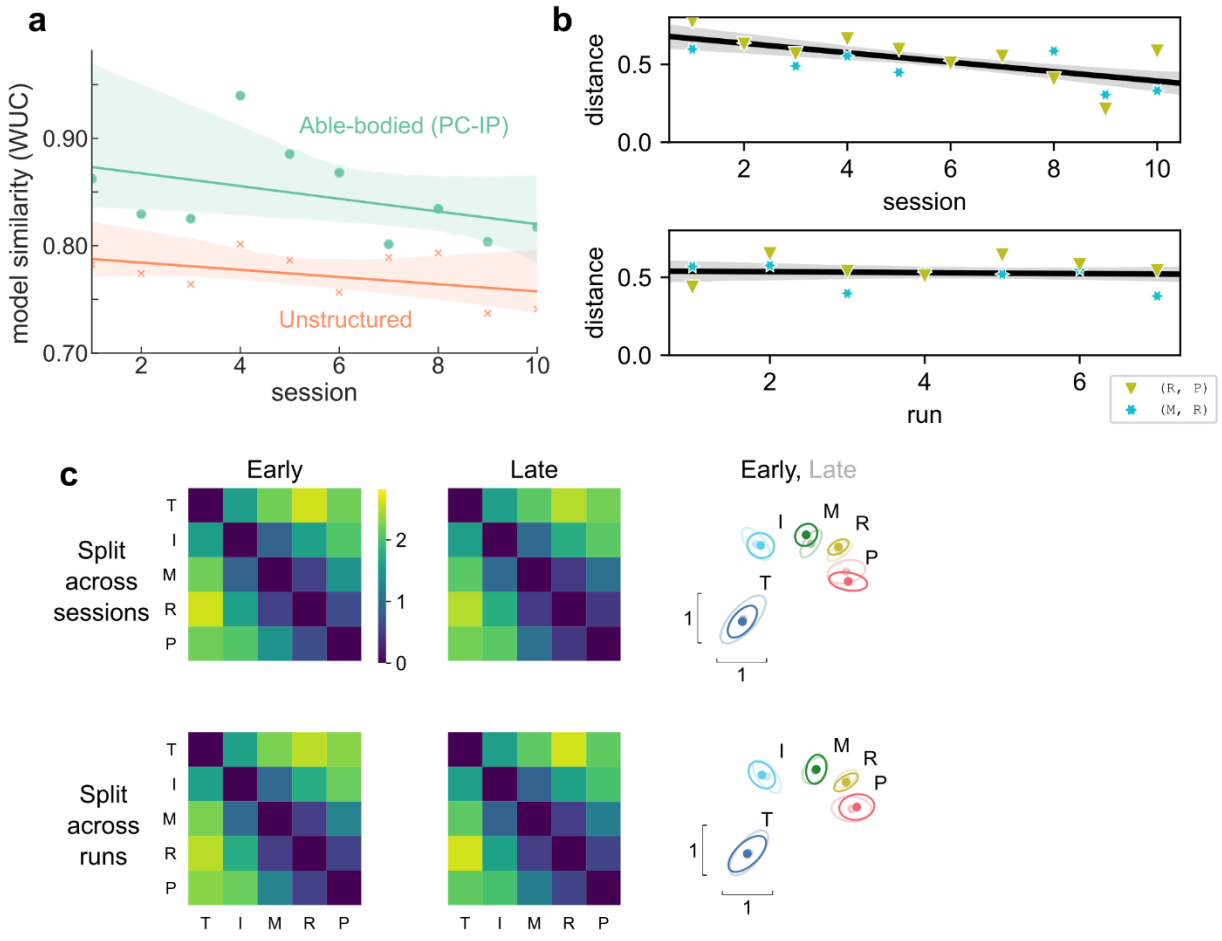

Figure 2.3. Hand representation changed minimally after weeks of BCI control
(**a**) Slope comparison shows that the model fit did not trend towards the unstructured model over sessions (P = 0.32). (**b**) The distance between high-error finger pairs (middle-ring and ring-pinky) did not increase across sessions or runs (within sessions), as shown by partial regression plots. Distance metric: cross-validated Mahalanobis, averaged across runs (for the session plot) or averaged across sessions (for the run plot). The black line indicates linear regression. The gray shaded region indicates a 95% confidence interval. Each run consisted of 8 presses per finger.
(**c**) Minimal change in representational structure between early and late sessions or between early and late runs. Mean RDM, when grouped by sessions (top row) or individual runs (bottom row). Grouped into early half (left column) or late half (center column). MDS visualization (right column) of early (opaque) and late (translucent) representational structures after Generalized Procrustes alignment (without scaling, to allow distance comparisons).

2.3.5 Finger representational structure is motor-like and then somatotopic

PPC is hypothesized to overcome inherent sensory delays by computing an internal forward model for rapid sensorimotor control (Wolpert et al., 1998; Desmurget and Grafton, 2000; Mulliken et al., 2008a). The forward model integrates an efference copy of motor signals and delayed sensory feedback to dynamically predict the state of the body. The hypothesized forward-model role would predict that the representational structure changes over the time course of each movement, with an

early motor-command-like component during movement initiation. To investigate this temporal evolution, we modeled the representational structure of digit movements at each time point as a non-negative linear combination (Kietzmann et al., 2019) of potentially predictive models (Figure 2.4a).

We considered three models (Ejaz et al., 2015) that could account for representational structure: hand usage, muscle activation, and somatotopic. The hand-usage model (Figure 2.4b) predicts that the neural representational structure should follow the correlation pattern of finger kinematics during natural hand use. The muscle activation model (Figure 2.4c) predicts that the representational structure should follow the coactivation patterns of muscle activity during individual finger movements. The somatotopic model (Figure 2.4d) predicts that the representational structure should maintain the spatial relationship between fingers, with neighboring fingers represented similarly to each other (Ejaz et al., 2015; Schellekens et al., 2018). At the neural population level, the somatotopic model is analogous to Gaussian receptive fields (Schellekens et al., 2018).

Because the hand usage model is nearly multicollinear with the muscle and somatotopic models (variance inflation factor: $VIF_{usage,OLS} = VIF_{usage,NNLS} = 20.9$, Methods), we first reduced the number of component models. Through a model selection procedure (Methods), we found that the hand-usage+somatotopy and muscle+somatotopy model combinations matched the data best (Supplementary Figure 2.12), with the muscle+somatotopy model matching the data marginally better. Thus, in the main text, we present our temporal analysis using the muscle and somatotopy component models.

Figure 2.4e shows the decomposition of the representational structure into the muscle and somatotopic component models. The results show a dynamic structure, with the muscle model emerging 170ms earlier than the somatotopic model ($P = 0.002$, two-sided Wilcoxon signed-rank test). This timing difference was consistent across individual sessions (Supplementary Figure 2.13) and task contexts, such as the calibration task (Supplementary Figure 2.14). Indeed, the transition from the muscle model (Figure 2.4c) to the somatotopic model (Figure 2.4d) is visually apparent when comparing the average RDMs at 600ms (muscle-model-like) and 1200ms (somatotopic) (Figure 2.4e).

These temporal dynamics were robust to our feature selection procedure, demonstrating a similar timing difference for the hand-usage+somatotopy model combination (Supplementary Figure 2.14).

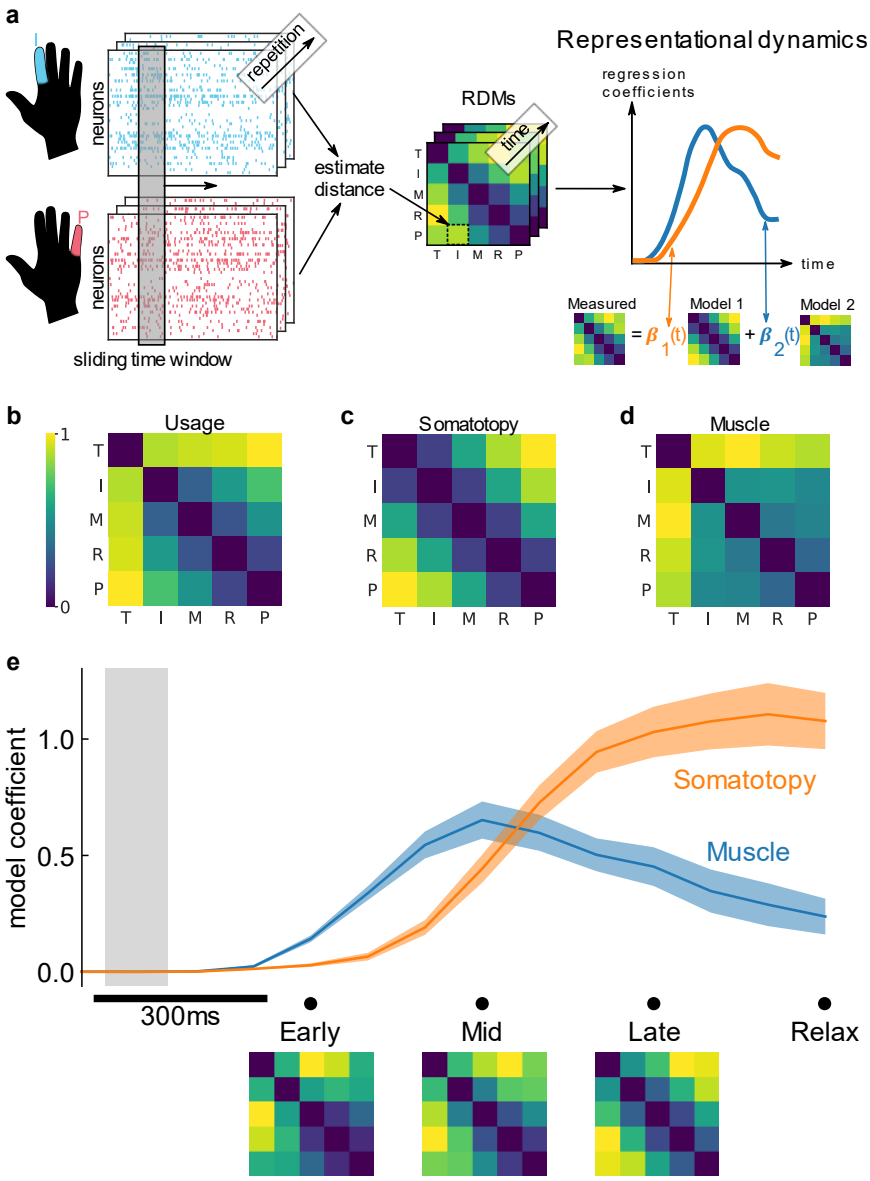

Figure 2.4. Representational dynamics analysis (RDA) dissociates neural processes over time.

(**a**) RDA performs representational similarity analysis (RSA) in a sliding window across time. Here, we model the measured representational structure as a nonnegative linear combination of component model RDMs.

(**b-d**) Hypothesized explanatory component RDMs: usage, muscle, and somatotopic (Ejaz et al., 2015). Max-scaled to [0, 1].

(**e**) RDA of the measured RDM over time shows an early fit to the muscle model and a late fit to the somatotopic model. Confidence intervals indicate +/- s.e.m. bootstrapped across 10 sessions. Gray shaded region indicates the approximate onset time of the saccade to cue (interquartile range across trials). Difference in model start-time (170ms, Methods) was significant ($P = 0.002$, two-sided Wilcoxon signed-rank test). RDM snapshots (bottom, each max-scaled to [0, 1]) intuitively visualize the change in representational structure over time from muscle-like to somatotopic.

2.4 Discussion

2.4.1 Neural prosthetic control of individual fingers using recordings from PC-IP

We found that participant NS could robustly control the movement of individual fingers using a neural prosthetic in a variety of contexts (Figure 2.1 and Supplementary Figure 2.3), even after years of paralysis. Her brain-computer interface (BCI) control accuracy exceeded the previous best of other five-finger, online BCI control studies (Hotson et al., 2016; Jorge et al., 2020). These results establish PC-IP as a candidate implant region for dexterous neural prostheses.

2.4.2 Connecting brain-computer interface studies to basic neuroscience

Although previous studies have shown that the anterior intraparietal area (AIP) of PPC is involved in whole-hand grasping (Murata et al., 2000; Klaes et al., 2015; Schaffelhofer and Scherberger, 2016), our work is the first to show individual finger representations in PPC (Supplementary Figure 2.4). Likewise, many other BCI studies with tetraplegic participants have contributed novel discoveries to basic neuroscience, deepening our understanding of the human cortex (Zhang et al., 2017; Rutishauser et al., 2018; Stavisky et al., 2019; Aflalo et al., 2020; Willett et al., 2020; Chivukula et al., 2021). A frequent (Flesher et al., 2016; Armenta Salas et al., 2018; Stavisky et al., 2019; Willett et al., 2020; Chivukula et al., 2021; Fifer et al., 2021; Andersen and Aflalo, 2022) discussion question is: how well do these findings generalize to the brains of able-bodied individuals? Specifically, do the observed phenomena result from partial reorganization (Nardone et al., 2013; Kambi et al., 2014) after spinal cord injury, or do they reflect intact motor circuits, preserved from before injury (Makin and Bensmaia, 2017)?

Early human BCI studies (Hochberg et al., 2006; Collinger et al., 2013c) recorded from the motor cortex and found that single-neuron directional tuning is qualitatively similar to that of able-bodied non-human primates (NHPs) (Georgopoulos et al., 1982; Hochberg et al., 2006). Many subsequent human BCI studies have also successfully replicated results from other classical NHP neurophysiology studies (Hochberg et al., 2012; Collinger et al., 2013c; Aflalo et al., 2015; Gilja et al., 2015; Bouton et al., 2016; Ajiboye et al., 2017; Brandman et al., 2018), leading to the general heuristic that the sensorimotor cortex retains its major properties after spinal cord injury (Andersen and Aflalo, 2022). This heuristic further suggests that BCI studies of tetraplegic individuals should generalize to able-bodied individuals. However, this generalization hypothesis has so far lacked direct, quantitative comparisons between tetraplegic and able-bodied individuals. Thus, as human BCI studies expand beyond replicating results and begin to challenge conventional wisdom, neuroscientists have questioned whether cortical reorganization could influence these novel phenomena (see Discussions of (Flesher et al., 2016; Armenta Salas et al., 2018; Stavisky et al., 2019; Willett et al., 2020; Chivukula et al., 2021; Fifer et al., 2021; Andersen and Aflalo, 2022)). As an example of a novel discovery, a recent BCI study found that the hand knob of tetraplegic individuals is directionally tuned to movements of the entire body (Willett et al., 2020), challenging the traditional notion that primary somatosensory and motor subregions respond selectively to individual body parts (Penfield and Boldrey, 1937). Given the brain's capacity for reorganization (Jain et al., 2008; Kambi et al., 2014), could these BCI results be specific to cortical remapping? Detailed comparisons with able-bodied individuals, as shown here, may help shed light on this question.

2.4.3 Matching finger organization between tetraplegic and able-bodied participants

We asked whether participant NS's BCI finger representations resembled that of able-bodied individuals or whether her finger representations had reorganized after paralysis. Single-neuron recordings of PC-IP during individuated finger movements are not available in either able-bodied human participants or non-human primates. However, many fMRI studies have characterized finger representations (Yousry et al., 1997; Ejaz et al., 2015; Kikkert et al., 2016, 2021), and representational similarity analysis (RSA) has previously shown RDM correspondence between fMRI and single-neuron recordings of another cortical region (inferior temporal cortex) (Kriegeskorte et al., 2008b). This match was surprising because single-neuron and fMRI recordings differ fundamentally; single-neuron recordings sparsely sample 10^2 neurons in a small region, while fMRI samples $10^4 – 10^6$ neurons/voxel (Kriegeskorte and Diedrichsen, 2016; Guest and Love, 2017). The correspondence suggested that RSA might identify modality-invariant neural organizations (Kriegeskorte et al., 2008b), so here we used fMRI recordings of human PC-IP as an able-bodied model.

We found that participant NS exhibited a consistent finger representational structure across sessions, and this representational structure matched the able-bodied fMRI model better than the task-optimal, unstructured model. When compared with individual able-bodied participants, participant NS's finger organization was also quite typical, in part due to the relative variability in PC-IP fMRI representational structure across able-bodied participants.

The motor cortex (MC) fMRI finger representation is well-studied and has been shown to reflect the patterns of natural hand use (Ejaz et al., 2015; Kikkert et al., 2016; Wesselink et al., 2019), so we also considered a model constructed from MC fMRI recordings. Compared to the PC-IP fMRI finger representation, MC represents the non-thumb fingers more distinctly from each other (Supplementary Figure 2.6). Interestingly, participant NS's finger RDMs more strongly matched the able-bodied MC fMRI model, reaching similarities close to the theoretical maximum (Supplementary Figure 2.8 and Supplementary Figure 2.10). This result does obscure a straightforward interpretation of the RSA results—why does our recording area match MC better than the corresponding implant location? Several factors might contribute, including differing neurovascular sensitivity to the early and late phases of the neural response (Figure 2.4e), heterogeneous neural organizations across the single-neuron and voxel spatial scales (Kriegeskorte and Diedrichsen, 2016; Guest and Love, 2017; Arbuckle et al., 2020), or mismatches in functional anatomy between participant NS and standard atlases (Eickhoff et al., 2018). Furthermore, fMRI BOLD contrast is thought to reflect cortical inputs and intracortical processing (Logothetis et al., 2001). Thus, the match between PC-IP spiking output and MC fMRI signals could also suggest that PC-IP sends signals to MC, thereby driving the observed MC fMRI structure.

Even so, it is striking that participant NS's finger representation matches the neural and hand use patterns (Figure 2.4b and Supplementary Figure 2.12) of able-bodied individuals. Despite the lack of overt movement or biomechanical constraints (Lang and Schieber, 2004a), the measured finger representation still reflected these usage-related patterns. This result matches recent sensorimotor cortex studies of tetraplegic individuals, where MC decoding errors (Jorge et al., 2020) and S1 finger somatotopy (Kikkert et al., 2021) appeared to reflect able-bodied usage patterns. Taken together with our dynamics analyses (see below Discussion), the evidence supports the interpretation

that motor representations are preserved after paralysis. Comparisons with single-neuron recordings from able-bodied participants would validate this interpretation but may be difficult to acquire.

2.4.4 Able-bodied-like finger representation is not explained by learning

Hand use patterns shape neural finger organization (Ejaz et al., 2015; Kikkert et al., 2016; Wesselink et al., 2019), so we considered the possibility that participant NS's able-bodied-like representational structure also emerged from BCI usage patterns after paralysis. Contrary to this hypothesis, her BCI finger representational structure changed minimally over weeks (Figure 2.3). Furthermore, even though participant NS's representational structure contributed to BCI errors (Figure 2.1b) and she was anecdotally cognizant of which fingers would get confused, she did not increase the neural distance between fingers with experience. This relative stability suggests that the measured representational structure has been stable after paralysis, rather than emergent from BCI learning.

The stability of finger representations here suggests that BCIs can benefit from the pre-existing, natural repertoire (Hwang et al., 2013), although learning can play an important role under different experimental constraints. In our study, the participant received only a delayed, discrete feedback signal after classification (Figure 2.1a). Because we were interested in understanding participant NS's natural finger representation, we did not artificially perturb the BCI mapping. When given continuous feedback, however, participants in previous BCI studies could learn to adapt to within-manifold perturbations to the BCI mapping (Ganguly and Carmena, 2009; Sadtler et al., 2014; Vyas et al., 2018; Sakellaridi et al., 2019). BCI users can even slowly learn to generate off-manifold neural activity patterns when the BCI decoder perturbations were incremental (Oby et al., 2019). Notably, learning was inconsistent when perturbations were sudden, indicating that learning is sensitive to specific training procedures.

So far, most BCI learning studies have focused on two-dimensional cursor control. To further understand how much finger representations can be actively modified, future studies could benefit from perturbations (Oby et al., 2019; Kieliba et al., 2021), continuous low-latency neurofeedback (Ganguly and Carmena, 2009; Vyas et al., 2018; Oby et al., 2019), and additional participants. Time-variant BCI decoding algorithms, such as recurrent neural networks (Sussillo et al., 2012; Willett et al., 2021), could also help facilitate learning specific to different time windows of finger movement.

2.4.5 Representational dynamics are consistent with PPC as a forward model

In able-bodied individuals, PPC is thought to maintain a forward estimate of movement state (Wolpert et al., 1998; Desmurget and Grafton, 2000; Mulliken et al., 2008a; Aflalo et al., 2015; McNamee and Wolpert, 2019). As such, PPC receives delayed multimodal sensory feedback and is hypothesized to receive efference copies of motor command signals (Andersen et al., 1997; Mulliken et al., 2008a). This hypothesized role predicts that PPC houses multiple functional representations, each engaged at different time points of motor production.

To dissociate these neural processes, we performed a time-resolved version of representational similarity analysis (Figure 2.4). We considered three component models: muscle, usage, and somatotopic (Ejaz et al., 2015). Our temporal analysis showed a consistent ordering: early emergence of the muscle model followed by the somatotopic model.

This ordering was consistent when exchanging the muscle and hand-usage component models (Figure 2.4 and Supplementary Figure 2.14), as hand-usage and muscle activation patterns

are strongly correlated for individual finger movements (Overduin et al., 2012). Therefore, we group these two models under the single concept of motor production. In the future, more complex multi-finger movements (Ejaz et al., 2015) would help distinguish between muscle and hand-usage models.

The somatotopic model predicts that neighboring fingers will have similar cortical activity patterns (Ejaz et al., 2015). We note that prior fMRI studies described this representational structure as "somatotopic" and captured the spatial relationship between fingers using equidistant Gaussian receptive fields (Ejaz et al., 2015; Schellekens et al., 2018). Gaussian receptive fields have been useful tools for understanding digit topographies within the sensorimotor cortex (Schellekens et al., 2018, 2021). In another study with participant NS, we found that the same PC-IP population encodes actual touch (Chivukula et al., 2021) with Gaussian-like receptive fields. Based on these results, the somatotopic model can be thought of as a sensory-consequence model. However, because participant NS has no sensation below her shoulders, we interpret the somatotopic model as the preserved prediction of the sensory consequences of a finger movement. These sensory outcome signals could be the consequence of internal computations within the PPC or could come from other structures important for body-state estimation, such as the cerebellum (McNamee and Wolpert, 2019).

The 170ms timing difference we found roughly matches the 60ms + 60ms delay between feedforward muscle activation and somatosensory afferents (Scott, 2016; Sollmann et al., 2017) in able-bodied individuals. Given PPC's hypothesized role as a forward model, PPC likely integrates motor planning and production signals to predict sensory outcomes at such a timing (Wolpert et al., 1998; Desmurget and Grafton, 2000; Mulliken et al., 2008a; McNamee and Wolpert, 2019). Alternatively, because participant NS cannot move overtly, the sensory-consequences model could instead reflect the error between the internal model's expected sensory outcomes and the actual (lack of) sensory feedback (Adams et al., 2013). In either scenario, the match in timing between BCI control and able-bodied individuals provides further evidence that the recorded motor circuits have preserved their functional role.

2.4.6 Preserved motor representations in PC-IP after paralysis

A persistent question in neuroscience has been how experience shapes the brain, and to what extent existing neural circuits can be modified. Early studies by Merzenich, Kaas, and colleagues showed that the primary somatosensory cortex reorganized after amputation, with intact body parts invading the deprived cortex (Merzenich et al., 1984; Pons et al., 1991; Qi et al., 2000). However, the authors also recognized that the amputated body part might persist in latent somatosensory maps. Since then, preserved, latent somatosensory representations have been demonstrated in studies of amputation (Kikkert et al., 2016; Bruurmijn et al., 2017; Makin and Bensmaia, 2017; Wesselink et al., 2019) and even paralysis (Flesher et al., 2016; Armenta Salas et al., 2018; Fifer et al., 2021; Kikkert et al., 2021). Overall, deafferentation appears to expand the remaining regions slightly, even while the pre-injury structure persists in the deafferented cortex (Makin and Bensmaia, 2017). Fewer studies have investigated sensorimotor plasticity beyond the primary somatosensory and motor cortex, but our results in PC-IP indicate that association areas can also remain stable after paralysis.

The topic of cortical reorganization has long been significant to the development of BCIs, particularly when deciding where to implant recording electrodes. If, as previously thought, sensory deprivation drives cortical reorganization and any group of neurons can learn to control a prosthetic (Fetz, 1969; Moritz and Fetz, 2011), the specific implant location would not affect BCI performance.

However, our results and others (Smirnakis et al., 2005; Hwang et al., 2013; Kikkert et al., 2016, 2021; Bruurmijn et al., 2017; Makin and Bensmaia, 2017; Wesselink et al., 2019) suggest that the pre-injury properties of brain regions do affect BCI performance. Even though experience shapes neural organization (Merzenich et al., 1984; Ejaz et al., 2015; Wesselink et al., 2019), representations may be remarkably persistent once formed (Wesselink et al., 2019; Kikkert et al., 2021). Thus, even though BCIs bypass limbs and their biomechanical constraints (Lang and Schieber, 2004a), BCIs may still benefit from tapping into the preserved, natural (Hwang et al., 2013) movement repertoire of motor areas.

As BCIs enable more complex motor skills, such as handwriting (Willett et al., 2021), future studies could investigate whether these complex skills also retain their pre-injury representational structure. For example, does a tetraplegic participant's BCI handwriting look like their physical, pre-injury handwriting? These results will have important implications for the design of future neural prosthetics.

2.5 Methods

2.5.1 Data collection

2.5.1.1 Study participant

The study participant NS has an AIS-A spinal cord injury at cervical level C3-C4 that she sustained approximately ten years before this study. Participant NS cannot move or feel her hands. As part of a BCI clinical study (ClinicalTrials.gov identifier: NCT01958086), participant NS was implanted with two 96-channel Neuroport Utah electrode arrays (Blackrock Microsystems model numbers 4382 and 4383). She consented to the surgical procedure as well as to the subsequent clinical studies after understanding their nature, objectives, and potential risks. All procedures were approved by the California Institute of Technology, Casa Colina Hospital and Centers for Healthcare, and the University of California, Los Angeles Institutional Review Boards.

2.5.1.2 Multielectrode array implant location

The recording array was implanted over the hand/limb region of the left PPC at the junction of the intraparietal sulcus (IPS) with the postcentral sulcus (PCS) (Supplementary Figure 2.1; Talairach coordinates [−36 lateral, 48 posterior, 53 superior]). We previously (Aflalo et al., 2015; Klaes et al., 2015; Zhang et al., 2017) referred to this brain area as the anterior intraparietal area (AIP), a region functionally defined in non-human primates (NHPs). Here we describe the implanted area anatomically, denoting it the postcentral-intraparietal area (PC-IP). More details regarding the methodology for functional localization and implantation can be found in (Aflalo et al., 2015).

2.5.1.3 Neural data preprocessing

Using the NeuroPort system (Blackrock Microsystems), neural signals were recorded from the electrode array, amplified, analog bandpass-filtered (0.3 Hz to 7.5 kHz), and digitized (30 kHz, 250 nV resolution). A digital high-pass filter (250 Hz) was then applied to each electrode.

Threshold crossings were detected at a threshold of –3.5 x RMS (root-mean-square of an electrode's voltage time-series). Threshold crossings were used as features for in-session BCI

control. For all other analyses, we used k-medoids clustering on each electrode to spike-sort the threshold crossing waveforms. The first $n \in \{2, 3, 4\}$ principal components were used as input features to k-medoids, where n was selected for each electrode to account for 95% of waveform variance. The gap criteria (Tibshirani et al., 2001) was used to determine the number of waveform clusters for each electrode.

2.5.2 Experimental setup

2.5.2.1 Recording sessions

Experiments were conducted in 2–3-hour recording sessions at Casa Colina Hospital and Centers for Healthcare. All tasks were performed with participant NS seated in her motorized wheelchair with her hands resting prone on the armrests. Participant NS viewed text cues on a 27-inch LCD monitor that occupied approximately 40 degrees of visual angle. Cues were presented using the psychophysics toolbox (Brainard, 1997) for MATLAB (Mathworks).

The data were collected on 9 days over 6 weeks. Almost all experiment days were treated as individual sessions (i.e., the day's recordings were spike-sorted together). The second experiment day (2018-09-17) was an exception, with data being recorded in a morning period and an afternoon period with a sizable rest in between. To reduce the effects of recording drift, we treated the two periods as separate sessions (i.e., spike-sorted each separately) for a total of 10 sessions. Each session can thus be considered a different resampling of a larger underlying neural population, with both unique and shared neurons each session. We did not re-run the calibration task for the afternoon session, resulting in 9 sessions of the calibration task for Supplementary Figure 2.3b.

Each session consisted of a series of 2–3 minute, uninterrupted "runs" of the task. The participant rested for a few minutes between runs as needed.

2.5.2.2 Calibration task

At the beginning of each recording session, the participant performed a reaction-time finger flexion task (Supplementary Figure 2.2; denoted "calibration task" in the Results) to train a finger classifier for subsequent runs of the primary task. On each trial, a letter appeared on the screen (e.g., "T" for thumb). The participant was instructed to immediately flex the corresponding finger on the right hand (contralateral to the implant), as though pressing a key on a keyboard. The condition order was block-randomized, such that each condition appeared once before repetition. The classifier was then calibrated according to the Finger Classification section.

2.5.2.3 Finger flexion grid task

In the primary task, movement cues were arranged in a 3 x 4 grid of letters on the screen (Figure 2.1a). Each screen consisted of two repetitions each of T (thumb), I (index), M (middle), R (ring), P (pinky/little), and X (No-Go) arranged randomly on the grid. Each trial lasted three seconds. At the beginning of each trial, a new cue was randomly selected with a crosshairs indicator, which jittered randomly to prevent letter occlusion. Each cue was selected once (for a total of 12 trials) before the screen was updated to a new arrangement. Each run consisted of 3–4 screens.

On each trial, the participant was instructed to immediately 1) saccade to the cued target, 2) fixate, and 3) attempt to press the corresponding finger. During both movement and No-Go trials,

the participant was instructed to fixate on the target at least until the visual classification feedback was shown. The cue location randomization was used to investigate whether cue location would affect movement representations.

On each trial, 1.5 seconds after cue presentation, the classifier decoded the finger movement and presented its prediction via text feedback overlaid on the cue.

2.5.2.4 No-movement control task

The control task was like the primary task, except that the subject was instructed to saccade to each cued letter and fixate without attempting any finger movements. No classification feedback was shown.

2.5.3 Statistical analysis

2.5.3.1 Unit selection

Single-unit neurons were identified using the k-medoids clustering method, as described in the Neural Data Preprocessing section. Analyses in the main text used all identified units, regardless of sort quality. With spike-sorting, there is always the possibility that a single waveform cluster corresponds to activity from multiple neurons. To confirm that potential multi-unit clustering did not bias our results, we repeated our analyses using only well-isolated units (Supplementary Figure 2.15).

Well-isolated single units were identified using the L-ratio metric (Schmitzer-Torbert et al., 2005). The neurons corresponding to the lowest third of L-ratio values (across all sessions) were selected as "well-isolated." This corresponded to a threshold of $L_{ratio} = 10^{-1.1}$ dividing well-isolated single units and potential multi-units (Supplementary Figure 2.15).

2.5.3.2 Single-unit tuning to finger flexion

We calculated the firing rate for each neuron in the window [0.5, 1.5] seconds after cue presentation. To calculate significance for each neuron (Supplementary Figure 2.4), we used a two-tailed t-test comparing each movement's firing rate to the No-Go firing rate. A neuron was considered significantly tuned to a movement if $P < 0.05$ (after FDR correction). We also computed the mean firing rate change between each movement and the No-Go condition. If a neuron was significantly tuned to at least one finger, we denoted the neuron's "best finger" as the significant finger with the largest effect size (mean firing rate change). For each neuron and finger, we also calculated the discriminability index (d', RMS standard deviation) between the baseline (No-Go) firing rate and the firing rate during finger movement.

In Supplementary Figure 2.4, neurons were pooled across all 10 sessions. Neurons with mean firing rates less than 0.1 Hz were excluded to minimize sensitivity to discrete spike-counting.

2.5.3.3 Finger classification

To classify finger movements from firing rate vectors, we used linear discriminant analysis (LDA) with diagonal covariance matrices (Dudoit et al., 2002) (a form of regularization); diagonal LDA is also equivalent to Gaussian Naive Bayes (GNB) when GNB assumes that all classes share a covariance matrix.

We used data from the calibration task to fit the BCI classifier. Input features (firing rate vectors) were calculated by counting the number of threshold crossings on each electrode during a 1-second time window within each trial's movement execution phase. The exact time-window was a hyperparameter for each session and was chosen to maximize the cross-validated accuracy on the calibration dataset. Electrodes with mean firing rates less than 1 Hz were excluded to prevent low-firing rate discretization effects. This classifier was then used in subsequent online BCI control for the main task (finger flexion grid).

During online control of the finger flexion grid task, input features were similarly constructed by counting the threshold crossings from each electrode in a 1-second time window. This time window was fixed to [0.5, 1.5] seconds after cue presentation. The window start-time was chosen based on the estimated saccade latency in the first experimental session. The saccade latency was estimated by taking the median latency for the subject to look > 80% of the distance between targets. The analysis window was a priori determined to be 1 second; this choice was supported post-hoc by a sliding window analysis (not shown), which confirmed that finger movements could be accurately classified up to 1.6 seconds after cue. The online classifier was occasionally retrained using data from this main task, usually every 4 run-blocks.

Offline classification accuracy (Supplementary Figure 2.3) was computed using leave-one-out cross-validation (within each session). We used features from the same time window as the online control task. However, offline analyses used firing rates after spike-sorting, instead of raw threshold crossings.

In the Results section, reported classification accuracies aggregate trials over all sessions (as opposed to averaging the accuracies across sessions with different numbers of trials). Reported standard deviations indicate variability across sessions, weighted by the number of trials in each session. To visualize confusion matrices, trials were pooled across sessions. Confusion matrix counts were normalized by row sum (true label) to display confusion percentages.

In the first session (2018-09-10), the No-Go condition (X) was not cued in the calibration task, so the classifier did not output No-Go predictions during that session. However, No-Go conditions were cued in the main task; these 84 No-Go trials were thus excluded from the online control accuracy metrics (Figure 2.1b), but they were included in the offline cross-validated confusion matrix (Supplementary Figure 2.3).

2.5.3.4 Cross-validated neural distance

We quantified the dissimilarity between the neural activity patterns of each finger pair (j, k), using the cross-validated (squared) Mahalanobis distance (Nili et al., 2014; Schütt et al., 2019):

$$d_{jk}^2 = \left(b_j - b_k\right)_A \left(\frac{\Sigma_A + \Sigma_B}{2}\right)^{-1} \left(b_j - b_k\right)_B^T / N$$

Equation 2.1

where A and B denote independent partitions of the trials, Σ are the partition-specific noise covariance matrices, (b_j, b_k) are the trial measurements of firing rate vectors for conditions (j, k), and N normalizes for the number of neurons. The units of d_{jk}^2 are $\text{unitless}^2/\text{neuron}$.

The cross-validated Mahalanobis distance, also referred to as the "crossnobis" distance (Schütt et al., 2019), measures the separability of multivariate patterns, analogous to LDA classification accuracy (Nili et al., 2014). To generate independent partitions A and B for each session, we stratified-split the trials into 5 non-overlapping subsets. We then calculated the crossnobis distance for all combinations of subsets (A, B) and averaged the results. Cross-validation ensures that the (squared) distance estimate is unbiased; $E[d_{jk}^2] = 0$ when the underlying distributions are identical (Walther et al., 2016). The noise covariance Σ was regularized (Ledoit and Wolf, 2003) to guarantee invertibility.

Similar results were also obtained when estimating neural distances with the cross-validated Poisson symmetrized KL-divergence (Schütt et al., 2019) (Supplementary Figure 2.8).

2.5.3.5 Representational models

We used representational dissimilarity matrices (RDMs) to describe both the type and format of information encoded in a recorded population. To make these RDMs, we calculated the distances between each pair of finger movements and organized the 10 unique inter-finger distances into a $[n_{fingers}, n_{fingers}]$-sized representational dissimilarity matrix (RDM) (Figure 2.2d). Conveniently, the RDM abstracts away the underlying feature types, enabling direct comparison with RDMs across brain regions (Kietzmann et al., 2019), subjects, or recording modalities (Kriegeskorte et al., 2008b).

We also used RDMs to quantify hypotheses about how the brain might represent different actions. In Figure 2.2b, we generated an able-bodied model RDM using fMRI data from two independent studies: (Kieliba et al., 2021) (N = 29, pre-intervention, right hand, 3T scans) and (Ejaz et al., 2015) (N = 7, no intervention, right hand, 7T scans). The fMRI ROI was selected to match participant NS's anatomical implant location (PC-IP). Specifically, a 4mm geodesic distance around vertex 7123 was initially drawn in fs_LR_32k space, then resampled onto fsaverage. The RDM for each subject was then calculated using the cross-validated (squared) Mahalanobis distance between fMRI activity patterns. Based on a permutation shuffle test, RDMs were similar between the studies' groups of participants, so we aggregated the RDMs into a single dataset here. The MC RDMs (Supplementary Figure 2.6) used data from the same scans (Ejaz et al., 2015; Kieliba et al., 2021), with ROIs covering Brodmann area 4 near the hand knob of the precentral gyrus.

In Figure 2.4 and its supplemental figures, we decomposed the data RDMs into model RDMs borrowed from (Ejaz et al., 2015). The hand usage model was constructed using the velocity time series of each finger's MCP joint during everyday tasks (Ingram et al., 2008). The muscle activity model was constructed using EMG activity during single- and multi-finger tasks. The somatotopic model is based on a cortical sheet analogy and assumes that finger activation patterns are linearly spaced Gaussian kernels across the cortical sheet. The somatotopic model is based on a cortical sheet analogy and assumes that finger activation patterns are linearly spaced Gaussian kernels across the cortical sheet. Further modeling details are available in the methods section of (Ejaz et al., 2015).

2.5.3.6 Comparing representational structures

We used the *rsatoolbox* Python library (Schütt et al., 2019) to calculate data RDMs and compare them with model RDMs (representational similarity analysis (Kriegeskorte et al., 2008a), RSA).

To quantify model fit, we used the whitened unbiased RDM cosine similarity (WUC) metric (Diedrichsen et al., 2021), which (Diedrichsen et al., 2021) recommend for models that predict continuous real values. We used WUC instead of Pearson correlation for two reasons (Diedrichsen et al., 2021). First, cosine similarity metrics like WUC properly exploit the informative zero point; we used an unbiased distance estimate, so $d_{jk}^2 = 0$ indicates that the distributions (j, k) are identical. Second, Pearson correlation assumes that observations are independent, but the elements of each RDM covary (Diedrichsen et al., 2021) because the underlying dataset is shared. For example, the (thumb, middle)-pairwise dissimilarity uses the same thumb data as the (thumb, ring)-pairwise dissimilarity.

Like correlation similarities, a larger WUC indicates a better match, and the maximum WUC value is 1. However, cosine similarities like WUC are often larger than the corresponding correlation values or are even close to 1 (Diedrichsen et al., 2021). Thus, while correlation values can be compared against a null hypothesis of 0-correlation, WUC values should be interpreted by comparing against a baseline. The baseline is usually (Diedrichsen et al., 2021) chosen to be a null model where all conditions are pairwise-equidistant (and would thus correspond to 0-correlation). In this study, this happens to correspond to the unstructured model. For more details about interpreting the WUC metric, see (Diedrichsen et al., 2021).

To demonstrate that our model comparisons were robust to the specific choice of RDM similarity metric, we also show model fits using whitened Pearson correlation in Supplementary Figure 2.8. Whitened Pearson correlation is a common alternative to WUC (Diedrichsen et al., 2021).

2.5.3.7 Noise ceiling for model fits

Measurement noise and behavioral variability cause data RDMs to vary across repetitions, so even a perfect model RDM would not achieve a WUC similarity of 1. To estimate the noise ceiling (Nili et al., 2014) (the maximum similarity possible given the observed variability between data RDMs), we assume that the unknown, perfect model resembles the average RDM. Specifically, we calculated the average similarity of each individual-session RDM (Supplementary Figure 2.7) with the mean RDM across all other sessions (i.e., excluding that session):

$$\hat{C} = \frac{1}{D}\sum_{d=1}^{D} similarity(r_d, \bar{r}_{j\neq d})$$

$$\bar{r}_{j\neq d} = \frac{1}{D-1}\sum_{j\neq d} r_j$$

Equation 2.2

where similarity is the WUC similarity function, D is the number of RDMs, r_d refers to a single RDM from an individual session, and $\hat{C}$ is the "lower" noise ceiling. This noise ceiling is analogous to leave-one-out-cross-validation. If a model achieves the noise ceiling, the model fits the data well (Nili et al., 2014).

2.5.3.8 *Measuring changes in the representational structure*

To assess the effect of BCI task experience on the inter-finger distances, we performed a linear regression analysis (Figure 2.3b and Supplementary Figure 2.11). We first subdivided each session's dataset into individual runs and calculated separate RDMs for each (session, run) index. We then used linear regression to predict each RDM's (squared) inter-finger distances from the session index, run index, and finger pair:

$$d_{jk}^2 = \beta_{jk} + \beta_{session} s + \beta_{run} r + \beta_0$$

Equation 2.3

where β_0 is the average inter-finger distance, β_{jk} is the coefficient for finger-pair (j, k), s is the session index, and r is the run index. $|\beta_{session}| > 0$ would suggest that RDMs are dependent on experience across sessions. $|\beta_{run}| > 0$ would suggest that RDMs depend on experience across runs within a session. For t-tests, we conservatively estimated the degrees-of-freedom as the number of RDMs, because the individual elements of each RDM covary and thus are not independent (Diedrichsen et al., 2021). The effect sizes for the session-index predictor and the run-index predictor were quantified using Cohen's f^2 (Cohen, 1988), comparing against the finger-pair-only model as a baseline.

For t-tests without significant differences, we also calculated Bayes factors (BF) to determine the likelihood of the null hypothesis, using the common threshold that Bayes factor < 1/3 substantially supports the null hypothesis (Dienes, 2014). Bayes factors were computed using the R package BayesFactor (Morey et al., 2015) with default priors. To calculate Bayes factors for one-sided t-tests (for example, $\beta > 0$), we sampled (N = 10^6) from the posterior of the corresponding two-sided t-test ($|\beta| > 0$), calculated the proportion of samples that satisfied the one-sided inequality, and divided by the prior odds $\frac{P(\beta>0)}{P(|\beta|>0)} = \frac{1}{2}$ (Morey and Wagenmakers, 2014).

2.5.3.9 *Linear combinations of models*

We modeled the finger RDM (in vector form) as a zero-intercept, non-negative linear combination (Jozwik et al., 2016) of potentially predictive model RDMs: usage, muscle, and somatotopic (Figure 2.4).

First, we used the variance inflation factor (VIF) to assess multicollinearity between the hypothesized models. For each model (e.g., usage), we calculated the standard, ordinary least squares (OLS)-based VIF ($\text{VIF}_{\text{usage,OLS}}$), and we also calculated a modified VIF ($\text{VIF}_{\text{usage,NNLS}}$) based on non-negative least squares (NNLS).

$$\text{VIF}_{j,\text{OLS}} = \frac{1}{1 - R^2_{M_j|M_{-j}}}$$

Equation 2.4

where $R^2_{M_j|M_{-j}}$ is the R^2 from an OLS regression predicting RDM M_j from all other RDMs M_{-j}. VIF_{OLS} values above a threshold indicate that multicollinearity is a problem; VIF>5 or VIF>10 are

common thresholds (James et al., 2013). Here, we constrained the linear combination coefficients to be non-negative, which can sometimes mitigate multicollinearity. Thus, we also calculated VIF_{NNLS}, which follows the same equation above, except that we use NNLS to predict M_j from M_{-j}.

Because multicollinearity was a problem here, we next determined the best subset of model RDMs to use. We used NNLS to predict the data RDM from the model RDMs. We estimated the model fits using leave-one-session-out cross-validation. To estimate model-fit uncertainty, we bootstrapped RDMs (sessions) over the cross-validation procedure (Schütt et al., 2019). We then used the "one-standard error" rule (James et al., 2013) to select the best parsimonious model, choosing the simplest model within one standard error of the best model fit.

2.5.3.10 Representational dynamics analysis

To investigate how the finger movement representational structure unfolds over time, we used a time-resolved version of representational similarity analysis (Kietzmann et al., 2019) (Figure 2.4a). At each timepoint within a trial, we computed the instantaneous firing rates by binning the spikes in a 200ms time window centered at that point. These firing rates were used to calculate cross-validated Mahalanobis distances between each pair of fingers and generate an RDM. Snapshots (Figure 2.4e) show single-timepoint RDMs averaged across sessions.

The temporal sequence of RDMs constitutes an RDM movie (size $[n_{fingers}, n_{fingers}, n_{timepoints}]$) that visualizes the representational trajectory across the trial duration. RDM movies were computed separately for each recording session. At each time point, we linearly decomposed the data RDM into the component models using nonnegative least squares. Because the component models were multicollinear, component models were limited to the subsets chosen in the previous model reduction step. Each component RDM was normalized by its vector length (ℓ_2-norm) before decomposition to allow comparison between coefficient magnitudes. We used bootstrapped sampling of RDMs across sessions and decomposed the bootstrap-mean RDM to generate confidence intervals on the coefficients.

We computed the start-time of each model component as the time at which the corresponding mixture coefficient exceeded 0.2 (about 25% of the median peak-coefficient across models and sessions).

2.5.4 Data availability

Data is available on the BRAIN Initiative DANDI Archive at:
https://dandiarchive.org/dandiset/000147

2.5.5 Code availability

Analysis code is available on GitHub at:
https://github.com/AndersenLab-Caltech/fingers_rsa

2.6 Acknowledgments

We thank NS for her dedicated participation in the study. Tyson Aflalo mentored and collaborated with me throughout this project. Tyson Aflalo and Carey Zhang collected the data. Elena Amoruso, Paulina Kieliba, Tamar Makin, Jörn Diedrichsen, and Spencer Arbuckle generously shared their

fMRI data with me. Tamar Makin and Whitney Griggs provided helpful feedback on my initial drafts.

2.7 Supplementary Material

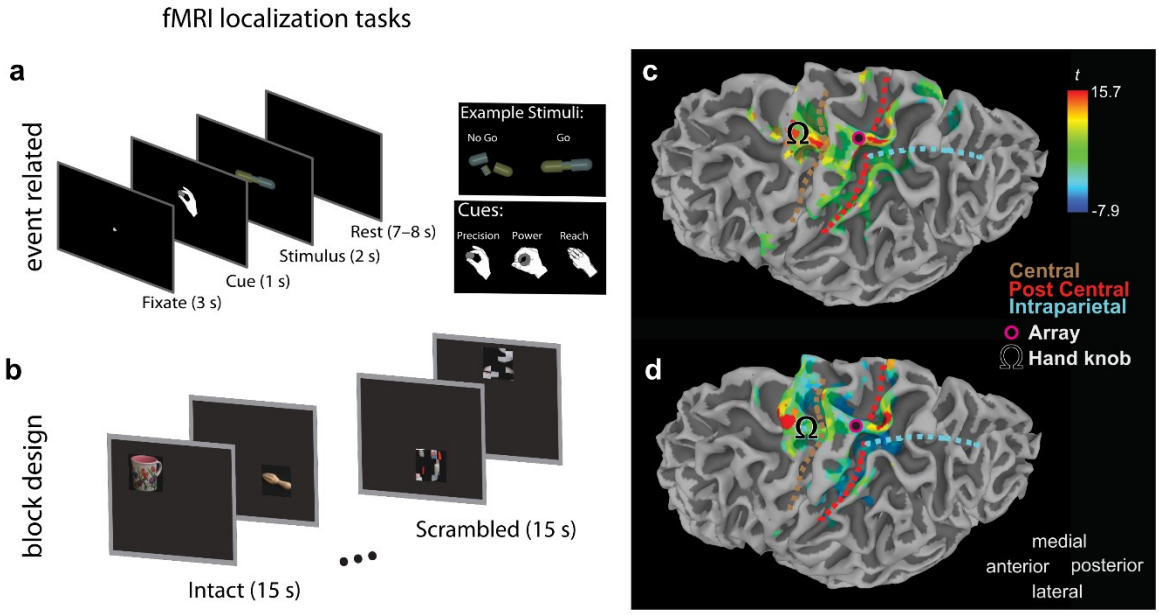

Supplementary Figure 2.1. Multielectrode array implant location. Figure and legend text have been reproduced from Figure S1 of (Aflalo et al., 2020) (CC BY-NC 4.0)

We used fMRI to identify cortical regions involved in imagined reaching and grasping actions. The participant performed two complementary tasks to ensure activation was robust across paradigms.

(**a**) Event-related task design. Following an intertrial interval, the subject was cued to perform a specific imagined movement (precision grasp, power grasp, or reach without hand shaping). Following the cue, a cylindrical object was displayed. If the object was intact, the subject imagined performing the cued movement. If the object was broken, the subject withheld movement.

(**b**) Block task design. Eight blocks were presented for 30 seconds per run. During the first 15 seconds of each block, common objects were presented every three seconds in varying spatial locations. Before each run, the subject was instructed to either imagine pointing at, imagine reaching and grasping, or look naturally at the object. During the last 15 seconds of each block, scrambled images were presented, and the subject was instructed to guess the identity of the object.

(**c**) Statistical parametric map showing voxels with significant activity for grasping ("Go" versus "No-Go") ($p < 0.01$, FDR-corrected), based on task (a). Array location and cortical landmarks are depicted in the legend.

(**d**) Statistical parametric map showing voxels with significant activation ($P < 0.01$, FDR-corrected) for grasping versus looking, based on task (b).

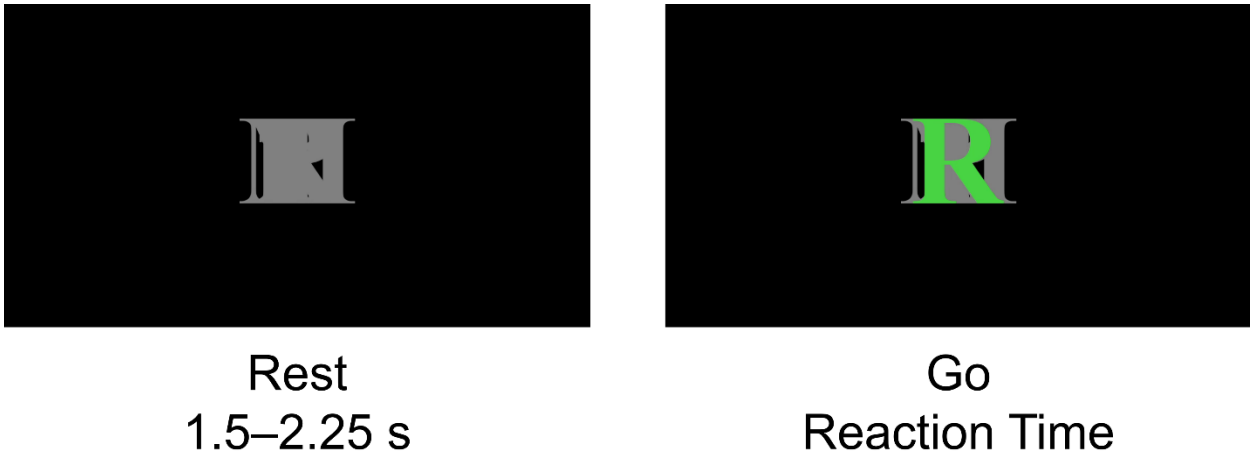

Supplementary Figure 2.2. Calibration task.
Task structure, single trial. Each trial consisted of an intertrial interval (ITI) and a reaction-time Go phase. During the Go phase, green text specified which digit to flex. All letters were overlaid in gray to minimize visual differences between ITI and Go phases.
(Legend) T = thumb, I = index, M = middle, R = ring, P = pinky, X = no movement

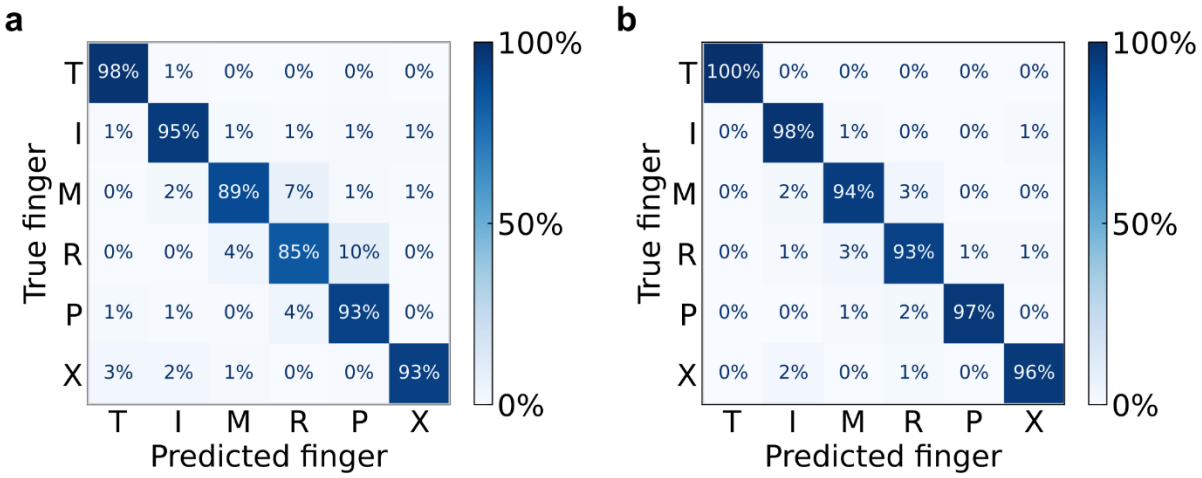

Supplementary Figure 2.3. Robust cross-validated finger classification during main and calibration tasks.

(**a**) Confusion matrix of offline finger classification, cross-validated within single sessions. 4080 trials of the main task aggregated over 10 sessions.

(**b**) Confusion matrix of offline finger classification, cross-validated within single sessions. 530 trials of the calibration task aggregated over 9 sessions.

(Legend) T = thumb, I = index, M = middle, R = ring, P = pinky, X = no movement. Each entry (i, j) in the matrix corresponds to the ratio of movement i trials that were classified as movement j.

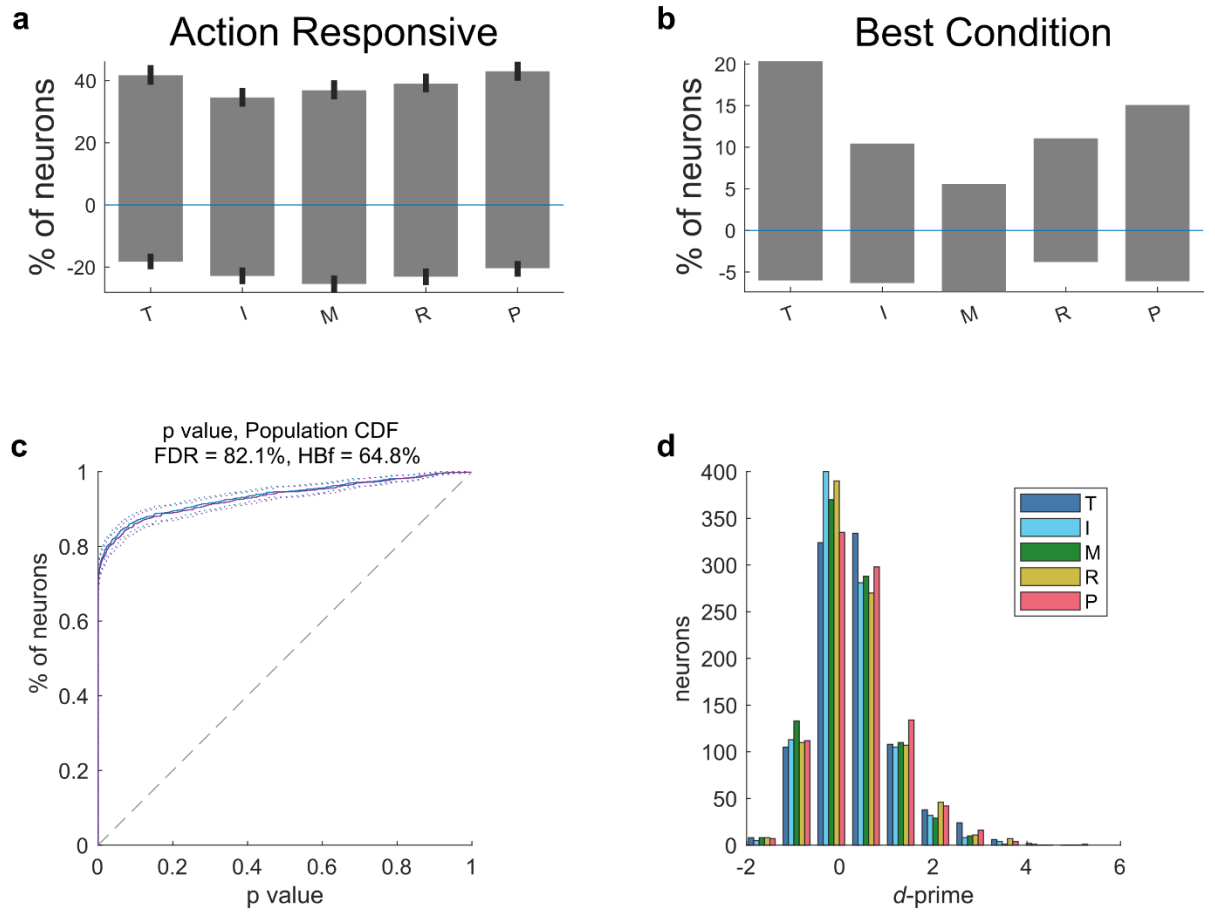

Supplementary Figure 2.4. Single-neuron encoding of individual fingers.
All five fingers of the right (contralateral) hand were encoded within the population during movement execution.
(**a**) Percentage of the population tuned significantly ($P < 0.05$, FDR-corrected) to flexion of each digit. Positive percentages indicate neurons that increased firing rate during digit movement and negative percentages bar indicate neurons that decreased firing rate. Error bars indicate a 95% bootstrap confidence interval.
(**b**) Percentage of the population tuned best to each digit.
(**c**) Cumulative distribution function of the population's tuning significance p-values.
(**d**) Histogram of d' (discriminability index) values across neurons.
(**a-d**) Neurons were pooled across sessions.

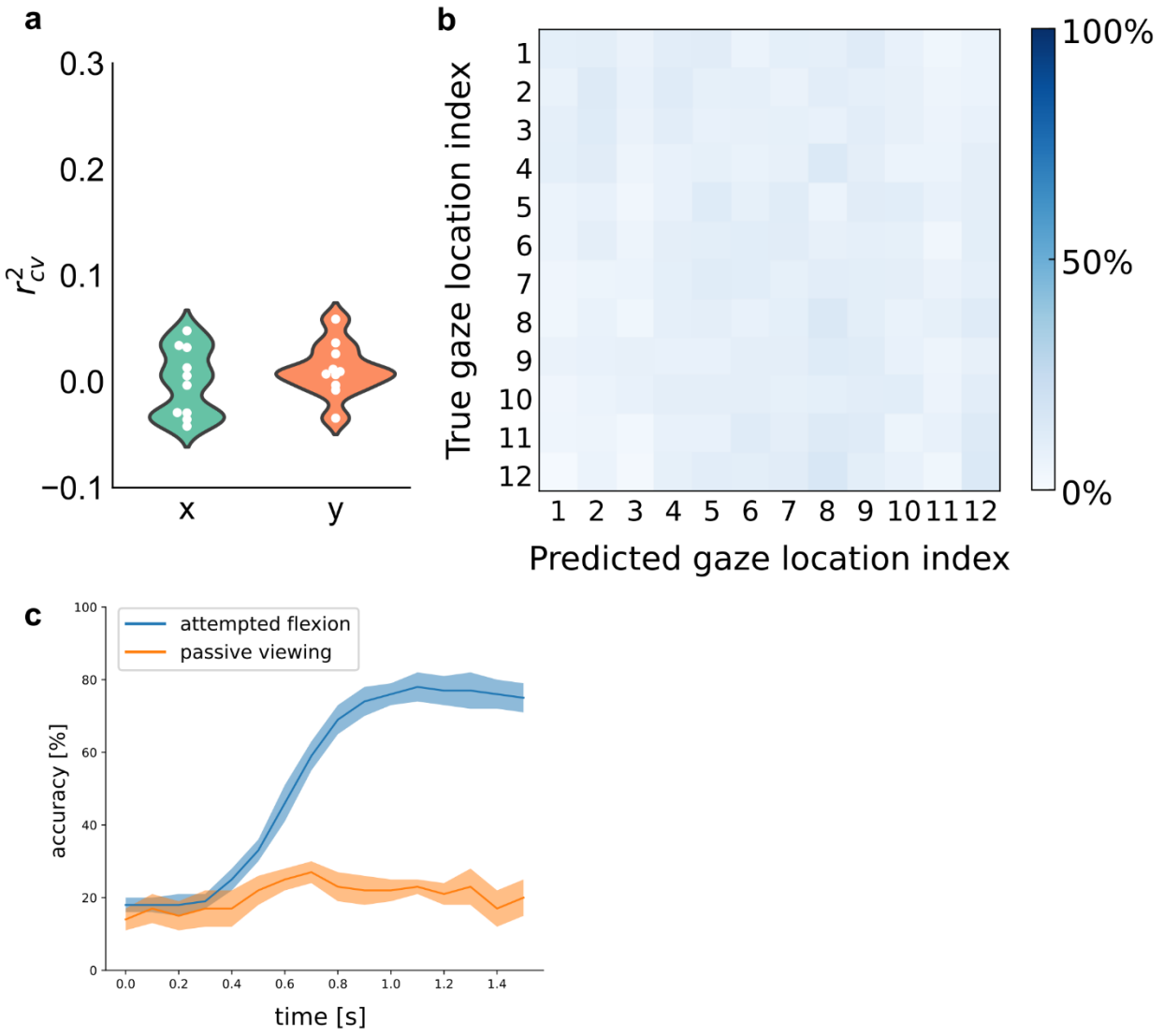

Supplementary Figure 2.5. Gaze location did not affect finger decoding during the attempted-movement period.

(**a**) Linear regression could not decode target location [x, y] coordinates from the neural activity during the attempted-movement period. Violin plot shows that cross-validated regression r^2 values are close to 0 across sessions, with each circle marking a single session.

(**b**) A linear classifier (diagonal LDA) could not classify the gaze location from neural activity during the attempted-movement period. Confusion matrix depicts cross-validated classifications of cue location.

(**c**) Cross-validated classification accuracy for main and control tasks: a linear classifier (diagonal LDA) could not classify finger movements from neural activity during passive observation (orange) of the digit flexion task. Sliding bin width: 200ms. The shaded region indicates +/- s.e.m. (6 sessions passive viewing, 10 sessions attempted flexion).

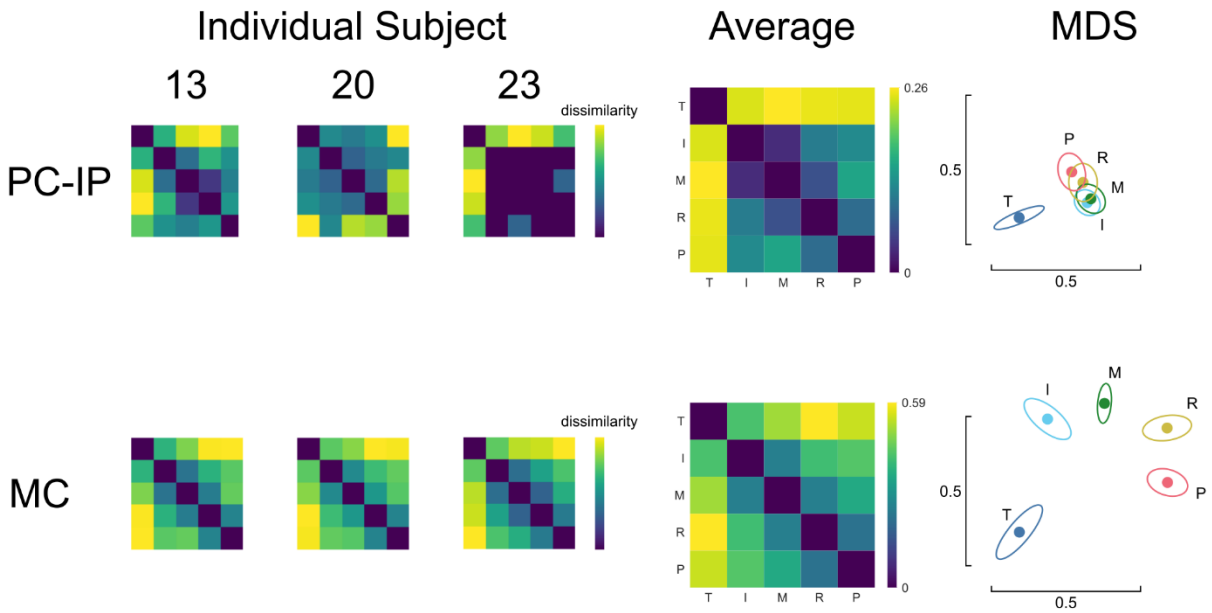

Supplementary Figure 2.6. fMRI representational structure for finger movements, from (Kieliba et al., 2021)

fMRI representational dissimilarity matrices (RDMs) for 3 individual subjects and the group mean (N = 29). Intuitive visualization of distances using multidimensional scaling (MDS) and Generalized Procrustes alignment (without scaling); ellipses show mean +/- s.d. across subjects. Regions of interest (ROIs): motor cortex (MC, top row) and junction of the postcentral and intraparietal sulci (PC-IP, bottom row).

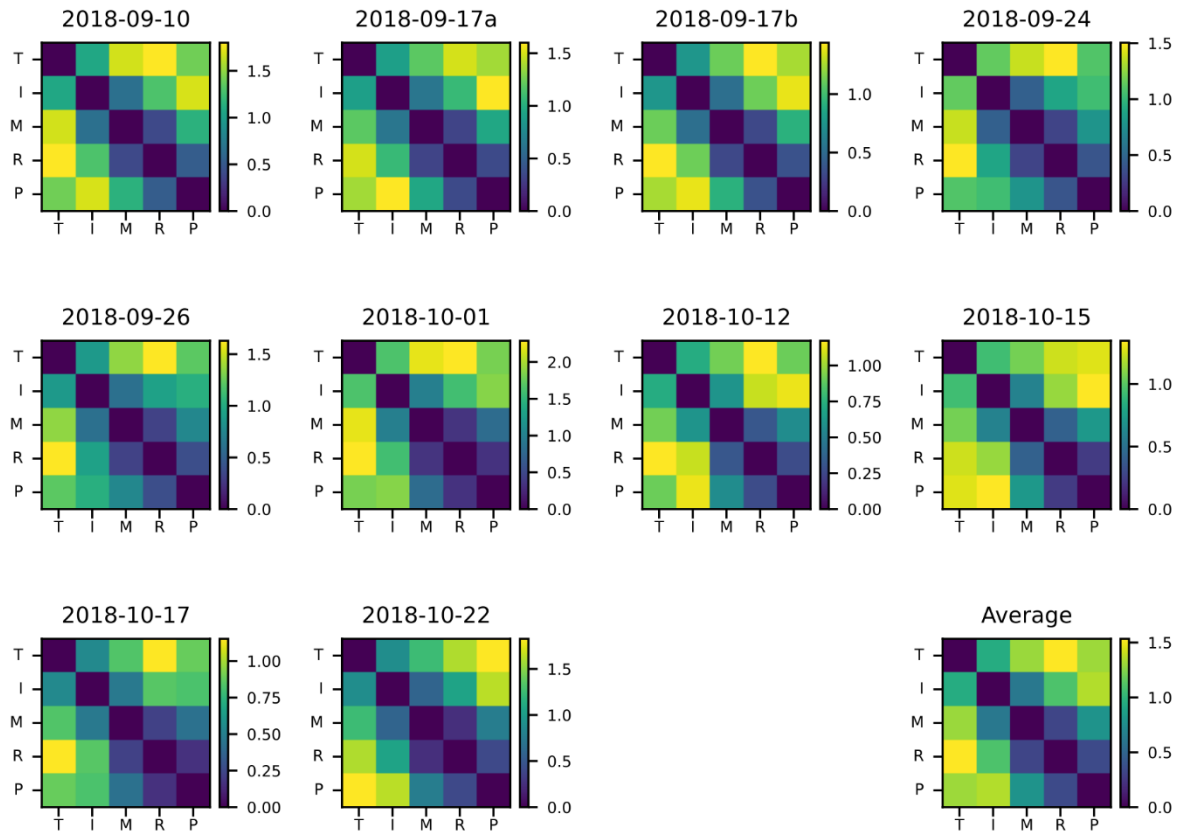

Supplementary Figure 2.7. Individual representational dissimilarity matrices for each session.

Representational dissimilarity matrices across all sessions, using the cross-validated Mahalanobis distance. "Average" RDM matches Figure 2.2d.

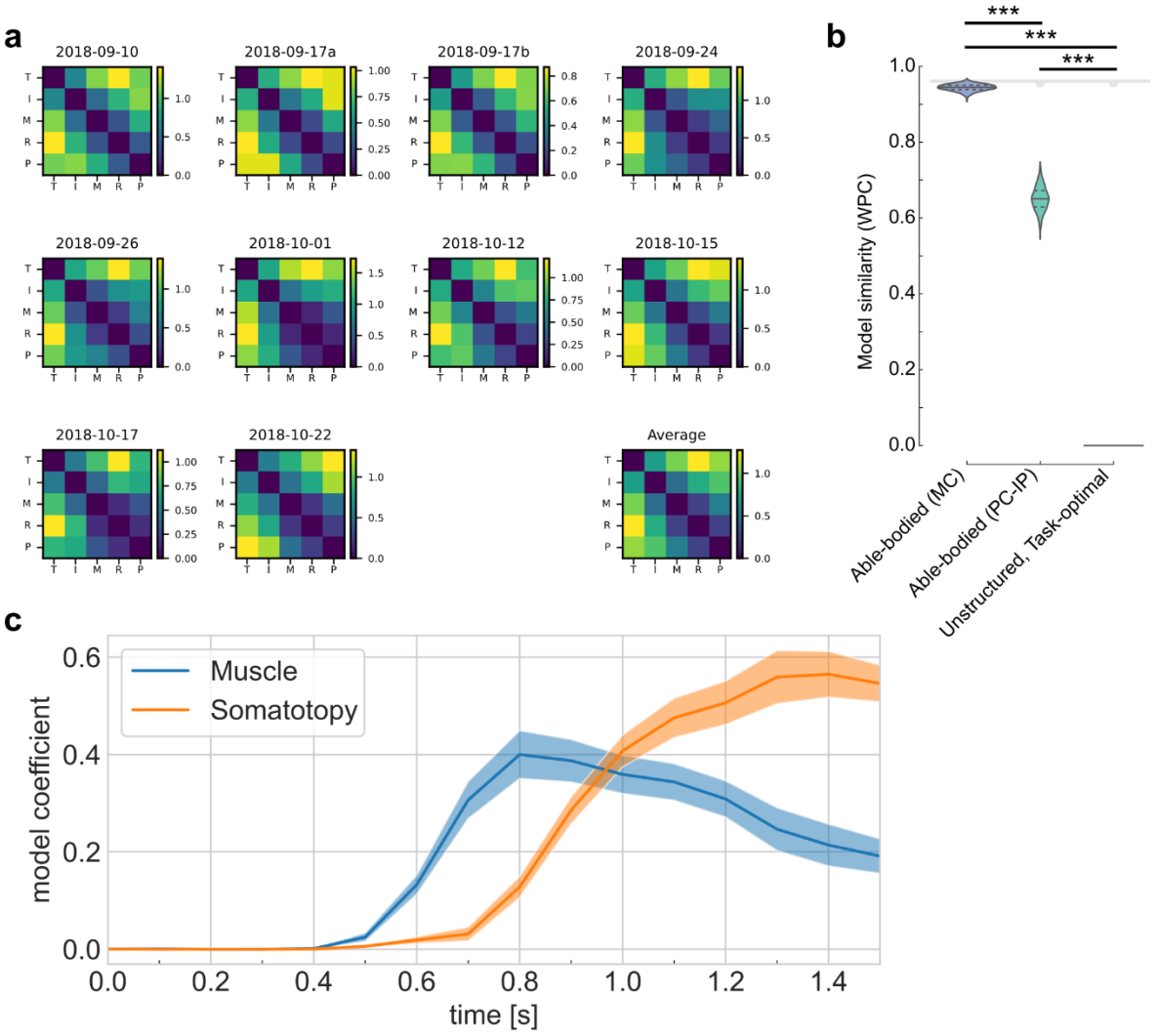

Supplementary Figure 2.8. Representational structure during BCI finger control matches the structure of able-bodied individuals when using alternative analysis parameters.

(**a**) RDMs calculated with an alternative dissimilarity metric: cross-validated Poisson KL-divergence (Schütt et al., 2019). Units: nats / neuron. Related to Supplementary Figure 2.7a and Figure 2.2d.

(**b**) Fit between measured RDMs and motor-intact BOLD data using alternative metrics. Distance metric: cross-validated Poisson KL-divergence. Similarity metric: whitened RDM Pearson correlation (Diedrichsen et al., 2021). Similar to Figure 2.2f.

(**c**) Representational dynamics calculated with an alternative dissimilarity metric: cross-validated Poisson KL-divergence. Similar to Figure 2.4e.

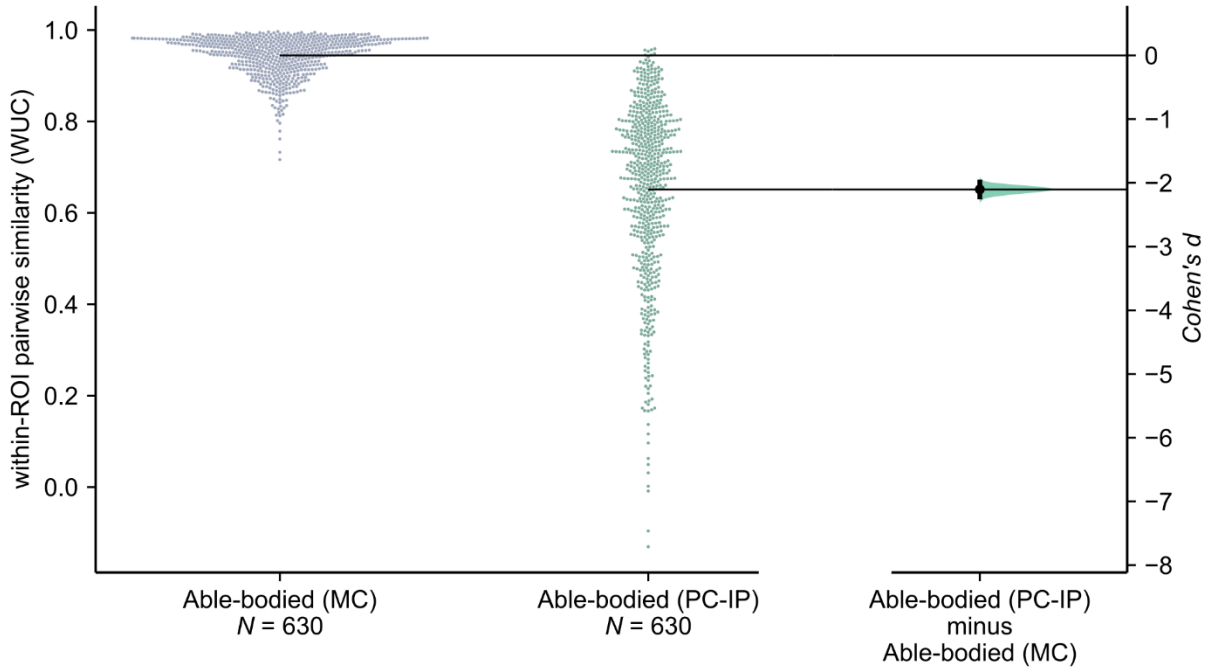

Supplementary Figure 2.9. fMRI finger RDMs are more consistent across able-bodied participants in MC than in PC-IP

Gardner-Altman estimation plot (Ho et al., 2019) of the WUC similarity between same-ROI pairs of RDMs (N = 630 pairs between 36 subjects). Each circle on the swarm plot (left) marks the similarity for a pair of subjects. Horizontal black lines mark the mean pairwise similarity within each ROI. The curve (right) indicates the resampled (N = 5000) distribution of the effect size between ROIs, as measured by Cohen's d. Cohen's d of PC-IP minus MC: –2.1 (95% CI: [–2.22, –1.99]).

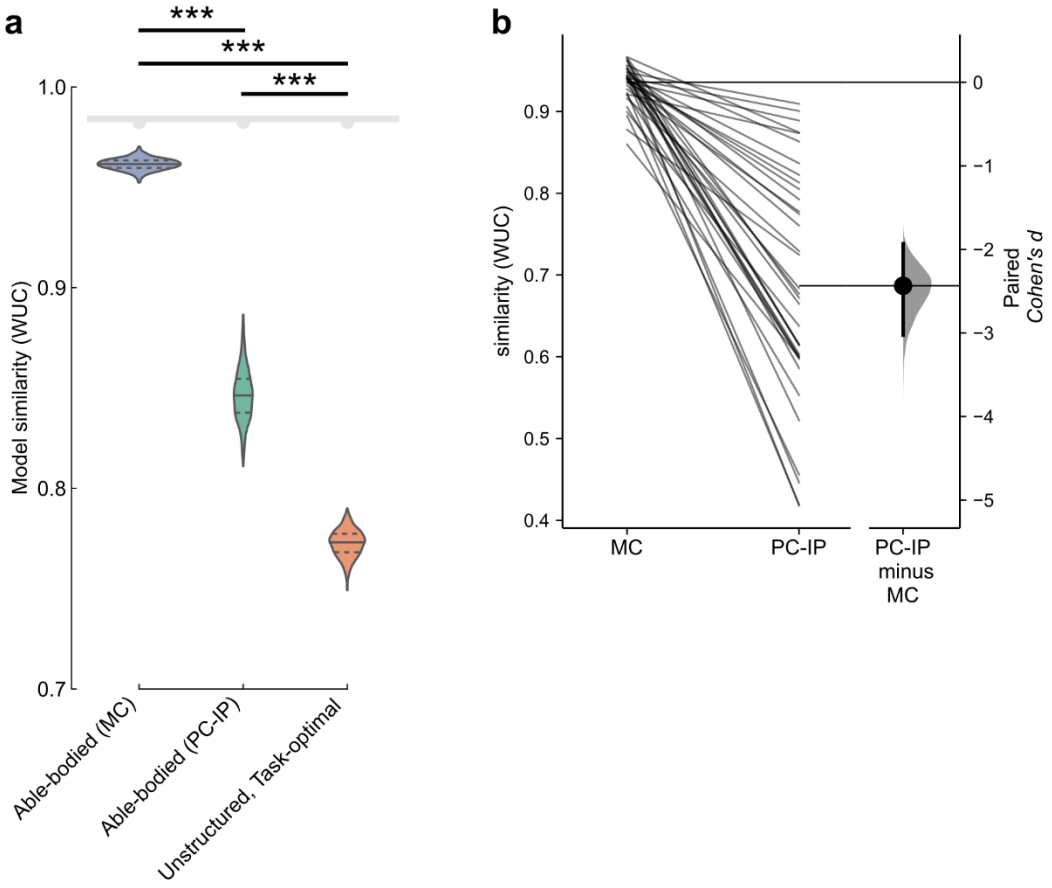

Supplementary Figure 2.10. PC-IP finger representational structure of tetraplegic individual matches fMRI RDMs from MC even better than fMRI RDMs from PC-IP.

(**a**) Measured RDMs match the able-bodied MC fMRI RDM better than they match the able-bodied PC-IP fMRI RDM ($P = 1.9 \times 10^{-6}$; two-tailed t-test, 1000 bootstrap samples over 10 sessions), as measured by the whitened unbiased cosine similarity (Diedrichsen et al., 2021) (WUC) (Methods). Violin plot: solid horizontal lines indicate the median WUC over bootstrap samples, and dotted lines indicate the first and third quartiles. Noise ceiling: gray region estimates the best possible model fit (Methods). Similar to Figure 2.2f.

(**b**) Paired Gardner-Altman estimation plot (Ho et al., 2019) of the similarity (WUC) between participant NS (average RDM across sessions) and individual MC and PC-IP RDMs from able-bodied fMRI participants. The slopegraph's connected points (left) show each fMRI participant's (N = 36) MC and PC-IP similarities with participant NS's mean finger RDM. Mean difference between PC-IP and MC similarities (right) presented as Cohen's d (N = 5000 bootstrap samples).

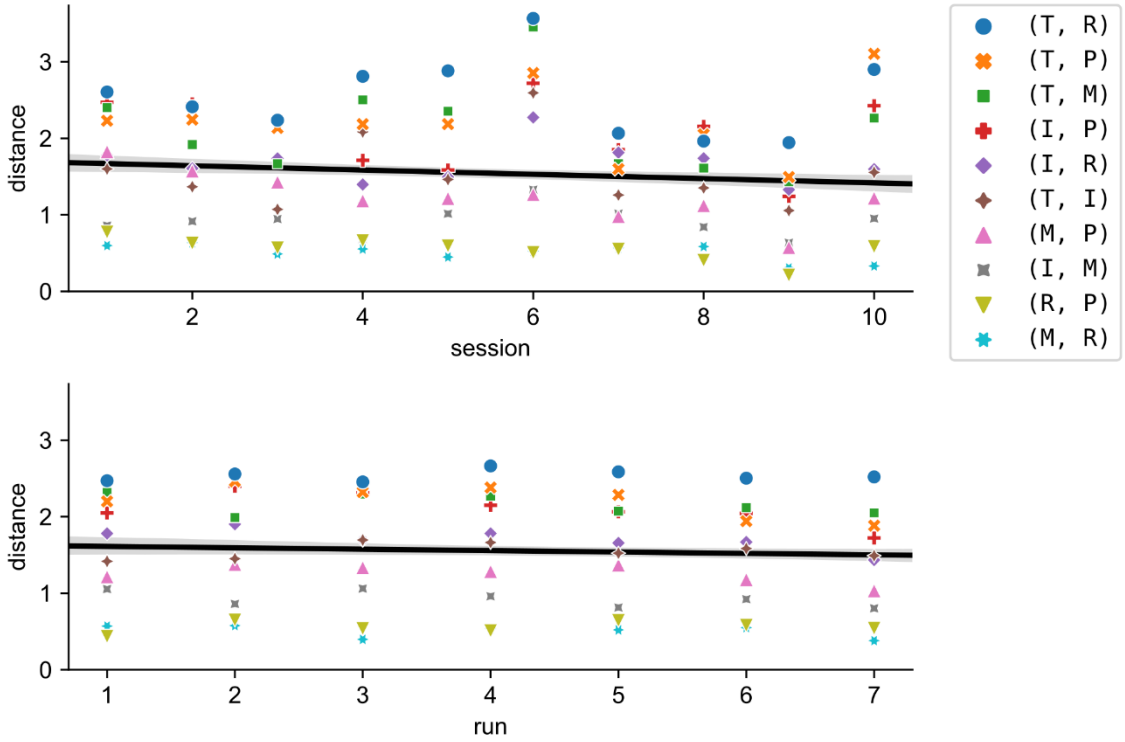

Supplementary Figure 2.11. Inter-finger distances did not increase across sessions or within sessions.
BCI classification errors could have encouraged inter-finger distances to increase to improve separability, but this did not occur. Inter-finger distances instead decreased slightly (across sessions: t(8) = –4.0, two tailed t-test P = 0.004; across runs within sessions: $t(82) = -2.4$, two-tailed t-test P = 0.019), although the effect size was very small (across sessions: Cohen's $f^2 = 0.008$; across runs within sessions: = 0.005). Markers indicate average pairwise distance for each finger pair and session (top) or run-within-session (bottom).

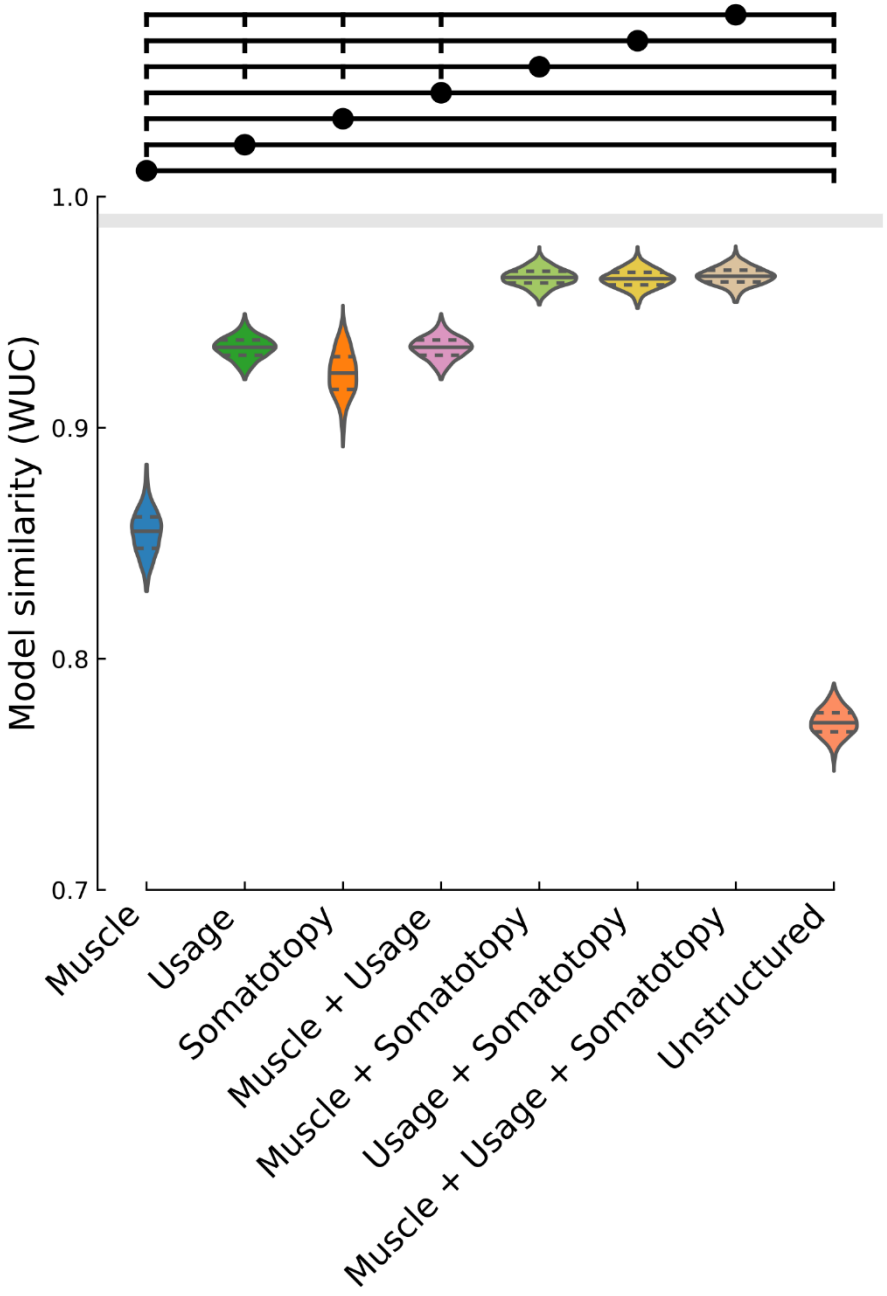

Supplementary Figure 2.12. Fit between measured RDM and linear combinations of models. Violin plot of WUC similarity between the measured RDM (N = 1000 bootstrap samples over 10 sessions) and the corresponding model combination. Violin plot: solid horizontal lines indicate the mean WUC over bootstrap samples, and dotted lines indicate the first and third quartiles. Horizontal lines (above) indicate significance groups, where the circle-indicated model is significant over the vertical-tick-indicated models (two-tailed t-test, $q < 0.01$, FDR-corrected for 28 model-pair comparisons). For example, the muscle+somatotopy combined model is significant over the individual muscle, hand usage, somatotopic, combined muscle+hand-usage, and pairwise-equidistant/unstructured (null) models.

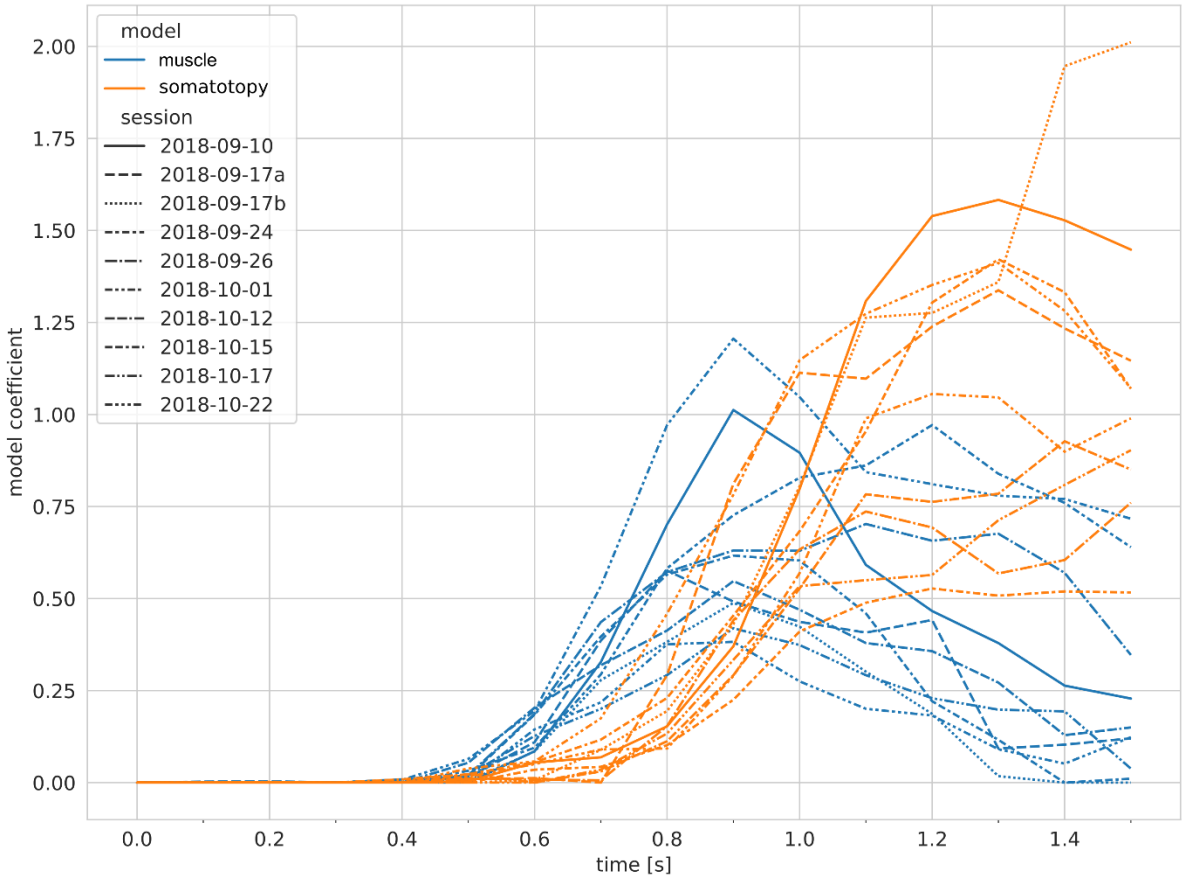

Supplementary Figure 2.13. Temporal delays between component models are consistent across single sessions.

When linear modeling within single sessions, the muscle model (blue) consistently preceded the somatotopic model (orange). Time difference: 170ms +/- 66ms (s.d. across sessions) (P = 0.002, two-sided Wilcoxon signed-rank test). Line styles indicate session. Related to Figure 2.4e.

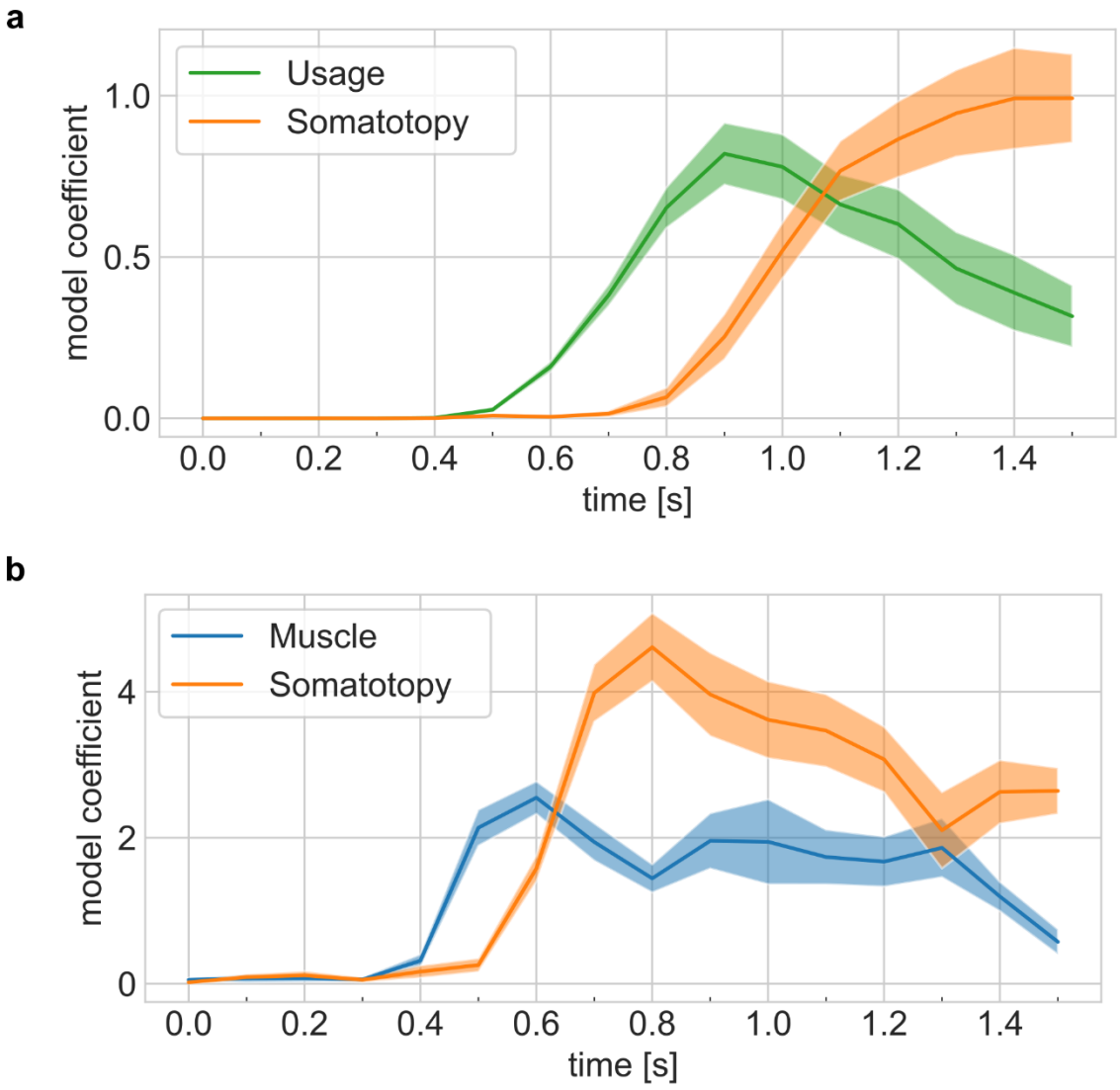

Supplementary Figure 2.14. Representational dynamics are robust across tasks and model combination choices.

(**a**) Representational dynamics analysis shows an early fit to the hand-usage model and a late fit to the somatotopic model. Confidence intervals indicate +/- s.e.m. across sessions. Related to Figure 2.4e.

(**b**) Representational dynamics analysis shows a consistent delay between models during the calibration task. Note: the absolute timing differs from the main task because the calibration task does not require an initial saccade to read the cue. Related to Figure 2.4e.

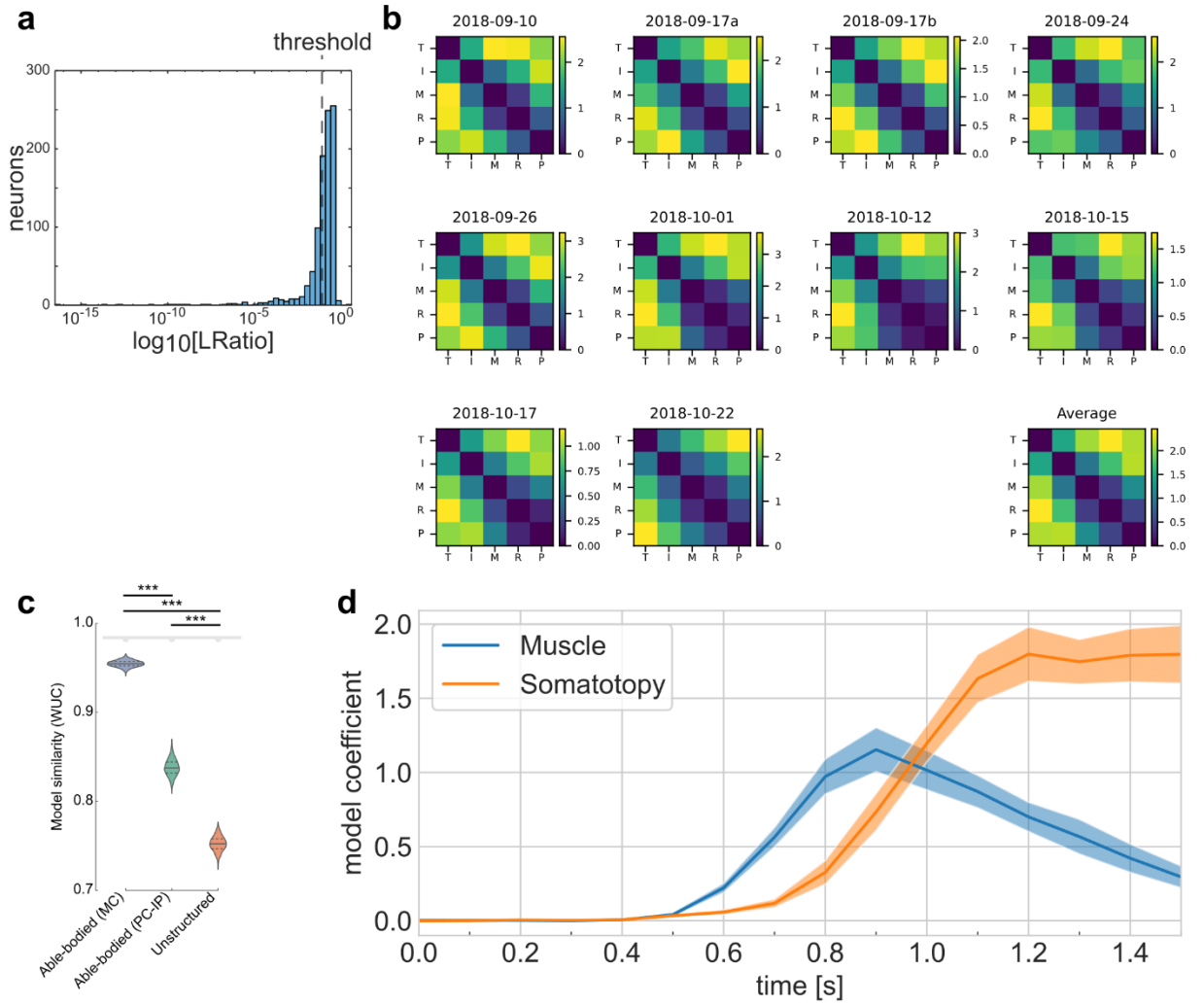

Supplementary Figure 2.15. Well-isolated single neurons of the tetraplegic participant match the finger representational structure of able-bodied individuals.

(**a**) Histogram of L-ratio, a spike-sorting cluster metric. Threshold for well-isolated units: 33% quantile ($L_{ratio} < 10^{-1.1}$).

(**b**) Representational dissimilarity matrices calculated only using well-isolated units, using the cross-validated Mahalanobis distance. Similar to Figure 2d and Supplementary Figure 2.7a.

(**c**) Whitened unbiased similarity (WUC) between measured (b) RDMs (using only well-isolated units) and model predictions (Figure 2b-c), showing that the measured RDMs match the able-bodied fMRI RDM significantly better than they match the unstructured model ($P = 3.1 \times 10^{-10}$, two-tailed t-test) and the SPLa fMRI RDM ($P = 1.7 \times 10^{-8}$). Error bars indicate +/- s.e.m. Noise ceiling: gray region estimates the best possible model fit (Methods). Gray downward semicircle indicates that the noise ceiling is significantly higher ($P < 0.001$) than the fit of the SPLa fMRI RDM and the unstructured model. Similar to Figure 2.2f.

(**d**) Representational dynamics analysis, repeated using only well-isolated units, shows an early fit to the muscle model and a late fit to the somatotopic model. Confidence intervals indicate +/- s.e.m. across sessions. Similar to Figure 2.4e.

3 Decoding and geometry of ten finger movements in human posterior parietal cortex and motor cortex

3.1 Summary

Objective. Enable neural control of individual prosthetic fingers for participants with upper-limb paralysis.
Approach. Two tetraplegic participants were each implanted with a 96-channel array in the left posterior parietal cortex (PPC). One of the participants was additionally implanted with a 96-channel array near the hand knob of the left motor cortex (MC). Across tens of sessions, we recorded neural activity while the participants attempted to move individual fingers of the right hand. Offline, we classified attempted finger movements from neural firing rates using linear discriminant analysis (LDA) with cross-validation. The participants then used the neural classifier online to control individual fingers of a brain-machine interface (BMI). Finally, we characterized the neural representational geometry during individual finger movements of both hands.
Main Results. The two participants achieved 86% and 92% online accuracy during BMI control of the contralateral fingers (chance = 17%). Offline, a linear decoder achieved ten-finger decoding accuracies of 70% and 66% using respective PPC recordings and 75% using MC recordings (chance = 10%). In MC and in one PPC array, a factorized code linked corresponding finger movements of the contralateral and ipsilateral hands.
Significance. This is the first study to decode both contralateral and ipsilateral finger movements from PPC. Online BMI control of contralateral fingers exceeded that of previous finger BMIs. PPC and MC signals can be used to control individual prosthetic fingers, which may contribute to a hand restoration strategy for people with tetraplegia.

3.2 Introduction

Tetraplegic individuals identify hand function as a high-impact priority for improving their quality of life (Anderson, 2004; Snoek et al., 2004; Collinger et al., 2013a). Neuroprosthetics research has enabled control of basic grasp shapes (Hochberg et al., 2012; Collinger et al., 2013c; Klaes et al., 2015; Wodlinger et al., 2015), an important step towards empowering paralyzed individuals to perform daily activities. However, these predefined grasp templates constrain the range of motion and thus limit the usefulness of existing neural prosthetics.

The complexity of human motor behavior is largely enabled by our versatile, dexterous hands (Sobinov and Bensmaia, 2021). The human hand can weave intricate crafts, sign expressive languages, and fingerpick guitar solos. Even everyday manual behaviors, like turning a door handle, require volitional control over many degrees of freedom (Yan et al., 2020). Indeed, humans can move individual fingers much more independently than other animals, including monkeys (Schieber, 1991; Häger-Ross and Schieber, 2000). To better restore autonomy to people with tetraplegia, neural prosthetics would benefit from enabling dexterous finger control.

Intracortical brain-machine interface (BMI) research has largely focused on control of computer cursors and robotic arms, rather than dexterous hand control. Building off foundational

studies of non-human primates (Wessberg et al., 2000; Serruya et al., 2002; Taylor et al., 2002; Wu et al., 2004; Mulliken et al., 2008b; Ethier et al., 2012; Gilja et al., 2012), several clinical studies have implemented continuous decoders for cursor control (Hochberg et al., 2006; Kim et al., 2008; Wang et al., 2013; Aflalo et al., 2015; Gilja et al., 2015). Leveraging this cursor control, (Jarosiewicz et al., 2015; Pandarinath et al., 2017; Nuyujukian et al., 2018) subsequently developed on-screen keyboard typing interfaces for tetraplegic participants. (Hochberg et al., 2012; Collinger et al., 2013c; Wodlinger et al., 2015; Ajiboye et al., 2017) extended continuous decoding to arm control, with (Ajiboye et al., 2017) controlling the user's own muscles. Recent work has also decoded speech from sensorimotor cortex (Anumanchipalli et al., 2019; Moses et al., 2021; Sarah K. Wandelt et al., 2022; Willett et al., 2023). However, relatively few BMI studies have focused on hand control (Bouton et al., 2016; Hotson et al., 2016; Irwin et al., 2017; Jorge et al., 2020; Nason et al., 2021; Willett et al., 2021), and previous studies frequently combine the ring and little fingers or leave them out altogether. Individuated finger control would be useful for applications like keyboard typing or object manipulation.

Most motor BMIs record neural activity from the motor cortex (MC), although areas of the posterior parietal cortex (PPC) have also been used successfully for BMI control of reaching (Mulliken et al., 2008b; Aflalo et al., 2015) and grasping (Klaes et al., 2015). The PPC plays a central role in sensorimotor integration, with regions of PPC representing visual stimulus locations and eye movements (Andersen et al., 1987), task context (Gail et al., 2009), planned reaches (Snyder et al., 1997), and object grasping (Murata et al., 2000; Schaffelhofer and Scherberger, 2016). PPC uses partially mixed selectivity to simultaneously encode many motor variables (Zhang et al., 2017), which can be useful for versatile neural decoding.

Despite PPC's clearly demonstrated role in grasping (Gallese et al., 1994; Schaffelhofer and Scherberger, 2016; Sobinov and Bensmaia, 2021), less is known about PPC responses during individual finger movements. With fMRI, lesion, and anatomical evidence situating primary motor cortex as core to fine finger movements (for review, see (Sobinov and Bensmaia, 2021)), most electrophysiological studies of finger movements have focused on the primary motor (M1) and primary somatosensory cortex (S1) (Schieber and Hibbard, 1993; Schieber and Poliakov, 1998; Flesher et al., 2016; Hotson et al., 2016; Goodman et al., 2019; Fifer et al., 2021; Nason et al., 2021; Willsey et al., 2022). Nevertheless, non-human primate mapping studies (Seelke et al., 2012) and stimulation studies (Rathelot et al., 2017; Baldwin et al., 2018) have identified PPC sub-regions that are likely involved in fine finger movements. These results imply that fine finger movements are supported by a broad neuronal network, which should be investigated to improve dexterous BMI control.

Here, we recorded intracortical activity from the PPC of two tetraplegic participants while they attempted to press individual fingers. Across task contexts, we could classify individual finger movements during planning and attempted-execution periods. We connected this neural decoder to drive a neural prosthetic hand, with accuracies exceeding recent intracortical BMI studies (Jorge et al., 2020; Guan et al., 2022b). Furthermore, we characterize both the neural tuning and representational geometry (Kriegeskorte and Wei, 2021) during attempted finger movements of either hand. The neural code factorized into finger type and laterality components, leading to finger representations that were simultaneously discriminable and similar across contralateral/ipsilateral

pairs of fingers. These findings contribute to the understanding of human hand movements and advance the development of hand neuroprosthetics for people with paralysis.

3.3 Methods

3.3.1 Study participants

Experiments were conducted with two volunteer participants enrolled in a brain-machine interface (BMI) clinical study (ClinicalTrials.gov Identifier: NCT01958086). All procedures were approved by the respective Institutional Review Boards of California Institute of Technology, Casa Colina Hospital and Centers for Healthcare, and University of California, Los Angeles. Each participant consented to this study after understanding the nature, objectives, and potential risks.

Participant NS is a right-handed, tetraplegic woman. Approximately 10 years before this study, she sustained an AIS-A spinal cord injury at cervical level C3-C4. NS can move her deltoids and above, but she cannot move or feel her hands.

Participant JJ is a right-handed, tetraplegic man. Approximately 3 years before this study, he sustained a spinal cord injury at cervical level C4-C5. He has residual movement in his upper arms, but he cannot move or feel his hands.

Because both participants could not move or feel their hands, we instructed them, during the behavioral tasks, to attempt finger movements as if their fingers were not paralyzed. We often abbreviate these finger movement attempts as "finger movements."

3.3.2 Tasks

3.3.2.1 Alternating-cues finger press task with delay

Each participant performed an instructed-delay finger movement task (Figure 3.1). They were seated in front of a computer monitor display, with their hands prone on a flat surface. Each trial began with a cue specifying a finger of the right hand. The finger cue then disappeared during a delay period. A cue-invariant go-icon appeared, instructing the participant to attempt to press the cued finger as though pressing a key on a keyboard. This instructed-delay task format temporally separates the visual stimulus from the planning and execution epochs.

Supplementary Table 3.1 documents the phase durations for each task, and Supplementary Table 3.2 lists the date ranges for each task.

Some regions of the posterior parietal cortex (PPC) are modulated by non-motor variables like visual stimulus location (Andersen et al., 1987) and task context (Gail et al., 2009). To ensure that the recorded neural signals reflected movement type (rather than, e.g., visual memory), we varied the cueing method between runs (Figure 3.1). In the Spatial-Cue variant, five circles corresponded to the five fingers. In the Text-Cue variant, the finger cue was a letter abbreviation. A brief Pre-Cue phase in each trial indicated what cue variant the trial would be.

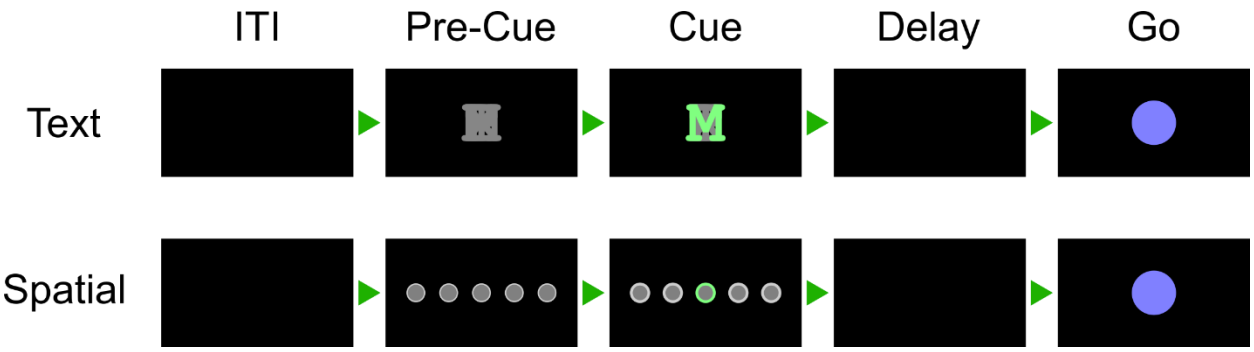

Figure 3.1. Alternating-cues, instructed-delay finger press task
Trial structure. Each rectangle represents the computer monitor display at each phase. Two cue variants, text and spatial, were trial-interleaved. In the spatial variant, the location of the highlighted circle corresponded to the cued finger. Trials without a highlighted circle indicated a No-Go cue. In the text variant, a highlighted letter (for example, "M" for the middle finger) cued each finger. In both variants, the finger cue disappeared before the movement phase (Go) to separate planning and execution periods. Phase durations are listed in Supplementary Table 3.1.

3.3.2.2 Finger press task with randomized cue location (reaction-time)

Letters, corresponding to each movement type, were arranged in a 3 x 4 grid across the screen. Each grid consisted of two repetitions each of T (thumb), I (index), M (middle), R (ring), P (pinky), and X (No-Go). Letters were arranged in a random order to dissociate eye gaze signals from movement representations. On each trial, a single letter cue was indicated with a crosshairs symbol, which was jittered to minimize systematic effects of letter occlusion. Each cue was selected once (for a total of 12 trials) before the screen was updated to a new arrangement. Each run-block consisted of 4 screens for a total of 48 trials.

On each trial, the participant was instructed to immediately saccade to the cued target and fixate, then attempt to press the corresponding finger of the right hand. A trained classifier decoded the finger movement from neural signals and displayed the classified finger movement 1.5 seconds after the start of the trial. The participant pressed the instructed finger and fixated on the cue until the visual classification feedback was shown.

Data from participant NS performing this task was previously analyzed in (Guan et al., 2022b). Data from participant JJ have not been reported previously. During 3 sessions, participant JJ also performed this task using his left hand.

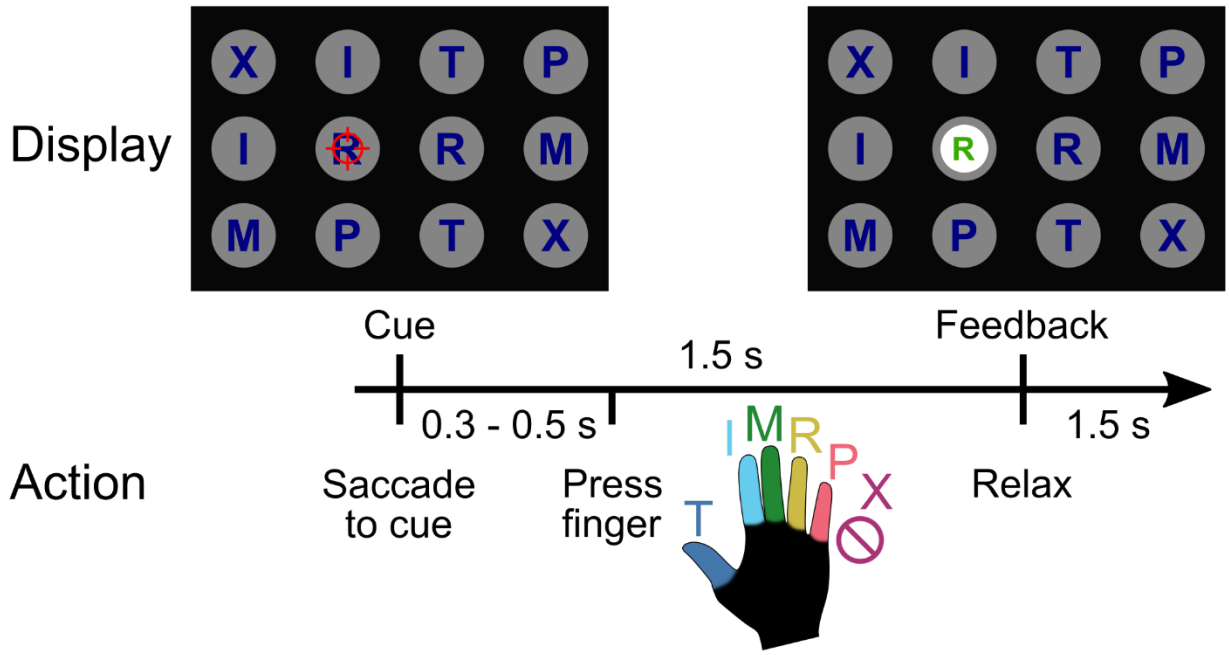

Figure 3.2. Reaction-time finger-press task with randomized cue location. Figure adapted from (Guan et al., 2022b) (CC BY-NC 4.0).
Main finger press task. When a letter was cued by the red crosshair, the participant looked at the cue and immediately attempted to flex the corresponding digit of the right (contralateral) hand. We included a No-Go condition "X," during which the participant looked at the target but did not move their fingers. Visual feedback indicated the decoded finger 1.5 seconds after cue presentation. To randomize the saccade location, cues were located on a grid (3 rows, 4 columns) in a pseudorandom order. The red crosshair was jittered to minimize visual occlusion.

3.3.2.3 Ten-finger press task

Each participant also performed an instructed-delay finger press task with fingers from both hands. The task was like the Text-Cue variant of the Alternating-cues finger press task with delay, except without a Pre-Cue phase. All ten fingers were interleaved in trials within the same run-block (Figure 3.3). Phase durations are documented in
Supplementary Table 3.1.

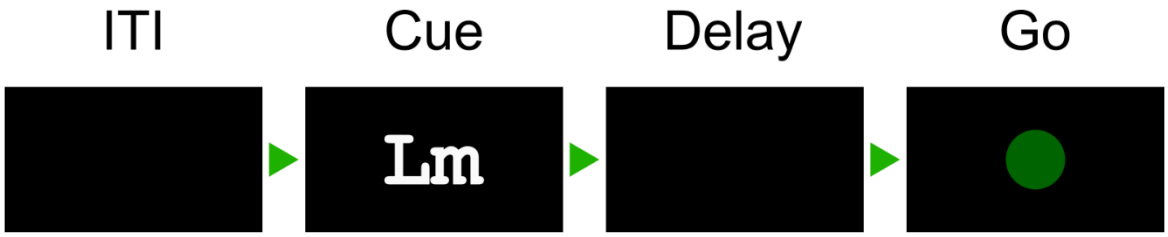

Figure 3.3. Text-cued finger movement task with instructed-delay.
Trial structure. Text cues indicate the hand ("R" or "L") and the finger (e.g., "m" for middle finger). After a delay period, a cue-invariant Go-icon instructs movement execution.

3.3.3 Implant location

Participant NS was implanted with two 96-channel NeuroPort Utah electrode arrays 6 years after injury (about 4 years before this study). The implant locations were determined using anatomical priors and preoperative functional magnetic resonance imaging (fMRI) (Guan et al., 2022b). One array (denoted NS-PPC) was implanted over the hand/limb region of PPC at the junction of the intraparietal sulcus (IPS) with the postcentral sulcus (PCS). This region is thought to be involved in the planning of grasp movements (Klaes et al., 2015; Schaffelhofer and Scherberger, 2016; Cavina-Pratesi et al., 2018). In this report, we refer to this brain area as PC-IP (postcentral-intraparietal), although it is sometimes also referred to as the anterior intraparietal sulcus (aIPS) region (Gallivan et al., 2013). A second array was in Brodmann's area (BA) 5d. In the weeks following implantation, it was found that the BA 5d array did not function, so only the PC-IP array was used in this study.

Participant JJ was implanted with two 96-channel NeuroPort Utah electrode arrays about 20 months after injury (about 35 months before this study). The first array (denoted JJ-PPC) was implanted in the superior parietal lobule (SPL) of the left PPC. The second array (denoted JJ-MC) was implanted near the hand knob of the left motor cortex (MC) (Supplementary Figure 3.1). PPC and MC activity were recorded simultaneously.

3.3.4 Neural signal recording and preprocessing

Neural signals were acquired, amplified, bandpass-filtered (0.3 Hz - 7.5 kHz) and digitized (30 kHz, 16-bits/sample) from the electrodes using NeuroPort Neural Signal Processors (NSP) (Blackrock Microsystems Inc.).

Action potentials (spikes) were detected by high-pass filtering (250Hz cut-off) the full-bandwidth signal, then thresholding at –3.5 times the root-mean-square (RMS) voltage of the respective electrode. Although one or more source neurons may generate threshold crossings, we used raw threshold crossings for online control and only sorted spikes for offline analyses. Single neurons were identified using the k-medoids clustering method. We used the gap criteria (Tibshirani et al., 2001) to determine the total number of waveform clusters. Clustering was performed on the first $n \in \{2, 3, 4\}$ principal components, where n was selected to account for 95% of waveform variance.

3.3.5 Feature Extraction

Except when otherwise specified, we used a 500-millisecond (ms) window of neural activity to calculate firing rates (counted spikes divided by the window duration). The firing rate was then used as the input features to each analysis or classification model.

For cross-validation classification analyses, neurons with an average firing rate on the training fold < 1 Hz were discarded as noisy features. For single-neuron analyses, a looser threshold of < 0.5 Hz, averaged over the entire recording, was used to exclude neurons from significance and effect size tests.

Behavioral epochs: the movement execution ("Go" or "move") analysis window was defined as the 500-ms window starting 200 ms after the Go cue. For applicable tasks, the movement planning ("Delay" or "plan") analysis window was defined as the 500-ms window starting 200 ms after the Delay screen. The Cue analysis window was defined as the 500-ms window starting 200 ms after the Cue screen. The intertrial interval (ITI) analysis window was defined as the last 500 ms of the ITI phase.

3.3.6 Single-neuron selectivity for finger movements

In the section "Single-neuron modulation to individual finger presses," we used a one-way ANOVA to determine whether neurons distinguished firing rates between attempted finger movements. A neuron was considered discriminative if $p < 0.05$ after false discovery rate (FDR) correction for multiple comparisons using the Benjamini–Hochberg procedure; we also denoted this FDR-adjusted p-value as q. We corrected for $m=N$ comparisons, where N is the number of neurons for each participant. Following Cohen's rules of thumb (Cohen, 1988), we denoted the ANOVA effect size as "large" if $\eta^2 > 0.14$. As the ANOVA post hoc test, we used Dunnett's multiple comparison test (Dunnett, 1964) to determine which fingers had significantly different firing rates than the No-Go baseline.

To quantify the effect size of firing-rate changes against the No-Go baseline (Figure 3.4a), we used Hedges' g, which is similar to Cohen's d but bias-corrected for small sample sizes. We calculated and visualized Hedges' g values using the Data Analysis using Bootstrap-Coupled Estimation Python library (Ho et al., 2019).

For visual simplicity, we pooled neurons across sessions when calculating and visualizing single-neuron metrics (percentage selective, number of fingers discriminable from No-Go, empirical cumulative distribution functions).

To visualize firing rates, spike rasters were smoothed with a Gaussian kernel (50-ms standard-deviation [S.D.]), then averaged across trials to create a peristimulus time histogram (PSTH).

3.3.7 Offline classification with cross-validation

We trained a separate linear classifier for each session to predict attempted finger movements from the neural features. We used diagonal-covariance linear discriminant analysis (diagonal LDA) (Dudoit et al., 2002); Diagonal LDA is equivalent to Gaussian Naive Bayes (GNB) when GNB shares a single covariance matrix across classes.

For offline classification and parameter sweeps, we estimated the generalization error using stratified K-Folds cross-validation (with K = 8) within each session. Reported classification accuracies indicate the number of correct trials (summed across sessions) divided by the total number of trials (summed across sessions). Across-session standard deviations of classification accuracy are weighted by the number of trials in each session.

Learning curves (Figure 3.5b) were generated by using subsets of the training set during each Stratified K-Fold split. Window duration sweeps (Figure 3.5d) varied the size of the firing-rate estimation window while fixing the start time at 200ms after the Go cue. Neural decode time-courses (Figure 3.5e) used 500ms bins centered at different times of the trial.

To visualize neuron-dropping curves (Figure 3.5c, Supplementary Figure 3.11), we first aggregated neurons across sessions into a pseudo-population. Specifically, we combined trials from different sessions based on their within-finger order. For example, each session's first right-thumb trial was combined into a single trial for the pseudo-population. For the Alternating-cues finger press task with delay, Participant JJ performed 96 trials in 1 session and 120 trials in 2 sessions, so we used only the first 96 trials from each session. Finally, we randomly sampled (without replacement) an *M*-neuron subpopulation from the pseudo-population. We calculated the cross-validated accuracy when decoding from this subpopulation. We varied *M* to create a neuron-dropping curve, and we repeated the subpopulation sampling 40 times for each *M* to generate confidence intervals.

3.3.8 Online brain-machine interface (BMI) discrete control

Each BMI control session started with a run of the open-loop calibration task. For participant NS, this was the Alternating-cues finger press task, modified to not have a delay. For participant JJ, this was the finger press task with randomized cue location, modified to not provide classifier output.

The neural activity and finger movement cues from the calibration task served as training data for the online BMI classification model. Neural features were composed of the threshold crossing rates of each electrode during a 1-second window for each trial. The window start-time, t_s, was a hyperparameter chosen to maximize the cross-validated classification accuracy on the calibration task. The online BMI classifier was then fit to the calibration task without cross-validation. Labels consisted of the finger movement cues, and features consisted of the firing rates during each trial's window $[t_s, 1 + t_s]$. Electrodes with mean firing rates < 1 Hz were excluded to minimize sensitivity to discretization.

During online control of the finger grid task, the classifier predicted a single finger movement for each trial. Input neural features consisted of the threshold crossing rates from each electrode in the time window [0.5, 1.5] seconds after cue presentation. The BMI classifier was occasionally recalibrated between run blocks using data from this task.

3.3.9 Neural distance between fingers

We quantified the neural activity differences between finger movements using the cross-validated (squared) Mahalanobis distance (Walther et al., 2016). The Mahalanobis distance is a continuous, non-saturating analogue of LDA classification accuracy (Nili et al., 2014). Cross-validation removes the positive bias of standard distance metrics, such that $E[d_{jk}^2] = 0$ when two activity patterns are statistically identical.

To calculate population distances, we used the representational similarity analysis Python toolbox (Schütt et al., 2019). The toolbox slightly modifies the cross-validated Mahalanobis equation, incorporating the noise covariances of both folds to improve robustness:

$$d_{jk}^2 = \left(b_j - b_k\right)_A \left(\frac{\Sigma_A + \Sigma_B}{2}\right)^{-1} \left(b_j - b_k\right)_B^T / N$$

Equation 3.1

where A and B indicate independent partitions of the trials, Σ is the noise covariance matrix, (b_j, b_k) are the firing rate vectors for finger movements (j, k) stacked across trials, and N normalizes for the number of neurons. The units of d_{jk}^2 are $\text{unitless}^2/\text{neuron}$.

3.3.10 Shared representations across hands

To quantify whether finger representations were similar across hands, we compared the pairwise distances between matching finger pairs and the pairwise distances between non-matching finger pairs (Figure 3.8b). We denoted a finger pair as matching if the hands differed and the finger-types were the same ([Lt, Rt], [Li, Ri], [Lm, Rm], [Lr, Rr], [Lp, Rp]). We denoted a finger pair as non-matching if the hands differed and the finger-types also differed ([Lt, Ri], [Lt, Rm], [Lt, Rr], [Lt, Rp], [Li, Rt], [Li, Rm], etc.). We described a neural population as sharing representations across hands if the average distance between matching finger pairs was smaller than the average distance between non-matching finger pairs.

3.3.11 Factorized finger representations

Factorized coding refers to representations that can be decomposed into simpler explanatory factors (Kobak et al., 2016; Kim and Mnih, 2018; Bernardi et al., 2020; Frankland and Greene, 2020; Aflalo et al., 2022). We assessed whether finger representations could be linearly decomposed into the sum of finger-type and laterality components.

We first visualized the representational geometry in Figure 3.8d using 2-D multidimensional scaling (MDS). MDS projects the finger movements into a low-dimensional space while attempting to preserve pairwise neural distances (Figure 3.8a). We performed MDS on data from individual sessions and then used Generalized Procrustes Analysis (GPA) with scaling to normalize and align MDS projections across sessions. In the NS-PPC MDS plot, ellipses show standard error (S.E.) across sessions. The JJ-PPC and JJ-MC MDS plots show the mean values without any S.E. ellipses, because the 2 sessions with participant JJ are not sufficient to estimate the S.E.

We used leave-one-group-out cross-validation to determine whether hand- and finger-dimensions generalize to left-out movements (Supplementary Figure 3.8). If finger representations are factorized, then hand classifiers (left vs. right) should generalize when trained on a subset of finger types and evaluated on left-out finger types. Additionally, finger-type classifiers should generalize when trained on one hand and tested on the other hand (Figure 3.8e). This metric is often called cross-condition generalization performance (CCGP) (Bernardi et al., 2020). We pooled neurons across sessions (NS: 10 sessions; JJ: 2) into a pseudo-population. We used a permutation test to assess whether CCGP was significantly above chance, shuffling the labels repeatedly

(N=1001) to generate a null distribution. Standard cross-validation accuracy provides a best-case upper bound on CCGP. Reaching this upper bound implies perfect factorization. We matched training dataset sizes when comparing CCGP and within-condition cross-validation accuracy.

3.4 Results

3.4.1 Single-neuron modulation to individual finger presses

We first sought to determine whether PPC single neurons discriminate between individual finger movements. We quantified single-neuron modulation to attempted finger presses of the right (contralateral to the implant) hand while the participant performed the Alternating-cues finger press task with delay (participant NS: 120 trials per session for 4 sessions; participant JJ: 112 trials per session [min: 96; max: 120] for 3 sessions). We recorded 118 neurons per session (min: 111; max: 128) over 4 sessions from NS-PPC, 103 neurons per session (min: 92; max: 116) over 3 sessions from JJ-PPC, and 93 neurons per session (min: 90; max: 95) from JJ-MC. For each neuron, we calculated firing rates during the attempted movement period and compared firing rates across finger movements (Figure 3.4a, Supplementary Figure 3.2, Supplementary Figure 3.3).

Like results from finger studies of the motor cortex hand area (Schieber and Hibbard, 1993; Schieber and Poliakov, 1998), PPC neurons were not anatomically segregated by finger selectivity. A large portion of neurons (NS-PPC: 54%; JJ-PPC: 30%; JJ-MC: 78%; Figure 3.4c) varied their firing rates between attempted finger movements ($q < 0.05$), and selective neurons were often selective for multiple finger movements (mean number of significant fingers, NS-PPC: 2.1; JJ-PPC: 1.9; JJ-MC: 2.7). Moreover, many neurons discriminated between movements with large effect sizes (percentage of neurons with $\eta^2 > 0.14$, NS-PPC: 40%; JJ-PPC: 25%; JJ-MC: 64%; Figure 3.4d, Supplementary Figure 3.2d, Supplementary Figure 3.3d).

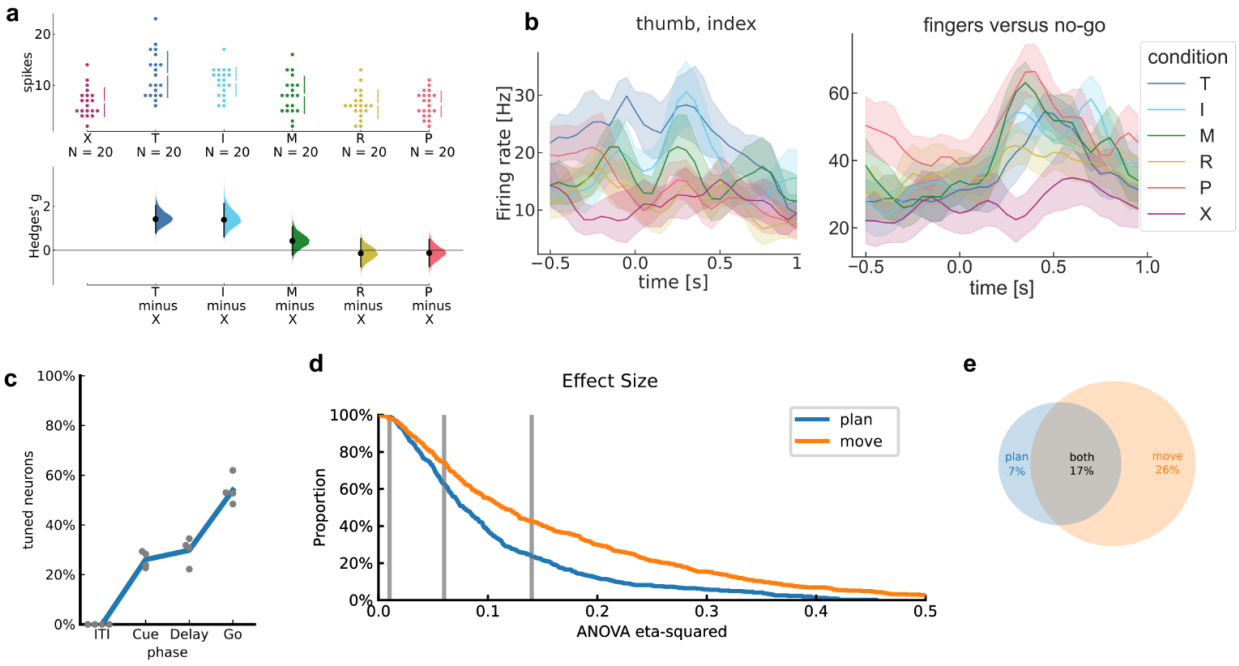

Figure 3.4. PPC single neurons discriminate between attempted finger movements.

a) Single-trial firing rates for an example NS-PPC neuron during attempted movements of different fingers. (top) Markers correspond to the firing rate during each trial. Gapped vertical lines to the right of markers indicate ± S.D., and each gap indicates the mean firing rate. (bottom) Firing rates during thumb (T) and index (I) presses were higher than the No-go (X) baseline. Vertical bars indicate bootstrap 95% confidence intervals (CI) of the effect size versus No-go baseline. Half-violin plots indicate bootstrap distributions.

b) Mean smoothed firing rates for each finger movement for two example NS-PPC neurons, which respectively modulated for thumb/index movements (left) and fingers versus No-Go (right). Shaded areas indicate 95% CI.

c) Percentage of NS-PPC neurons that discriminated between finger movements in each analysis window ($q < 0.05$, FDR-corrected for 466 neurons). Line (blue) indicates mean across sessions. Markers (gray) indicate individual sessions.

d) Complementary empirical cumulative distribution function (cECDF) visualizing the proportion of NS-PPC neurons with ANOVA effect sizes (η^2) above the corresponding x-axis value. Line colors indicate analysis epoch. Vertical lines (gray) indicate Cohen's thresholds (Cohen, 1988) for small (η^2=0.01), medium (η^2=0.06), and large (η^2=0.14) effect sizes.

e) Overlap of NS-PPC neurons that modulated significantly ($q < 0.05$) with large effect sizes ($\eta^2 > 0.14$) during movement preparation (plan) and movement execution (move).

We also quantified single-neuron modulation during movement preparation. Preparatory activity discriminated between finger movements with reasonable effect sizes (Figure 3.4d). Consistent with reaching studies of PPC (Aflalo et al., 2015), slightly fewer NS-PPC neurons had strong tuning ($q < 0.05$ and $\eta^2 > 0.14$) during movement preparation (percentage of neurons: 24%) than during movement execution (percentage of neurons: 43%) (Figure 3.4e). JJ-PPC neurons modulated at similar rates during preparation (percentage of neurons with $q < 0.05$ and $\eta^2 > 0.14$: 23%) versus during execution (24%) (Supplementary Figure 3.2e).

3.4.2 Classifying finger presses from neural activity

Since single neurons were tuned to finger movements, we evaluated whether attempted finger movements could be classified (offline) from the population neural activity. Using data from the same task, we trained linear classifiers and assessed finger classification accuracy on held-out trials using cross-validation (Methods). Classification accuracies substantially exceeded chance (accuracy, NS-PPC: 86%; JJ-PPC: 64%; JJ-MC: 84%; chance: 17%). The majority (NS-PPC: 75%; JJ-PPC: 42%; JJ-MC: 67%) of errors misclassified an adjacent finger (Figure 3.5a, Supplementary Figure 3.4, Supplementary Figure 3.5).

Classification accuracy can depend on the neural signal quality and prediction window. To better understand how finger classification varies over dataset and classifier parameters, we quantified cross-validated accuracy across different training dataset sizes, neuron counts, and window durations (Figure 3.5b-d, Supplementary Figure 3.4, Supplementary Figure 3.5).

Cross-validated accuracy increased with more training data, reaching 80% accuracy when training on about 40 trials (2.7 minutes) for NS-PPC. Higher neuron counts provide more finger information and thus improved classification accuracy, reaching 80% accuracy at about 70 neurons for NS-PPC. These results indicate that a single electrode array in PPC provides sufficient information to control a discrete finger-press prosthetic.

Accuracy also increased when using longer window durations, reaching 80% at durations above 350ms. Longer window durations average out firing rates and thereby reduce the impact of measurement noise and behavioral variability on classification, but they directly mandate longer control delays. In some cases, it may be useful to minimize BMI control latency even at the expense of accuracy (Shanechi et al., 2017).

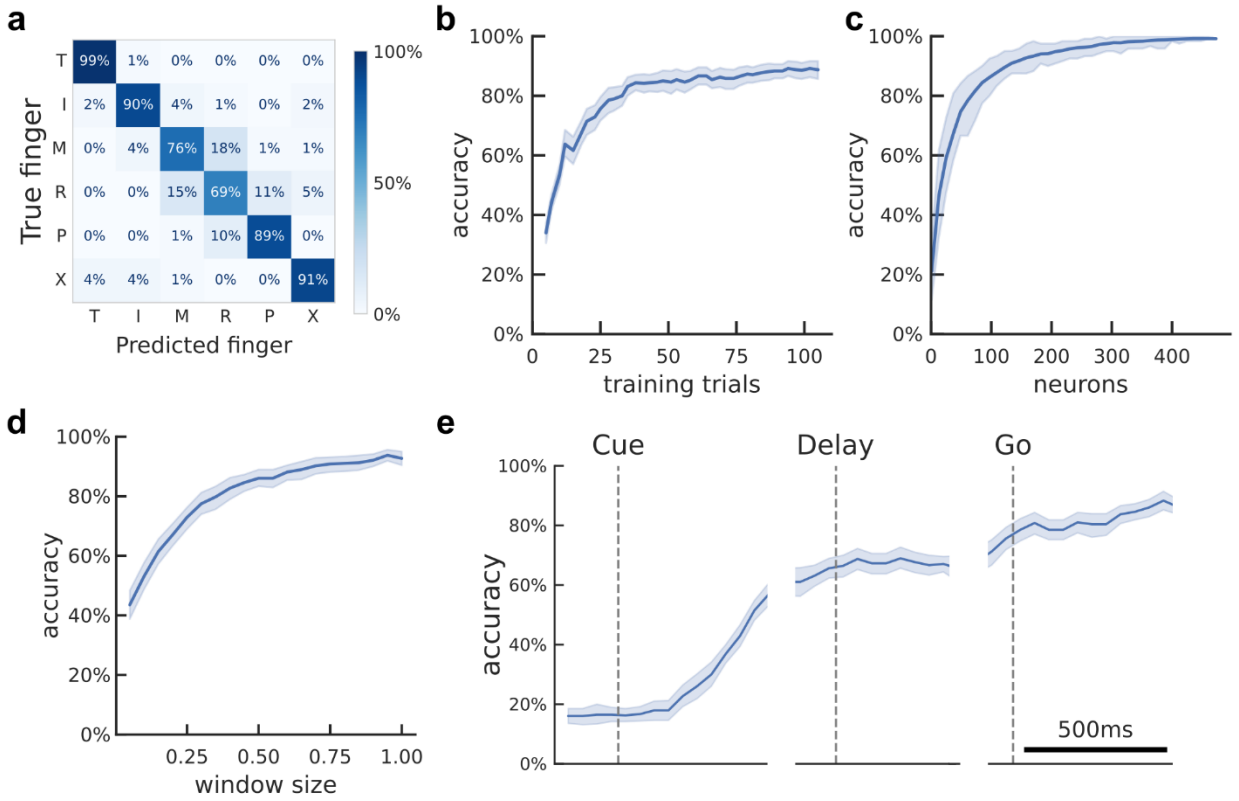

Figure 3.5. Offline classification of finger movement from population activity.

a) Cross-validated confusion matrix for classifying attempted finger movement from NS-PPC neural activity during the movement execution epoch. 86% accuracy, 480 trials over 4 sessions.

b) Learning curve showing cross-validated accuracy as a function of the training dataset size. About 40 trials (less than 7 trials per finger) are needed to achieve 80% accuracy. Shaded area indicates 95% CI over folds/sessions.

c) Neuron-dropping curve (NDC) showing cross-validated accuracy as a function of recorded neurons. Neurons were aggregated across sessions. About 70 neurons are needed to achieve 80% accuracy. Shaded area indicates 95% interval over subpopulation resamples.

d) Hyperparameter sweep showing cross-validated classification accuracy as a function of decode window size. Input features were the average firing rates in the window [200ms, 200ms + *window size*] after Go-cue. Window durations of about 350ms are necessary to achieve 80% accuracy. Shaded area indicates 95% CI over folds/sessions.

e) Cross-validated classification accuracy across the trial duration (500-ms sliding window). Shaded area indicates 95% CI over folds/sessions.

Finger movements could also be decoded from PPC during the planning period (Figure 3.5e)), although classification accuracy was lower (NS-PPC: 66%; JJ-PPC: 61%; chance: 17%) than during movement execution.

3.4.3 Brain-machine interface control of finger movements

We next mapped neural activity to finger movements to control an online finger BMI, where our participants would tap each finger and their attempted movement would be decoded. For this

section, we replicated a usage scenario where a prosthetic user could decide to move a finger and immediately execute the movement, without needing a delay period.

We started each session with an open-loop calibration task where the participant attempted to press fingers according to visual cues (Methods). Using only a short calibration period (8 repetitions per finger, totaling about 2.5 minutes), each participant was able to use a classifier to accurately control individual fingers of the BMI.

The confusion matrix for participant NS (Figure 3.6a) shows that she achieved high online control accuracies (86%; chance: 17%). These finger representations were robust across contexts and could be used in a range of environments (Guan et al., 2022b).

Participant JJ achieved even higher accuracies during BMI control (92% ± S.D. 3% over 8 sessions; chance: 17%) (Figure 3.6b). However, we note that participant JJ's BMI decoder used threshold crossings from both MC and PPC electrode arrays, thus doubling the number of electrodes compared to participant NS. While we cannot retrospectively replicate the BMI experiment with an isolated array, we can approximate the results by training the same classification algorithm on early runs, using recordings only from a single array; we can then apply this classifier to the subsequent test trials (accuracy, JJ-PPC: 83%; JJ-MC: 87%; chance: 17%; Supplementary Figure 3.6).

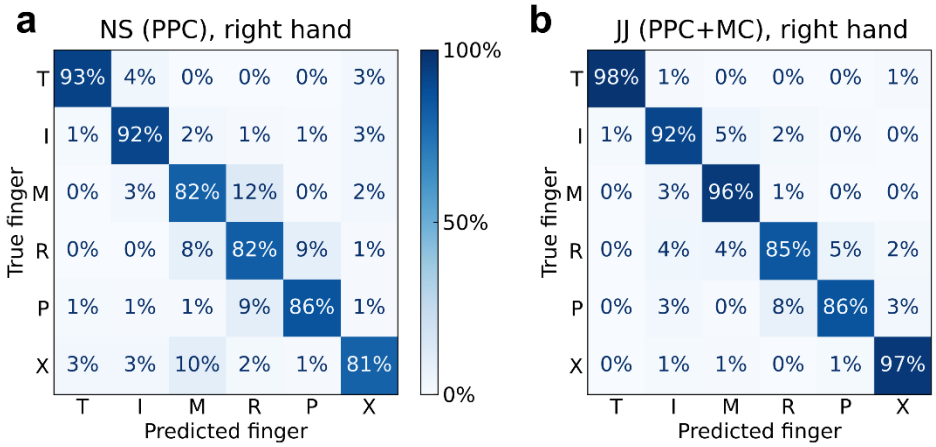

Figure 3.6. Online BMI classification of individual finger movements.

a) Confusion matrix for participant NS (PPC), right-hand finger presses. 86% accuracy ± S.D. 4% over 10 sessions, 4016 total trials. Reprinted from (Guan et al., 2022b) (CC BY-NC 4.0).

b) Confusion matrix for participant JJ (PPC+MC), right-hand finger presses. 92% accuracy ± S.D. 3% over 8 sessions, 1440 total trials.

On a few separate runs, participant JJ also performed the calibration and BMI control tasks with his left hand (ipsilateral to the implant). He achieved high accuracies (94% ± S.D. 4% over 3 sessions; chance: 17%) at a similar level to right-hand finger decoding (Supplementary Figure 3.7).

3.4.4 Classifying individual finger presses from both hands

We next investigated whether all ten finger movements could be classified from a single array. Cerebral hemispheres primarily control movement on the opposite side of the body, and we have only implanted electrode arrays in each participant's left hemisphere. However, the ability to classify

movements of both sides would reduce the number of implants necessary for bilateral BMI applications.

We examined single-neuron activity during interleaved, attempted finger presses of the contralateral (right) and ipsilateral (left) hands (Methods; participant NS: 100 trials / session for 10 sessions; participant JJ: 100 trials / session for 2 sessions). We recorded 111 neurons per session (min: 102; max: 119) from NS-PPC, 160 neurons per session (min: 159; max: 160) from JJ-PPC, and 130 neurons per session (min: 120; max: 130) from JJ-MC. Similarly to the contralateral-only results, most neurons (NS-PPC: 66%; JJ-PPC: 57%; JJ-MC: 78%) discriminated firing rates across fingers ($q < 0.05$).

We then evaluated whether these signals could be used for a neural prosthetic by classifying (offline) the attempted finger movement from the population neural activity. A linear classifier (Methods) was able to discriminate between all ten fingers (cross-validated classification accuracy, NS-PPC: 70%; JJ-PPC: 66%; JJ-MC: 75%; chance: 10%). The majority (NS-PPC: 76%; JJ-PPC: 66%; JJ-MC: 68%) of classification errors were adjacent-finger-confusion or matching-across-hand-confusion (Figure 3.7c-e).

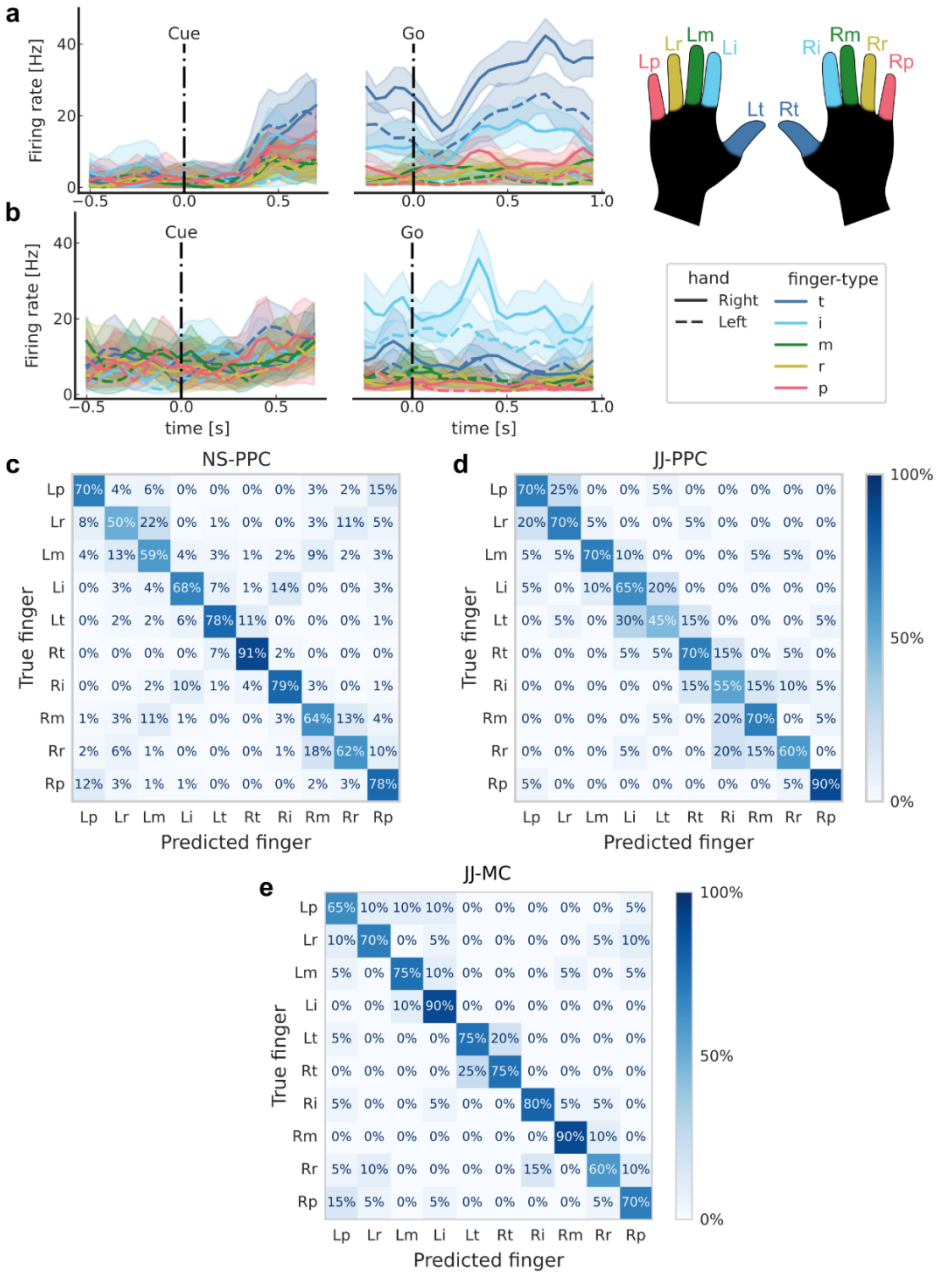

Figure 3.7. Offline classification of finger presses from both hands.

a) Mean firing rates for each finger movement for an example NS-PPC neuron, which increases its firing rate for thumb movements. Shaded areas indicate 95% confidence intervals (CI).

b) Same as (a) for a second example NS-PPC neuron, which increases it firing rate for index movements.

c) Cross-validated confusion matrix for classifying right- and left-hand finger movements from NS-PPC neural activity. 70% accuracy, 1000 trials over 10 sessions.

d) Same as (c) using recordings from JJ-PPC. 66% accuracy, 200 trials over 2 sessions.

e) Same as (c) using recordings from JJ-MC. 75% accuracy, 200 trials over 2 sessions.

3.4.5 Factorized representation of finger type and laterality

To characterize how NS-PPC simultaneously represents contralateral and ipsilateral finger movements, we calculated the cross-validated neural distances between pairs of attempted finger movements. Figure 3.8a visualizes these distances in a representational dissimilarity matrix (RDM) (Kriegeskorte and Wei, 2021) that is row- and column-indexed by finger. Visual inspection shows that neural distances are small between right/left pairs of fingers (anti-diagonal of Figure 3.8a), suggesting that movement representations are partially shared across hands. On average, matching right/left finger pairs were 1.56 distance-units (95% CI: [1.33, 1.78], Figure 3.8b) closer to each other than non-matching fingers were. Matching fingers were also represented more similarly than non-matching fingers in JJ-MC (mean difference: 4.30, 95% CI: [2.74, 5.46], Supplementary Figure 3.9b), but this result was not conclusive in JJ-PPC (mean difference: 0.27, 95% CI: [–0.17, 0.64], Supplementary Figure 3.10b).

What representational geometry allows downstream readout of all ten fingers (Figure 3.7) while sharing information across hands (Figure 3.8b)? Studies of human motor cortex (Diedrichsen et al., 2013; Bundy et al., 2018; Downey et al., 2020; Willett et al., 2020) have also found correlated representations across sides, with (Willett et al., 2020) linearly decomposing population activity into simpler factors: laterality, arm-versus-leg, and motion pattern.

Do laterality and finger-type also form a factorized code in PPC and MC? In a perfectly factorized representation (Figure 3.8c), vectors between neural representations are simply the summation of the vectors between their respective components. For example, the vector Lm->Ri can be decomposed into generic left->right and middle->index vectors. Geometrically, these generic vectors would form parallelograms between relevant groups of conditions (Figure 3.8c) (Fu et al., 2022). In other words, a factorized code would have a consistent hand subspace and a consistent finger-type subspace, although these subspaces need not be orthogonal.

We used 2-D multidimensional scaling to visualize the geometric relationship between NS-PPC finger representations (Figure 3.8d), limiting to the index, middle, and ring fingers for visual clarity. We found that inter-finger vectors were similar across hands, with the index finger relatively distinct from the middle and ring fingers, consistent with previous studies of contralateral finger movements (Ejaz et al., 2015; Guan et al., 2022b). Additionally, the left->right vector appeared identical across all matching left/right finger pairs.

Factorized coding generalizes across the axes of the simpler building blocks. Since individual left->right vectors are nearly identical to each other, linear decoders trained to differentiate left-vs-right on a subset of finger types (Lt-vs-Rt; Li-vs-Ri, Lm-vs-Rm, Lr-vs-Rr) should generalize to held-out, hypothetically equivalent vectors (Lp-vs-Rp) (Supplementary Figure 3.8). We aggregated neurons across different sessions into a pseudo-population (Methods). Consistent with the factorized coding hypothesis, cross-condition hand-decoding generalization performance (hand CCGP) was nearly perfect (accuracy using 1111 neurons: 99%, chance = 50%, $p < 0.001$, permutation test). Next, we applied cross-decoding to the finger dimension, training a classifier to discriminate between fingers of the right hand and then testing on the left hand (and vice-versa). The finger-type dimension also generalized well across hands (accuracy: 93%, chance = 20%, $p < 0.001$), and finger-type CCGP was close to the standard cross-validation accuracy (98%) evaluated using within-condition cross-validation (Figure 3.8e); this within-condition cross-validation accuracy is a best-case upper bound on CCGP. The close match between finger-type CCGP and cross-validation accuracy indicated that

the finger-type dimension robustly generalized across hands. This result demonstrates that NS-PPC finger representations can be decomposed linearly into hand and finger-type building blocks.

Comparable results held for JJ-MC recordings, with robust factorization of the neural code into hand and finger-type components (hand CCGP using 259 neurons: 86%, chance = 50%, $p < 0.001$; standard hand cross-validation accuracy: 87%) (finger-type CCGP: 75%, chance = 20%, $p < 0.001$; standard finger-type cross-validation accuracy: 89%) (Supplementary Figure 3.9). Interestingly, JJ-PPC finger representations were less factorized. While above chance ($p < 0.001$), the finger-type CCGP (36%, using 319 neurons) was much lower than the within-condition cross-validation accuracy (65%) (Supplementary Figure 3.10). Even when accounting for differences in neural population size, finger-type CCGP for JJ-PPC was lower than finger-type CCGP for NS-PPC and JJ-MC (Supplementary Figure 3.11).

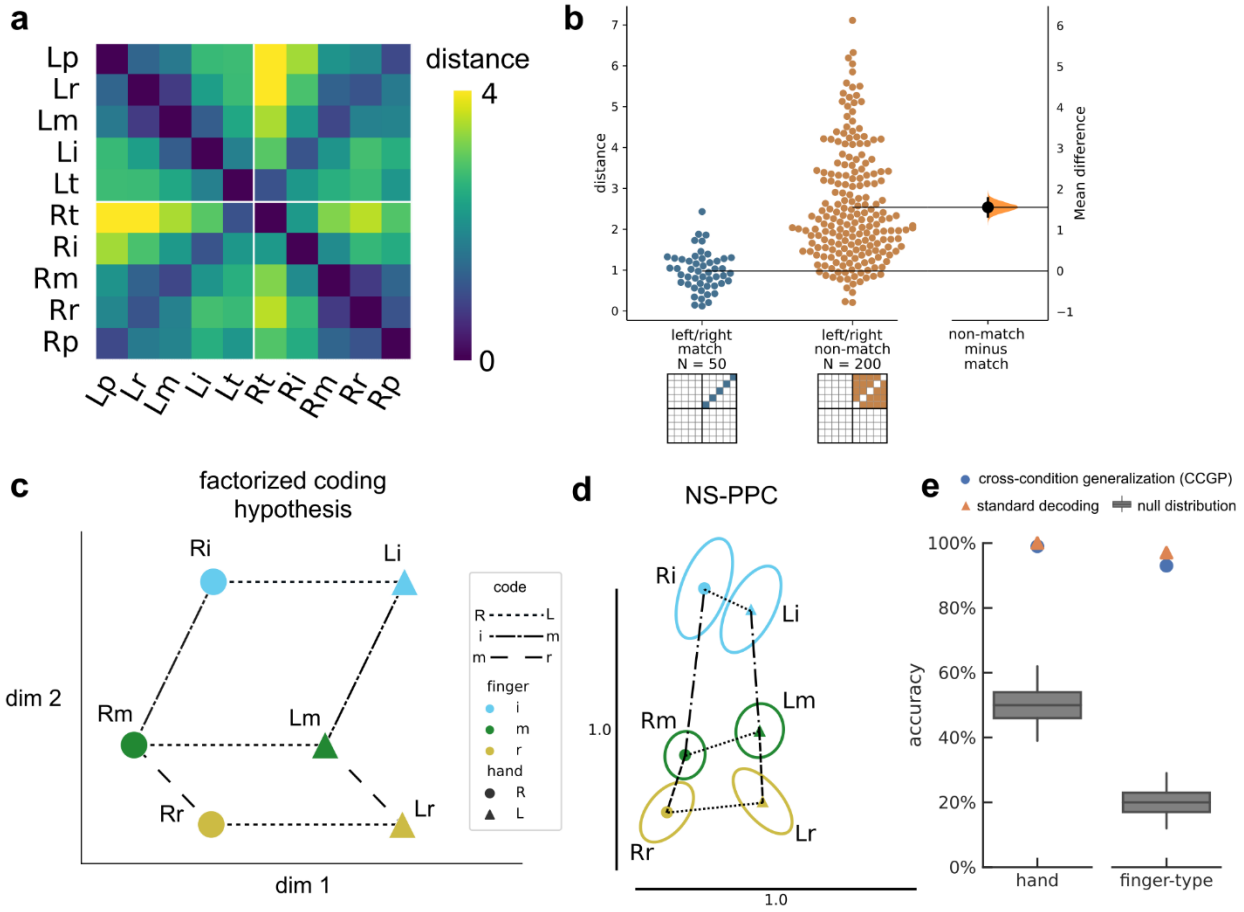

Figure 3.8. Representational geometry of contralateral and ipsilateral finger movements.

a) Cross-validated squared Mahalanobis distances between NS-PPC activity patterns during the contralateral/ipsilateral finger press task. Distances were averaged over the 10 sessions.

b) Non-matching (different finger-type, different hand) finger pairs have larger distances than matching (same finger-type, different hand) finger pairs. Each circle is one element of the dissimilarity matrix of an individual session, aggregated across 10 sessions.

c) Example schematic of perfect factorization along hand and finger-type components. Line styles indicate groups of parallel, identical vectors. A factorized code generalizes linearly across each component axis. For example, the Rm population activity can be constructed from the summation: Li + left->right + index->middle. For visual clarity, figure only shows three finger-types (index, middle, ring).

d) Representational geometry of finger movements corresponding to NS-PPC distances (a), visualized in 2-D using multidimensional scaling (MDS). We used Generalized Procrustes analysis (with scaling) to align across 10 sessions. Ellipses show standard error (S.E.) across sessions. Scale bars shown. Vectors with matching line-styles match each other, suggesting that the neural code is factorized.

e) Linear decoders generalized (Supplementary Figure 3.8) across finger-type to classify hand (left) and across hand to classify finger-type (right) ($p < 0.001$, permutation test), indicating that movement representations were factorized across finger-type and hand dimensions.

3.5 Discussion

Human dexterity is characterized by our ability to quickly reach-and-grasp, as well as our ability to move individual fingers volitionally beyond basic grasp templates (Yan et al., 2020). Individual finger movements are generally considered to be the domain of the motor cortex (MC) hand knob, while the posterior parietal cortex (PPC) complements via higher-level computations, such as transforming object shape to grip type (Schaffelhofer and Scherberger, 2016). This perception is supported by a wide range of evidence (Sobinov and Bensmaia, 2021); for example, fMRI studies find topographic finger activation maps in MC (Allison et al., 2000; Ejaz et al., 2015) but not in PPC (Ariani et al., 2022). Despite the lack of coarse finger topography in PPC, here we found that neurons in two grasp-related regions of PPC were discriminative for attempted finger movements. Population tuning was robust enough for human participants to control finger BMIs in a variety of applications. These results demonstrate that detailed information about finger movements is more distributed than is commonly thought.

Our study adds to a growing number of finger BMI demonstrations. Previously, (Hotson et al., 2016) demonstrated the first online neural decoding of all-five individual finger movements in human participants, using a high-density ECoG grid over the sensorimotor cortex. Like our study, (Jorge et al., 2020) implanted intracortical arrays in the motor cortex of a tetraplegic participant and decoded attempted finger movements, achieving an offline accuracy of 67%. Recently, (Nason et al., 2021; Willsey et al., 2022) achieved high-performance continuous control of flexion and extension of two finger groups. Our results contribute to prior studies by showing that simultaneous PPC+MC recordings can improve online finger decoding accuracies (Figure 3.6). Considering that PPC and MC usually fulfill different functions for able-bodied sensorimotor control (Sobinov and Bensmaia, 2021), an interesting future direction will be to understand to what degree PPC and MC complement each other across more diverse BMI control paradigms.

Algorithmic advances may further improve finger decoding performance. For example, hierarchical classifiers might be useful for classifying finger direction and finger movement (Hotson et al., 2016). Additionally, with larger data quantities or with data augmentation strategies, time-varying and nonlinear classifiers like recurrent neural networks can improve neural decoding (Inoue et al., 2018; Gruenwald et al., 2019; Willett et al., 2021; Willsey et al., 2022). Performance improvements may also come from decoding non-traditional variables, such as handwriting (Willett et al., 2021) or goals (Aflalo et al., 2015). State-machine control (common in other assistive technologies like myoelectric prostheses (Fougner et al., 2012) or Dwell) and AI-assisted hybrid control (Katyal et al., 2014; Downey et al., 2016) may further improve BMI usability. In combination with somatosensory intracortical microstimulation (ICMS) to generate fingertip sensations (Flesher et al., 2016; Fifer et al., 2021), such methods could enable a functional hand prosthetic.

After demonstrating BMI control of the contralateral fingers, we studied representations of ipsilateral finger movements. We found that a linear classifier could discriminate between movements of all ten fingers (Figure 3.7). Given that descending corticospinal tracts primarily cross to control the contralateral side, it was interesting to find that ipsilateral decoding was relatively robust. On some sessions, ipsilateral decoding accuracies were even comparable to contralateral decoding (Supplementary Figure 3.7). An important follow-up would be to understand how individual finger representations mix to construct multi-finger movements, both within and across hands. fMRI studies of sensorimotor cortex suggest that same-hand movements would be organized

by their natural usage patterns (Ejaz et al., 2015), while both-hand movements would exclusively represent the contralateral fingers (Diedrichsen et al., 2013). An open question is whether these patterns also extend to single-neuron recordings and to PPC.

Even as the ten finger movements were discriminable, activity patterns for NS-PPC and JJ-MC were similar across corresponding finger pairs on opposite hands (Figure 3.8a-b). Our results match other studies that have also found shared-yet-separable hand representations in macaque anterior intraparietal area (AIP) (Michaels and Scherberger, 2018) and human motor cortex (Diedrichsen et al., 2013; Willett et al., 2020). This pattern of cross-condition generalization has previously been described as partially mixed selectivity (Zhang et al., 2017), abstract or factorized representations (Bernardi et al., 2020), or compositional coding (Willett et al., 2020; Aflalo et al., 2022). Here, the NS-PPC and JJ-MC finger codes could be factorized into finger-type and laterality subspaces (Figure 3.8d-e), resembling the partial compositionality described by (Willett et al., 2020) for arm and leg movements. Compositional and factorized coding have been speculated to play a number of different computational functions, from skill transfer to general cognition (Zhang et al., 2017; Downey et al., 2020; Frankland and Greene, 2020; Willett et al., 2020; Aflalo et al., 2022). For neuroprosthetic applications, factorized coding simplifies decoder calibration. Because neural coding generalizes across conditions, decoders can train on only the underlying factors, rather than every combination.

Surprisingly, JJ-PPC population activity was not factorized to the same extent as NS-PPC and JJ-MC. The difference between JJ-PPC and NS-PPC results might stem from neuroanatomical variability (Scheperjans et al., 2008; Gallivan and Culham, 2015) or differences in implant location. The NS-PPC implant was located at the junction of the postcentral and intraparietal sulci (PC-IP), an area involved in grasping and fine finger movements (Binkofski et al., 1998; Gallivan and Culham, 2015; Klaes et al., 2015). PC-IP receives inputs from neighboring somatosensory cortex (Scheperjans et al., 2008; Rolls et al., 2022), suggesting that it may facilitate state estimation of the hand (Shadmehr and Krakauer, 2008; Tunik et al., 2008; Guan et al., 2022b). We could not implant the JJ-PPC recording array in the center of the PPC grasping area, functionally localized near PC-IP (Supplementary Figure 3.1), because blood vessels obstructed the cortical surface. Thus, we implanted the JJ-PPC array in the superior parietal lobule (SPL), medial and posterior compared to the NS-PPC implant. Medial and posterior areas of PPC tend to receive stronger visual inputs (Scheperjans et al., 2008; Wang et al., 2015; Rolls et al., 2022) and are more involved in reaching than grasping (Mars et al., 2011), so the recorded JJ-PPC population could be more involved in calculating visuomotor transforms (Buneo and Andersen, 2006; Rolls et al., 2022) for visually guided reaching (Scheperjans et al., 2008; Mars et al., 2011). It is possible that the difference in implant location also contributed to differences in contralateral finger tuning between NS-PPC (Figure 3.4) and JJ-PPC (Supplementary Figure 3.2). However, it is difficult to precisely compare implant locations, because the anatomical location of individual functional areas can vary widely between participants (Scheperjans et al., 2008; Gallivan and Culham, 2015). Future comparisons may benefit from multi-modal preoperative neuroimaging to map implant locations onto standard parcellations (Glasser et al., 2016).

The posterior parietal cortex (PPC) has long been known to be involved in the reaching and grasping of objects, but less is known about its contribution to individual finger movements. Here, two tetraplegic participants controlled individual fingers through BMIs recording from the posterior

parietal cortex and motor cortex (MC). Ipsilateral finger coding was strong in all three recorded neural populations, and two of the populations exhibited factorized coding that enabled decoders to simultaneously generalize across and discriminate between hands. Our results demonstrate that PPC and MC can provide complementary control signals for assistive neuroprosthetics.

3.6 Acknowledgments

NS and JJ made this research possible through their participation. Tyson Aflalo, Kelly Kadlec, and Jorge Gámez de Leon were close collaborators on this project, which is part of a long-term collaboration with Emily Rosario, Ausaf Bari, and Nader Pouratian. Spencer Kellis assisted with the robot hand demo.

3.7 Supplementary Material

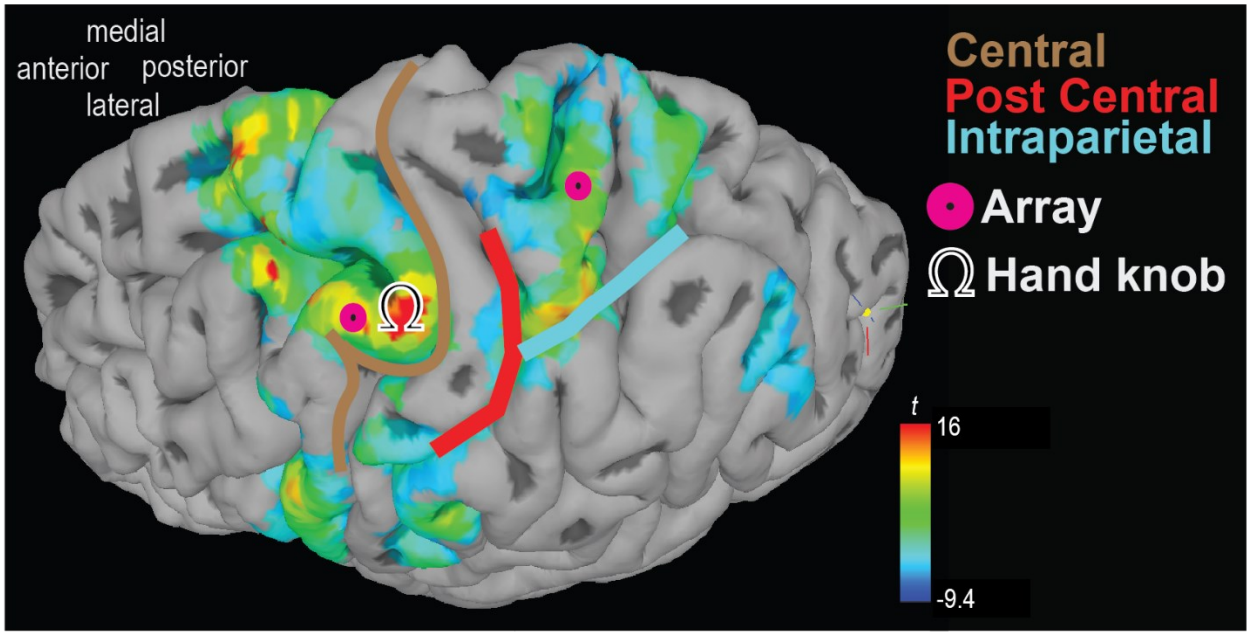

Supplementary Figure 3.1. Electrode array implant locations in participant JJ.
Microelectrode array locations overlaid on participant JJ's left cerebral hemisphere. Color scale indicates fMRI activation for grasp>look/point (task described in Figure S1b of (Aflalo et al., 2020)). One array (denoted JJ-PPC) was implanted in the superior parietal lobule (SPL) of the left PPC. Another array (denoted JJ-MC) was implanted near the hand knob of the left motor cortex (MC).

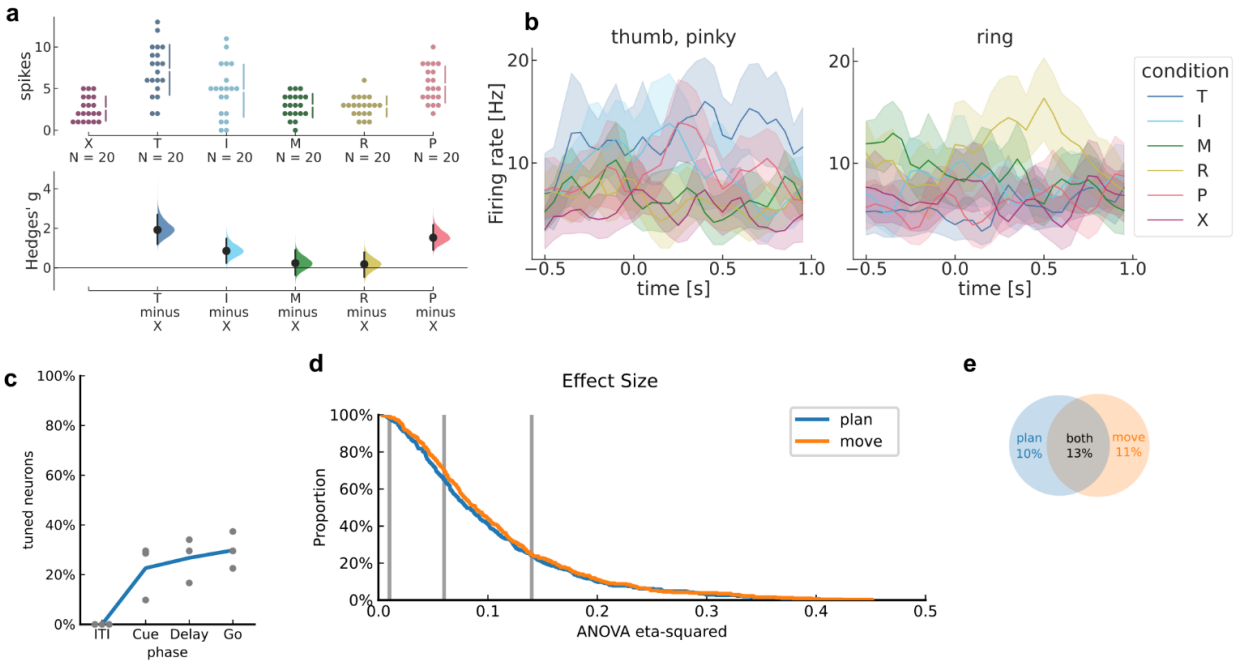

Supplementary Figure 3.2. PPC single neurons discriminate between attempted finger movements (JJ-PPC).
Similar to Figure 3.4 for JJ-PPC recordings.

a) Single-trial firing rates for an example JJ-PPC neuron during attempted movements of different fingers. (top) Markers correspond to the firing rate during each trial. Gapped vertical lines to the right of markers indicate ± S.D., and each gap indicates the mean firing rate. (bottom) Firing rates during thumb (T), index (I), and pinky (P) presses were higher than the No-go (X) baseline. Vertical bars indicate bootstrap 95% confidence intervals (CI) of the effect size versus No-go baseline. Half-violin plots indicate bootstrap distributions.

b) Mean smoothed firing rates for each finger movement for two example JJ-PPC neurons, which respectively modulated for thumb/pinky movements (left) and ring movements (right). Shaded areas indicate 95% CI.

c) Percentage of JJ-PPC neurons that discriminated between finger movements in each analysis window ($q < 0.05$, FDR-corrected for 308 neurons). Line (blue) indicates mean across sessions. Markers (gray) indicate individual sessions.

d) Complementary empirical cumulative distribution function (cECDF) visualizing the proportion of JJ-PPC neurons with ANOVA effect sizes (η^2) above the corresponding x-axis value. Line colors indicate analysis epoch. Vertical lines (gray) indicate Cohen's thresholds (Cohen, 1988) for small (η^2=0.01), medium (η^2=0.06), and large (η^2=0.14) effect sizes.

e) Overlap of JJ-PPC neurons that modulated significantly ($q < 0.05$) with large effect sizes ($\eta^2 > 0.14$) during movement preparation (plan) and movement execution (move).

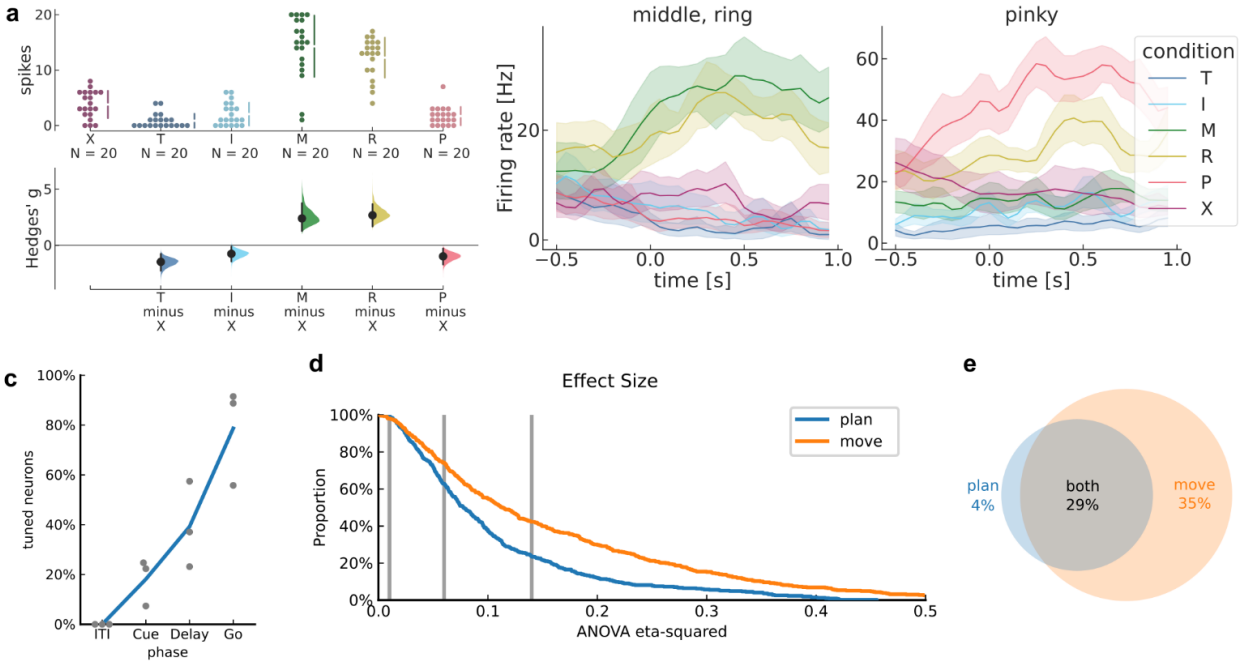

Supplementary Figure 3.3. MC single neurons discriminate between attempted finger movements (JJ-MC).
Similar to Figure 3.4 for JJ-MC recordings.

a) Single-trial firing rates for an example JJ-MC neuron during attempted movements of different fingers. (top) Markers correspond to the firing rate during each trial. Gapped vertical lines to the right of markers indicate ± S.D., and each gap indicates the mean firing rate. (bottom) Firing rates during middle (M) and ring (R) presses were higher than the No-go (X) baseline. Vertical bars indicate bootstrap 95% confidence intervals (CI) of the effect size versus No-go baseline. Half-violin plots indicate bootstrap distributions.

b) Mean smoothed firing rates for each finger movement for two example JJ-MC neurons, which respectively modulated for middle/ring movements (left) and pinky movements (right). Shaded areas indicate 95% CI.

c) Percentage of JJ-MC neurons that discriminated between finger movements in each analysis window ($q < 0.05$, FDR-corrected for 278 neurons). Line (blue) indicates mean across sessions. Markers (gray) indicate individual sessions.

d) Complementary empirical cumulative distribution function (cECDF) visualizing the proportion of JJ-MC neurons with ANOVA effect sizes (η^2) above the corresponding x-axis value. Line colors indicate analysis epoch. Vertical lines (gray) indicate Cohen's thresholds (Cohen, 1988) for small (η^2=0.01), medium (η^2=0.06), and large (η^2=0.14) effect sizes.

e) Overlap of JJ-MC neurons that modulated significantly ($q < 0.05$) with large effect sizes ($\eta^2 > 0.14$) during movement preparation (plan) and movement execution (move).

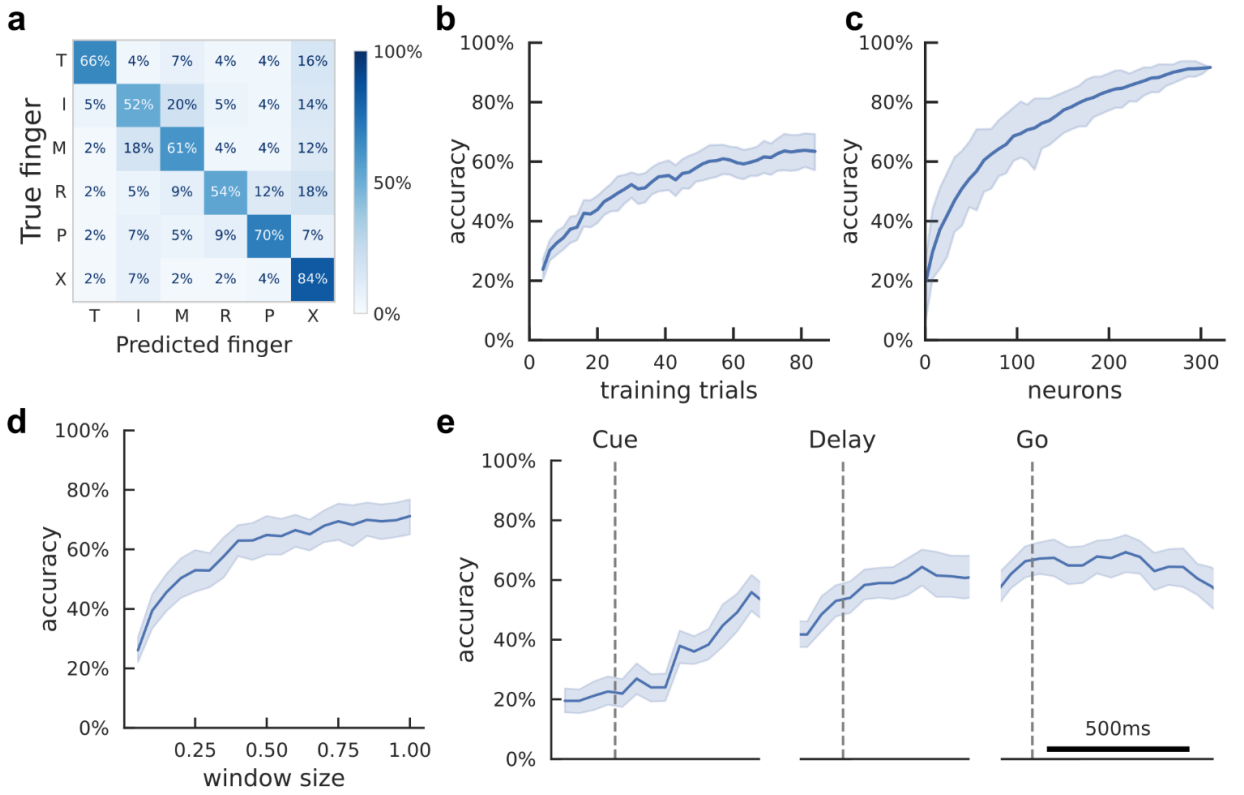

Supplementary Figure 3.4. Offline classification of finger movement from PPC population activity (JJ-PPC).

Similar to Figure 3.5 for JJ-PPC population recordings.

a) Cross-validated confusion matrix for classifying attempted finger movement from JJ-PPC neural activity during the movement execution epoch. 64% accuracy, 336 trials over 3 sessions.

b) Learning curve showing cross-validated accuracy as a function of the training dataset size. Shaded area indicates 95% CI over folds/sessions.

c) Neuron-dropping curve (NDC) showing cross-validated accuracy as a function of recorded population size. Shaded area indicates 95% interval over subpopulation resamples.

d) Hyperparameter sweep showing cross-validated classification accuracy as a function of decode window size. Input features were the average firing rates in the window [200ms, 200ms + window size] after Go-cue. Shaded area indicates 95% CI over folds/sessions.

e) Cross-validated classification accuracy across the trial duration (500-ms sliding window). Shaded area indicates 95% CI over folds/sessions.

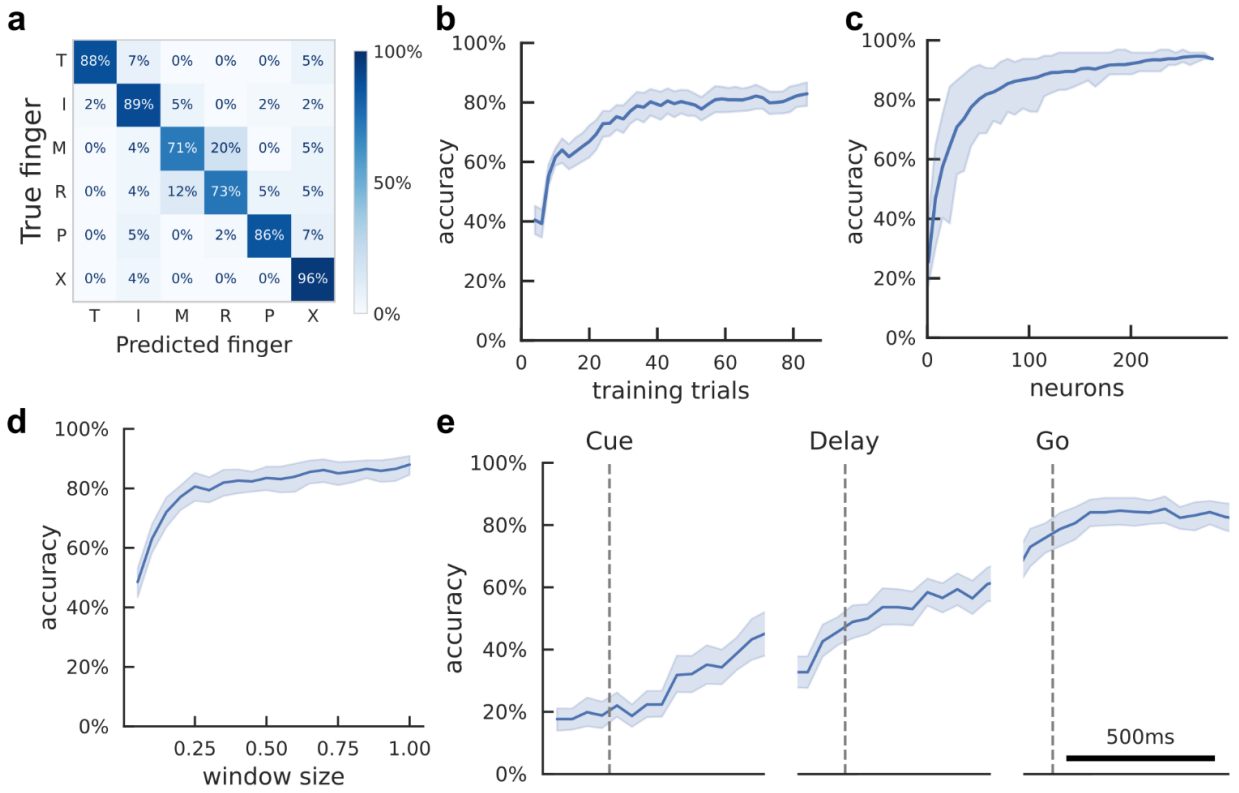

Supplementary Figure 3.5. Offline classification of finger movement from MC population activity (JJ-MC).

Similar to Figure 3.5 for JJ-MC population recordings.

a) Cross-validated confusion matrix for classifying attempted finger movement from JJ-MC neural activity during the movement execution epoch. 84% accuracy, 336 trials over 3 sessions.

b) Learning curve showing cross-validated accuracy as a function of the training dataset size. Shaded area indicates 95% CI over folds/sessions.

c) Neuron-dropping curve (NDC) showing cross-validated accuracy as a function of recorded population size. Shaded area indicates 95% interval over subpopulation resamples.

d) Hyperparameter sweep showing cross-validated classification accuracy as a function of decode window size. Input features were the average firing rates in the window [200ms, 200ms + window size] after Go-cue. Shaded area indicates 95% CI over folds/sessions.

e) Cross-validated classification accuracy across the trial duration (500-ms sliding window). Shaded area indicates 95% CI over folds/sessions.

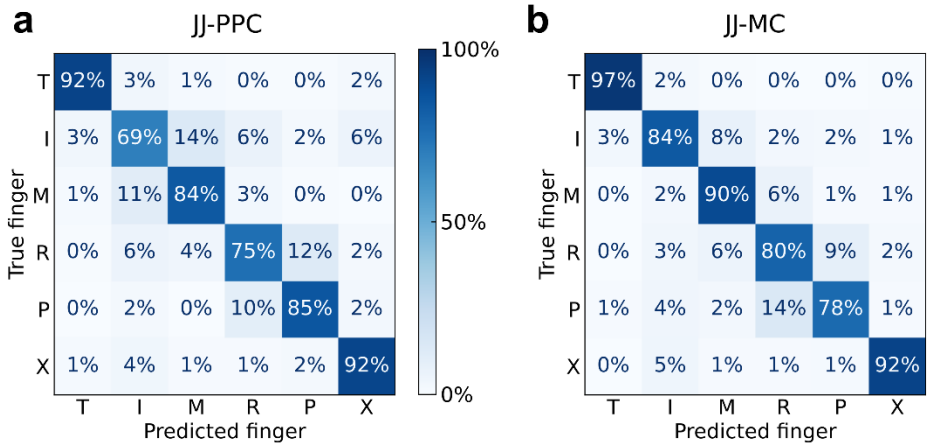

Supplementary Figure 3.6. Retrospective BMI accuracy when decoding from a single electrode array.

a) Offline approximation of single-array BMI accuracy. We trained the linear classifier on earlier run-blocks [0, 1, ..., M – 1] and evaluated on run-block M, repeating for all run-blocks in each session. 83% accuracy ± S.D. 7% (chance 17%), 1440 trials over 8 sessions.

b) Same as (a) using JJ-MC population activity. 87% accuracy ± S.D. 8% (chance 17%), 1440 trials over 8 sessions.

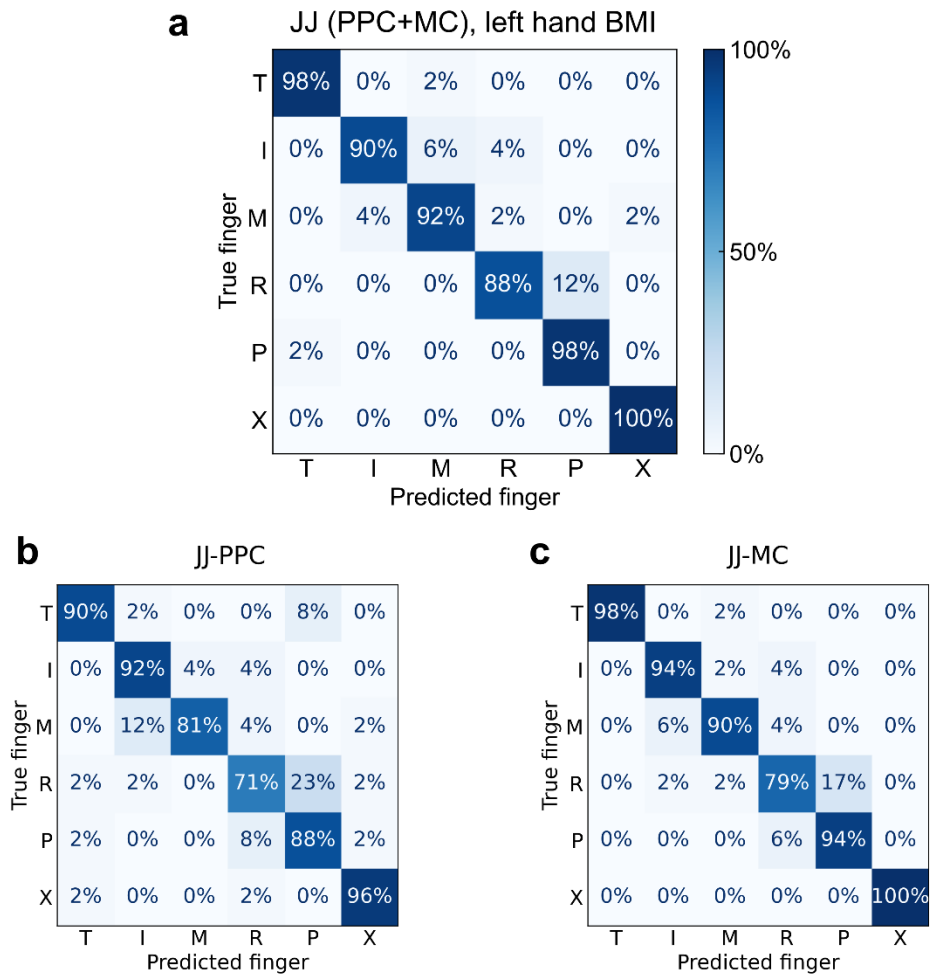

Supplementary Figure 3.7. Left-hand BMI classification of individual finger movements.

a) Confusion matrix for participant JJ (PPC+MC), left-hand finger presses. 94% ± S.D. 4% over 3 sessions (chance = 17%), 288 total trials.

b) Offline approximation of single-array BMI accuracy for left-hand finger presses. We trained the linear classifier on earlier run-blocks [0, 1, ..., M – 1] and evaluated on run-block M, repeating for all run-blocks in each session. 86% accuracy ± S.D. 3%.

c) Same as (b) using JJ-MC population activity. 92% accuracy ± S.D. 5%.

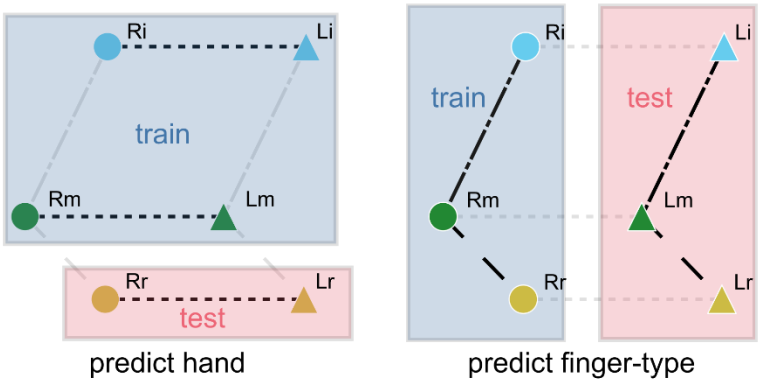

Supplementary Figure 3.8. Cross-condition generalization paradigm to assess the factorized coding hypothesis.

Factorized coding enables a linear decoder to generalize to unseen test conditions. (left) A left-vs-right-hand decoder was trained on 4 pairs of fingers, then evaluated on the held-out finger-type. Cross-condition generalization accuracies (CCGP) were averaged over all folds of hold-one-finger-type-out. (right) A 5-class finger-type decoder was trained on the right hand and evaluated on the left hand (and vice versa). (both) Plot only shows markers for the right and left index, middle, and ring fingers, but the actual procedure included all ten fingers.

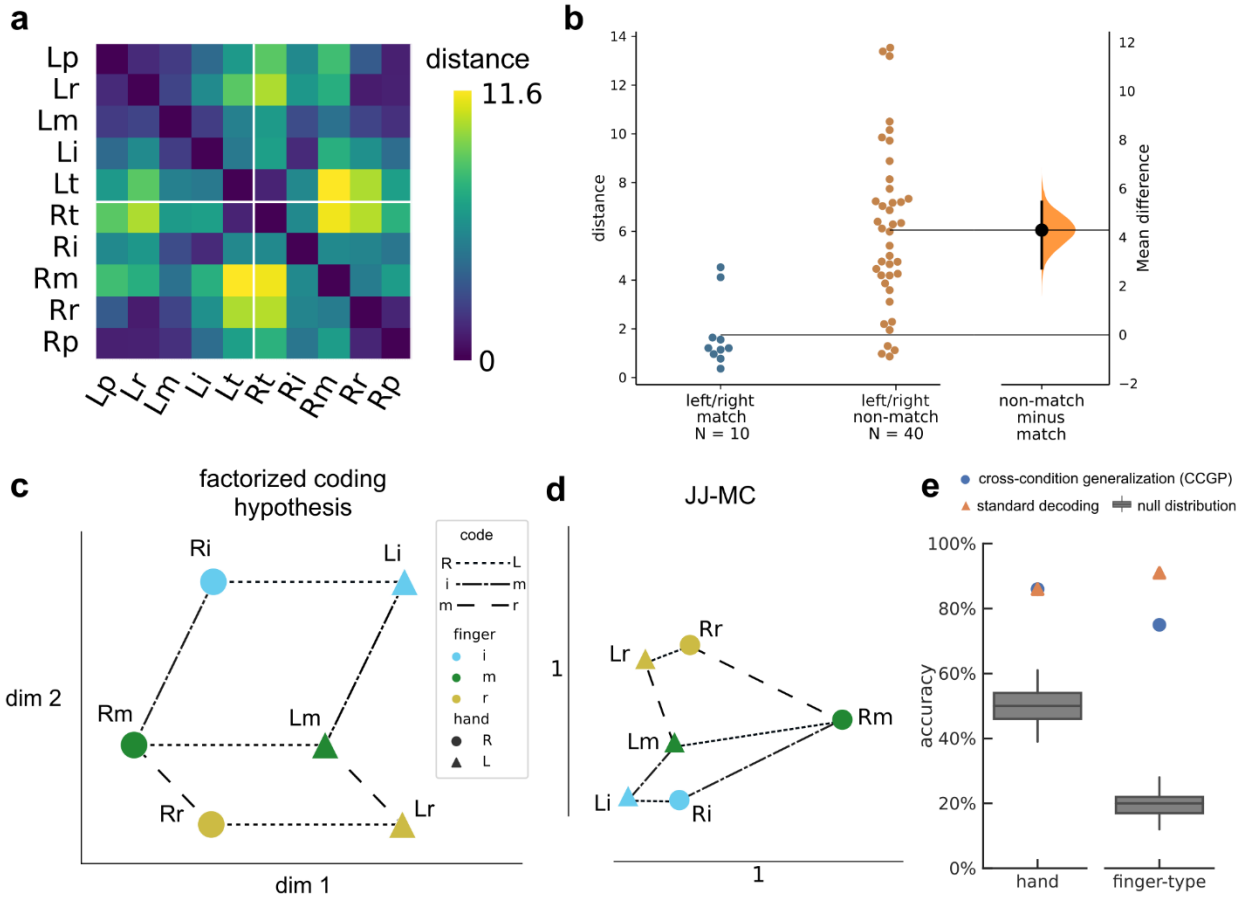

Supplementary Figure 3.9. Representational geometry of contralateral and ipsilateral finger movements (JJ-MC)

Similar to Figure 3.8 for JJ-MC population recordings.

a) Cross-validated squared Mahalanobis distances between JJ-MC activity patterns during the contralateral/ipsilateral finger press task. Distances were averaged over the 2 sessions.

b) Non-matching finger pairs have larger distances than matching finger pairs. Each circle is one pairwise distance, aggregated across 2 sessions.

c) Example schematic of perfect factorization along hand and finger-type components. Line styles indicate groups of parallel, identical vectors. A factorized code generalizes linearly across each component axis. For example, the Rm population activity can be constructed from the summation: Li + left->right + index->middle. For visual clarity, only three finger-types (index, middle, ring) are shown.

d) Representational geometry of finger movements corresponding to JJ-MC distances (a), visualized in 2-D using multidimensional scaling (MDS). We used Generalized Procrustes analysis (with scaling) to align across 2 sessions. Markers indicate mean across sessions. Scale bars shown.

e) Linear decoders generalized (Supplementary Figure 3.8) across finger-type to classify hand (left) and across hand to classify finger-type (right) ($p < 0.001$, permutation test), indicating that movement representations were factorized across finger-type and hand dimensions.

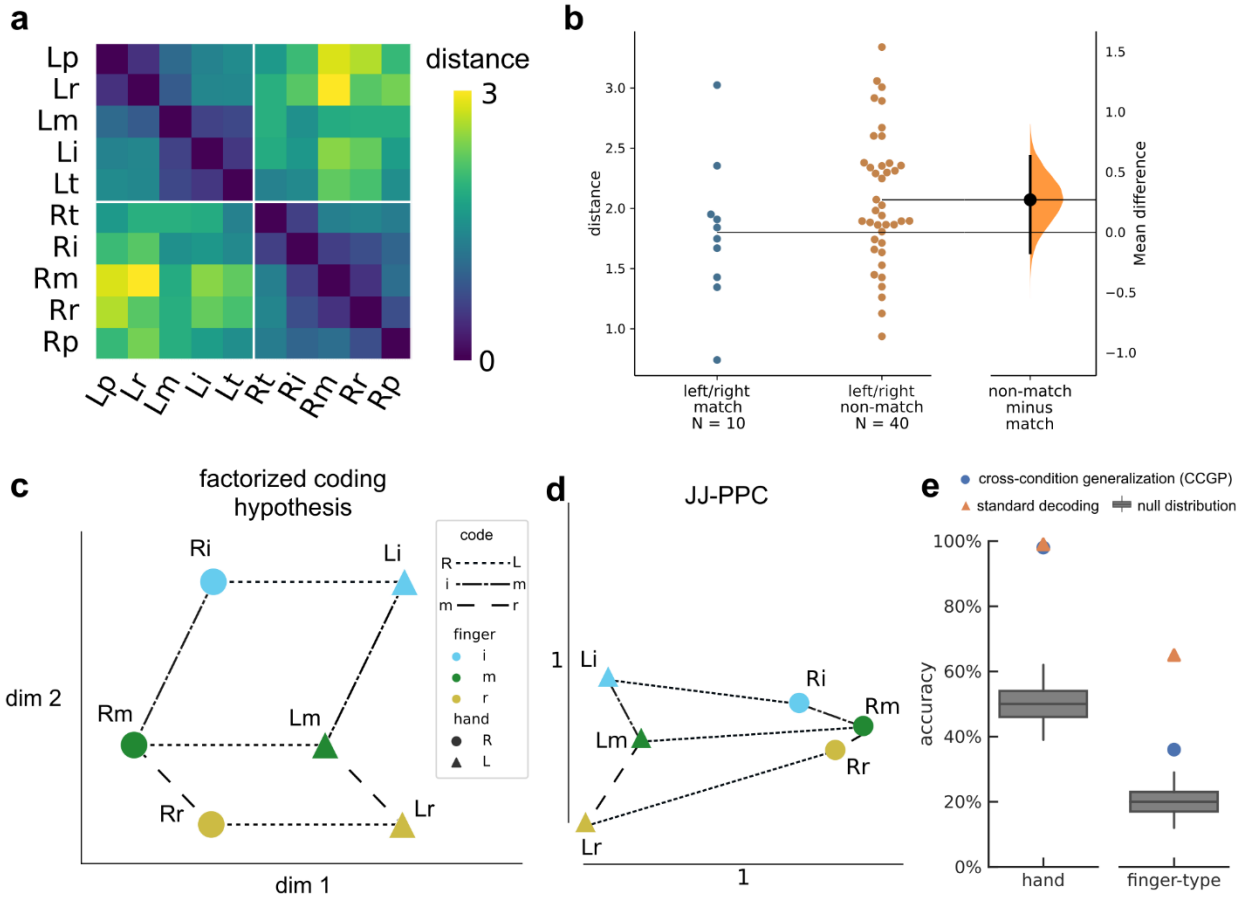

Supplementary Figure 3.10. Representational geometry of contralateral and ipsilateral finger movements (JJ-PPC)

Similar to Figure 3.8 for JJ-PPC population recordings.

a) Cross-validated squared Mahalanobis distances between JJ-PPC activity patterns during the contralateral/ipsilateral finger press task. Distances were averaged over the 2 sessions.

b) Comparison of distances between matching finger pairs and non-matching finger pairs. Each circle is one pairwise distance, aggregated across 2 sessions.

c) Example schematic of perfect factorization into hand and finger-type components. Line styles indicate groups of parallel, identical vectors. A factorized code generalizes linearly across each component axis. For example, the Rm population activity can be constructed from the summation: Li + left->right + index->middle. For visual clarity, only three finger-types (index, middle, ring) are shown.

d) Representational geometry of finger movements corresponding to JJ-PPC distances (a), visualized in 2-D using multidimensional scaling (MDS). We used Generalized Procrustes analysis (with scaling) to align across 2 sessions. Markers indicate mean across sessions. Scale bars shown.

e) (left) Linear decoders generalized (Supplementary Figure 3.8) across finger-type to classify hand (left; $p < 0.001$, permutation test). (right) Finger-type cross-condition generalization performance (CCGP; blue circle) was lower than standard decoding accuracy (orange triangle).

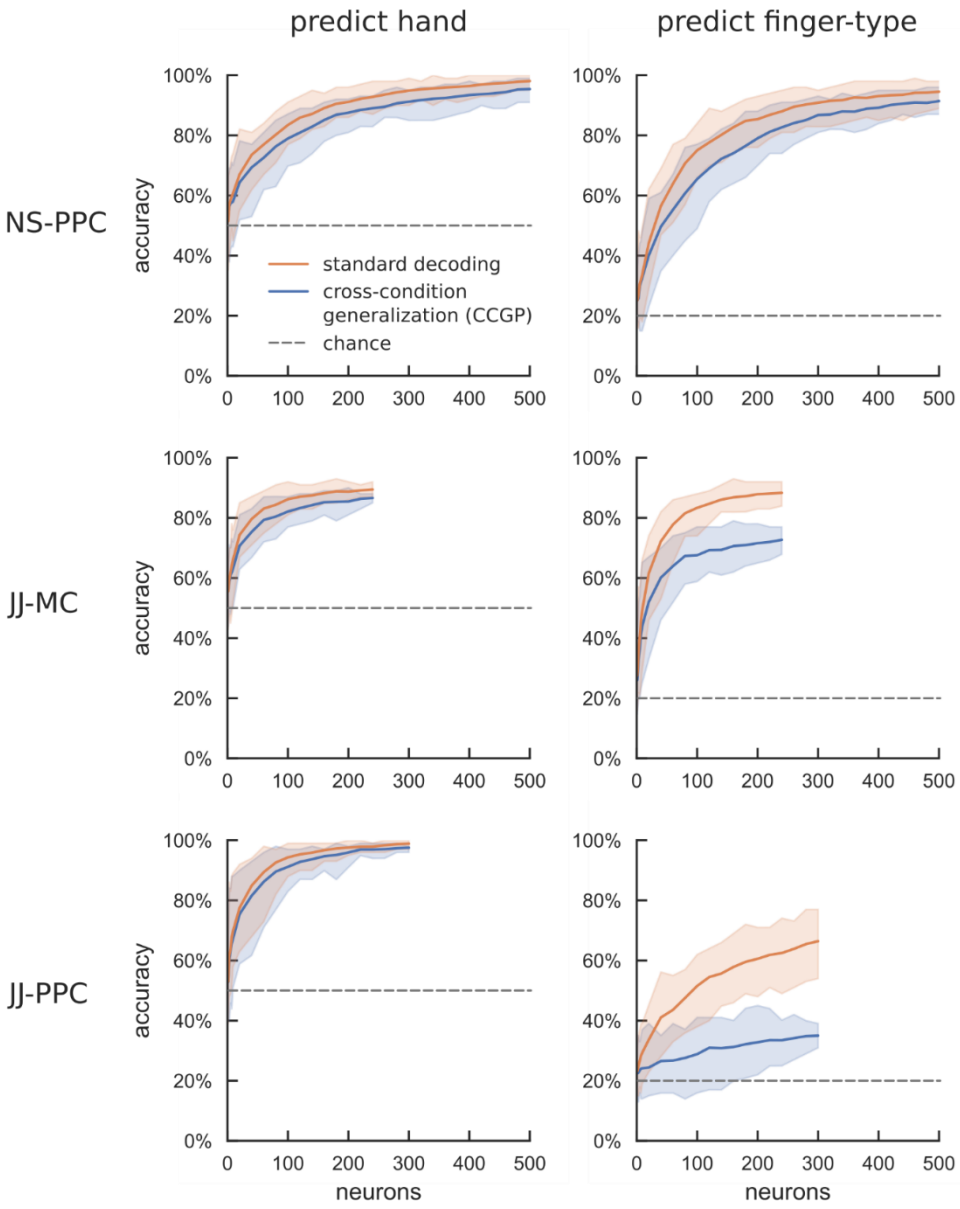

Supplementary Figure 3.11. Neuron-dropping curve for cross-condition generalization performance (CCGP).

Neuron dropping curves show generalization accuracy as a function of neural population size. Panel columns correspond to the variable predicted (left: hand; right: finger-type). Panel rows correspond to the recorded neural population. Shaded area indicates 95% interval over subpopulation resamples. Hand CCGP matched standard decoding accuracy in all recorded neural populations. Finger-type CCGP matched standard decoding accuracy for NS-PPC and JJ-MC, but finger-type decoders trained on JJ-PPC activity did not generalize well across hands (bottom right panel). 1111 NS-PPC neurons were recorded across 10 sessions, but we truncated the dropping curve at 500 neurons to match scales across participants.

		Phase					
Task	**Participant**	**Pre-Cue**	**Cue**	**Delay**	**Go**	**ITI**	**Feedback**
Alternating Cues	NS	1 sec	0.75 sec	1.25 - 2 sec	1 sec	2 sec	
Alternating Cues	JJ	0.5 sec	1.5 sec	0.5 - 1 sec	1 sec	0.5 - 1 sec	
Reaction time, randomized location	NS and JJ				1.5 sec		1.5 sec
Ten-finger	NS		1.5 or 1 sec	1 or 1–1.5 sec	1 sec	2 or 1.5 sec	
Ten-finger	JJ		1 or 1.5 sec	1–1.5 or 0.75–1 sec	1 or 2 sec	1.5 or 2 sec	

Supplementary Table 3.1. Phase durations for each task.

Table of phase durations for the different tasks and participants. Blank cells indicate that the task did not include that phase. Ranges indicate a uniform-random distribution per trial.

Participant	Task	Number of sessions	First session (days after implant)	Last session (days after implant)
NS	Alternating Cues	4	909	948
	Reaction time, randomized location	10	1476	1518
	Ten-finger	10	351	636
JJ	Alternating Cues	3	1046	1179
	Reaction time, randomized location	8	107	249
	Ten-finger	2	78	389

Supplementary Table 3.2. Date ranges for each task.

Dates of first and last session for each task.
Although the Alternating Cues data was presented first in the Results section, this data was collected from participant JJ later than the reaction-time data. The drop in neural yield between these dates affected classification performance.

4 Neural population dynamics during brain-computer interface control

4.1 Summary

The motor cortex (MC) is often described as an autonomous dynamical system during movement execution. In an autonomous dynamical system, flexible movement generation depends on reconfiguring the initial conditions, which then unwind along known dynamics. An open question is whether these dynamics govern MC activity during brain-computer interface (BCI) control. We investigated MC activity during BCI cursor movements of multiple durations, ranging from hundreds of milliseconds to sustained over seconds. These durations were chosen to cover the range of movement durations necessary to control modern BCIs under varying precision levels. Movements of different durations shared their MC initial condition with other movements in the same direction. However, sustained movements resulted in sustained MC activity, effectively pausing the neural population dynamics until each movement goal was reached. The difference in MC population trajectories can be attributed to external inputs. Our results highlight the role of inputs to MC during BCI control and potentially hint that MC likely integrates inputs even during able-bodied movement.

4.2 Introduction

The motor cortex (MC) is plays a central role in volitional movement, yet its precise mechanism is still debated (Omrani et al., 2017). Inspired by feature coding in the visual cortex, MC studies from the 1980s to early 2000s focused on representational modeling (RM), identifying movement parameters that correlate directly with neural activity. Studies discovered a wide range of represented parameters, including movement direction, speed, force, muscle activity, and posture (Evarts, 1968; Georgopoulos et al., 1986, 1992; Kakei et al., 1999; Moran and Schwartz, 1999; Paninski et al., 2004; Aflalo and Graziano, 2006). Multiple movement parameters were often represented simultaneously, however, and these representations shifted across task contexts (Aflalo and Graziano, 2007; Scott, 2008; Omrani et al., 2017) or even within a single movement (Churchland and Shenoy, 2007), challenging the notion of a literal movement parameter representation. Researchers began to voice that this parameter search was misleading (Fetz, 1992; Scott, 2008; Omrani et al., 2017). Perhaps MC neurons did not represent literal movement parameters, and a different framework was necessary.

A now-prominent framework emerged to replace representational modeling: the autonomous dynamical system hypothesis (aDSH). The aDSH states that the motor cortex comprises a pattern generator, where preparatory activity sets the initial condition and movement execution activity unfolds along predictable dynamics (Churchland et al., 2012; Shenoy et al., 2013; Pandarinath et al., 2015, 2018a, 2018b; Sussillo et al., 2015; Vyas et al., 2020). The aDSH has been demonstrated most comprehensively with able-bodied non-human primate subjects performing a prepared-reach task (Churchland et al., 2010, 2012; Kaufman et al., 2014; Elsayed et al., 2016). In this task, the initial preparatory state comprises a sufficient statistic to predict quasi-oscillatory MC activity during reach

execution (Pandarinath et al., 2018b). Recurrent neural network models indicate that local recurrence could implement MC's brief oscillations (Sussillo et al., 2015; Pandarinath et al., 2018b; Russo et al., 2018; O'Shea et al., 2022; Saxena et al., 2022), which provide a basis set for generating multiphasic muscle activity (Churchland et al., 2012; Sussillo et al., 2015).

Mathematically, a dynamical system can be described by a function f mapping the system state x and external inputs u to the instantaneous change in state $\frac{dx}{dt}$:

$$\frac{dx}{dt} = f\big(x(t), u(t)\big)$$

Equation 4.1

where t indicates time. Frequently (Shenoy et al., 2013; Sauerbrei et al., 2020), the system state is defined as the MC firing rate vector $\boldsymbol{r}$, and f is constrained to be an additive linear function h that models local recurrence. The input $\boldsymbol{u}$ can include external stimuli and the firing rates of other brain areas. In this simplification, Equation 4.1 can be written as:

$$\frac{d\boldsymbol{r}}{dt} = h\big(\boldsymbol{r}(t)\big) + \boldsymbol{u}(t).$$

Equation 4.2

The autonomous dynamical systems hypothesis posits that the system (MC) is self-contained during execution of prepared movements. That is, $\boldsymbol{u}$ is negligible during movement execution, further simplifying Equation 4.2 into:

$$\frac{d\boldsymbol{r}}{dt} = A\boldsymbol{r}(t) + b$$

Equation 4.3

where A is the dynamics matrix and b is an offset vector.

The autonomous dynamical systems hypothesis explained phenomena that had puzzled the RM framework. For example, neurons appear to change representational tuning with time, because they generate a temporal basis rather than directly driving the output (Shenoy et al., 2013; Pandarinath et al., 2018a). And apparent modulation by multiple movement parameters was not literal parameter representation, but rather a basis set for downstream muscle read-out.

Three related claims follow from the autonomous dynamical systems hypothesis. First, because the local MC dynamics h are stable (Gallego et al., 2020) and the external inputs u are hypothesized to be negligible, generating different neural trajectories $\boldsymbol{r}(t)$ is solely determined by specifying different initial conditions $\boldsymbol{r}(0)$ (Churchland et al., 2012; Pandarinath et al., 2018b; Vyas et al., 2020). Second, these dynamics cause movement; that is, neural perturbations disrupt movement if and only if the perturbation alters the task dynamics subspace (O'Shea et al., 2022). Third, because external inputs like sensory feedback are hypothesized to be negligible, errors cannot be easily detected and then corrected, so pattern generation must be robust to noise. Noise-robust autonomous dynamical systems exhibit low tangling (described in MC by (Russo et al., 2018)) (i.e.,

smooth flow fields) and low divergence (described in supplementary motor area, but notably not in MC, by (Russo et al., 2020)).

An important open question is whether these same autonomous dynamical principles govern MC activity during brain-computer interface (BCI) control. BCIs aim to restore movement to people with motor disabilities by decoding motor intent directly from neural activity (Hochberg et al., 2006, 2012; Collinger et al., 2013c; Aflalo et al., 2015; Gilja et al., 2015; Wodlinger et al., 2015; Bouton et al., 2016; Ajiboye et al., 2017). BCI cursor control has long been considered analogous to able-bodied reaching (Serruya et al., 2002; Taylor et al., 2002; Hochberg et al., 2006; Hwang et al., 2013; Golub et al., 2016; Inoue et al., 2018). Given the success of aDSH in explaining MC activity during able-bodied reaching, this analogy suggests that aDSH-based modeling could improve human BCI control of assistive devices (Kao et al., 2015; Pandarinath et al., 2018a). Such modeling has even extended successfully to movements beyond arm reaching (Hall et al., 2014; Stavisky et al., 2019; Kalidindi et al., 2021).

The applicability of the autonomous dynamical systems hypothesis is not a given, however. The aDSH has received various critiques, ranging from other explanations for the observed data's structure (Lebedev et al., 2019; Kalidindi et al., 2021) to aDSH's lack of generalization to dexterous movements (Sauerbrei et al., 2020; Suresh et al., 2020) or stopping movements (Russo et al., 2020). From the perspective of applying aDSH to BCI control, a core limitation is the assumption that feedback is negligible. Compared to the arm movements usually modeled by aDSH, current BCIs read out from a miniscule number of neurons, so BCI control is slower and less precise (Shanechi, 2016; Willett et al., 2017a) and prone to nonstationarities (Jarosiewicz et al., 2015). As a result, high-performance BCI control benefits from rapid real-time feedback (Gilja et al., 2012; Shanechi et al., 2016, 2017; Willett et al., 2018, 2019). During able-bodied movement, motor cortex reflects proprioceptive signals that are missing during BCI control (Stavisky et al., 2018). Taken together, behavioral dynamics and sensory inputs differ substantially between BCI control and able-bodied arm reaching.

Dynamical systems modeling promises to improve neural decoding performance (Kao et al., 2015; Pandarinath et al., 2018a; Gallego et al., 2020; Karpowicz et al., 2022). Given the difference in behavioral dynamics between able-bodied reaching and BCI control, an open question is how well the aDSH applies to BCI movements across different applications. In order to probe the relative contributions of autonomous dynamics, initial conditions, sensory inputs, and non-sensory inputs to MC activity, we adapted variants of the common BCI cursor tasks that dissociated the various components of a dynamical system. When the BCI participant attempted ballistic reaches analogous to previous aDSH studies, MC activity reproduced the previously described rotational dynamics. When the BCI participant sustained cursor movement for longer durations, the initial conditions were similar, yet the neural trajectories paused along that of ballistic movements. This divergence in neural trajectories would have required inputs from outside MC, inconsistent with the autonomous dynamical systems hypothesis. These inputs to MC were present even in the absence of sensory feedback, indicating that MC receives inputs from other brain areas during relatively simple behavior. Although autonomous dynamics may exist during able-bodied movement, MC is not constrained by such dynamics when a task requires otherwise.

4.3 Results

4.3.1 Intracortical brain-computer interface (BCI) cursor control

We recorded neural activity from microelectrode arrays implanted in participant JJ's hand knob of left motor cortex (MC) and posterior parietal cortex (PPC) while he completed different brain-computer interface (BCI) 2-D cursor tasks. To calibrate a BCI decoder, participant JJ observed a computer-controlled cursor perform the center-out-and-back task with 8 targets. Simultaneously, participant JJ attempted to move his right thumb as though he was controlling the cursor via a thumb joystick. Because participant JJ previously suffered a C4-C5 spinal cord injury, he cannot feel or move his fingers. Instead, participant JJ attempted to move his thumb as though he was not paralyzed. Using data from this calibration task, we trained a decoder to map predicted cursor velocity from electrode threshold crossing rates. Participant JJ then performed the same center-out-and-back task under BCI control, usually with partial computer assistance (Methods, weighted average assistance). He used the same attempted movement strategy (thumb joystick) during online BCI control; we use the terms "BCI control" and "movement" interchangeably here. We used the online BCI data to recalibrate the BCI decoder, because this recalibration procedure improves subsequent control (Jarosiewicz et al., 2013).

4.3.2 Ballistic and sustained BCI movements

The autonomous dynamical systems hypothesis (aDSH) is typically studied in non-human primates performing ballistic arm reaches, with movement durations on the order of 400ms (Churchland et al., 2012; Pandarinath et al., 2018b), but analogous BCI movements can take several seconds for comparably precise reaches (Willett et al., 2017a). BCI-useful models of MC activity should apply to movements of both timescales. To replicate both ballistic and sustained reaches, participant JJ performed the center-out BCI task under two decoder gain parameters. For sustained reaches, we limited the decoder gain to 25% or 30% of its normal value. For ballistic reaches, decoder gain was either set at its normal value or 300% of its normal value. BCI control is imprecise at high decoder gains (Willett et al., 2017a), but we wanted to investigate reaches analogous to well-practiced, able-bodied reaching, where corrections are small. Therefore, we partially assisted ballistic cursor control (Methods, error rail assistance), at a small enough level that cursor movement was primarily driven by neural activity. Additionally, participant JJ was not required to hold the cursor at the target, but was rather instructed to relax when the target hit. Sustained and ballistic reaches were grouped into respective trial blocks and block-interleaved.

Under both gain parameters, Participant JJ acquired the targets consistently (Figure 4.1; Supplementary Figure 4.1). As designed, ballistic (BCI) movement trials took a roughly similar amount of time as previous non-human primate studies (acquisition time, session 2: 0.45s ± SD 0.19s; Figure 4.1d). As designed, sustained movement trials were substantially longer (mean acquisition time, session 2: 2.34s; 95% CI of mean difference sustained-vs-ballistic: [1.77, 2.05]s). These patterns were consistent across sessions (Supplementary Figure 4.1).

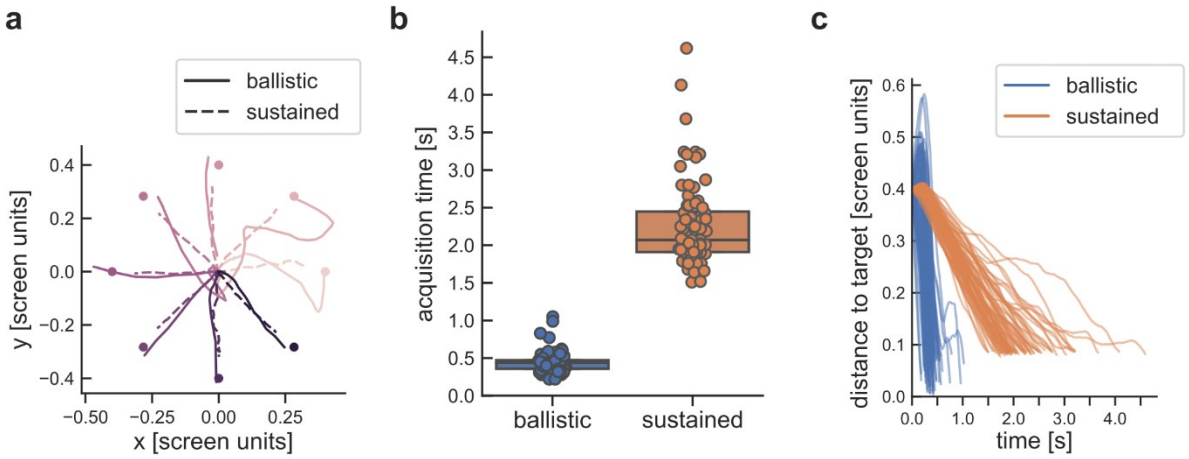

Figure 4.1. Ballistic and sustained brain-computer interface (BCI) cursor movements.
(**a**) Example single-trial cursor trajectories during BCI center-out task for ballistic and sustained movements.
(**b**) Distance to the target, as a function of time. Each line corresponds to a trial from session 2. Additional sessions visualized in Supplementary Figure 4.1.
(**c**) Time to reach target. Each marker corresponds to a trial from session 2. Box plot lines indicate lower quartile, median, and upper quartile, respectively.

4.3.3 Sustained single-neuron and population activity in motor cortex (MC) during sustained BCI movements is shared with ballistic movement encoding

We visualized single-neuron activity across sustained and ballistic trials (Figure 4.2a-c). Because our focus was to better understand the autonomous dynamical systems hypothesis (aDSH), which describes MC, here, we focus on analyzing MC recordings. During ballistic movements, many neurons exhibited phasic firing rate modulation, usually rising with movement onset and falling with target acquisition. During sustained movements, many neurons exhibited the same onset firing rate increase (Figure 4.2a) but instead sustained their firing rate throughout the entire movement (Figure 4.2b-c).

Next, we visualized population activity using principal component analysis (PCA) (Figure 4.2d). Similarly to a previous study (Kaufman et al., 2016), the largest-variance principal component (PC) was largely condition-invariant and reflected movement onset timing. Interestingly, the second- and third-largest-variance PCs corresponded directly to movement direction, regardless of the decoder gain parameter. In other words, population activity during sustained and ballistic movements to the same target took the same initial neural trajectory before diverging. The same projection matrix was used for both conditions, and thus similar responses suggest that ballistic and sustained movements share a common neural substrate.

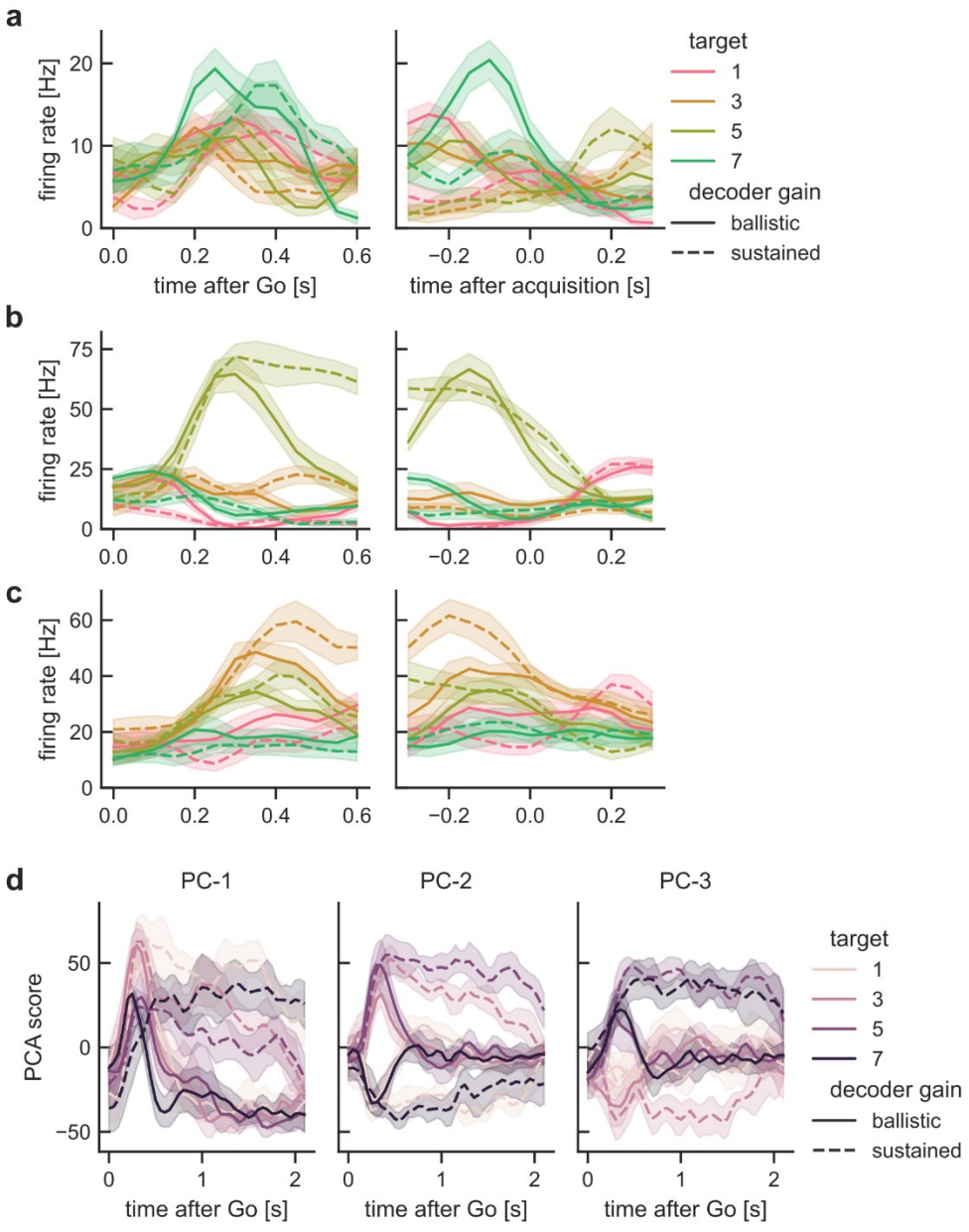

Figure 4.2. Neural responses in motor cortex (MC) during BCI cursor movements.
(**a**) Mean firing rate of an example neuron, aligned to Go (left panel) and target acquisition (right panel). Example neuron increased firing rate during movement onset. Most neurons appeared to modulate during movement onset, sustain firing rates during sustained movements, or some combination of onset and sustained preferred direction. 8 targets were used, but only 4 target conditions are shown.
(**b**) Mean firing rate of an example neuron, which activated during movements to target 5 and sustained firing for sustained movements.
(**c**) Mean firing rate of an example neuron, which activated during movements to target 3 and sustained firing for sustained movements.
(**d**) Principal component analysis (PCA) of MC population activity.

4.3.4 Comparing ballistic and sustained BCI movements reveals input-driven dynamics

During movement execution, the initial aDSH study described (quasi-)oscillatory dynamics, akin to a pendulum (Pandarinath et al., 2018a) or spring-mass system (Figure 4.3a). In this hypothetical limit of the system not receiving external inputs, the initial condition and dynamics should fully determine the neural trajectory. They used jPCA, a rotated variant of PCA, to uncover quasi-oscillatory dynamics in the neural activity (Churchland et al., 2012). Briefly, jPCA is a rotated version of PCA first reduces the recording dimensionality to the first $k = 6$ PCs. Within this subspace, a new orthonormal basis of k jPCs is calculated, such that the top two jPCs maximize the rotational component. This is mathematically equivalent to fitting the constrained dynamical system:

$$\dot{\boldsymbol{X}}(t, c) = M_{skew}\boldsymbol{X}(t, c)$$

Equation 4.4

where $\boldsymbol{X}(t, c)$ is the k-dimensional PCA reduction of the population firing rate vectors at time t and condition c. M_{skew} is a skew-symmetric matrix, whose eigenvectors correspond to the jPCs.A corollary to oscillatory dynamics is that $\left\|\dot{\boldsymbol{X}}(t, c)\right\|_2$ the neural speed should be constant throughout the movement duration (Figure 4.3a). We applied jPCA to MC activity during ballistic BCI movements (Figure 4.3b).

Consistent with ballistic arm reach studies (Churchland et al., 2012), jPCA revealed clear rotational dynamics in the top jPC plane. We compared the jPCA fit to null distribution with the same neural/temporal covariance structure. We generated the covariance-constrained null distribution using tensor maximum entropy (TME) (Elsayed and Cunningham, 2017) and applied to jPCA to the samples. The jPCA fit was significantly better on the true data than the null distribution ($p<0.001$). Consistent with these results, the cross-validated (Methods) neural population speed $\left\|\dot{\boldsymbol{X}}(t, c)\right\|_2$ was large across the duration of the movement (Figure 4.3c).

Next, we applied the neural speed and jPCA analyses to MC activity during sustained BCI movements (Figure 4.3c). Cross-validated neural speed high was during movement onset but returned to baseline levels (close to the ITI baseline) indicating that the neural activity is maintaining a constant stationary representation of intent while sustaining the BCI movement. In the jPCA visualization, this sustained activity appears as a "pause" in the rotational trajectory.

Finally, in Figure 4.3d, we compare directional tuning properties between three windows of time; one from the initial dynamic period (250–450ms after target presentation) and two from the sustained movement period chosen to equate duration and spacing between the three windows. In MC, the within- and across- time window comparisons show different tuning profiles between the early and sustained windows, but consistent coding in the sustained windows. Thus, MC sustained motor intent appears to consist of an initial dynamic phase and a subsequent sustained phase until the target is reached.

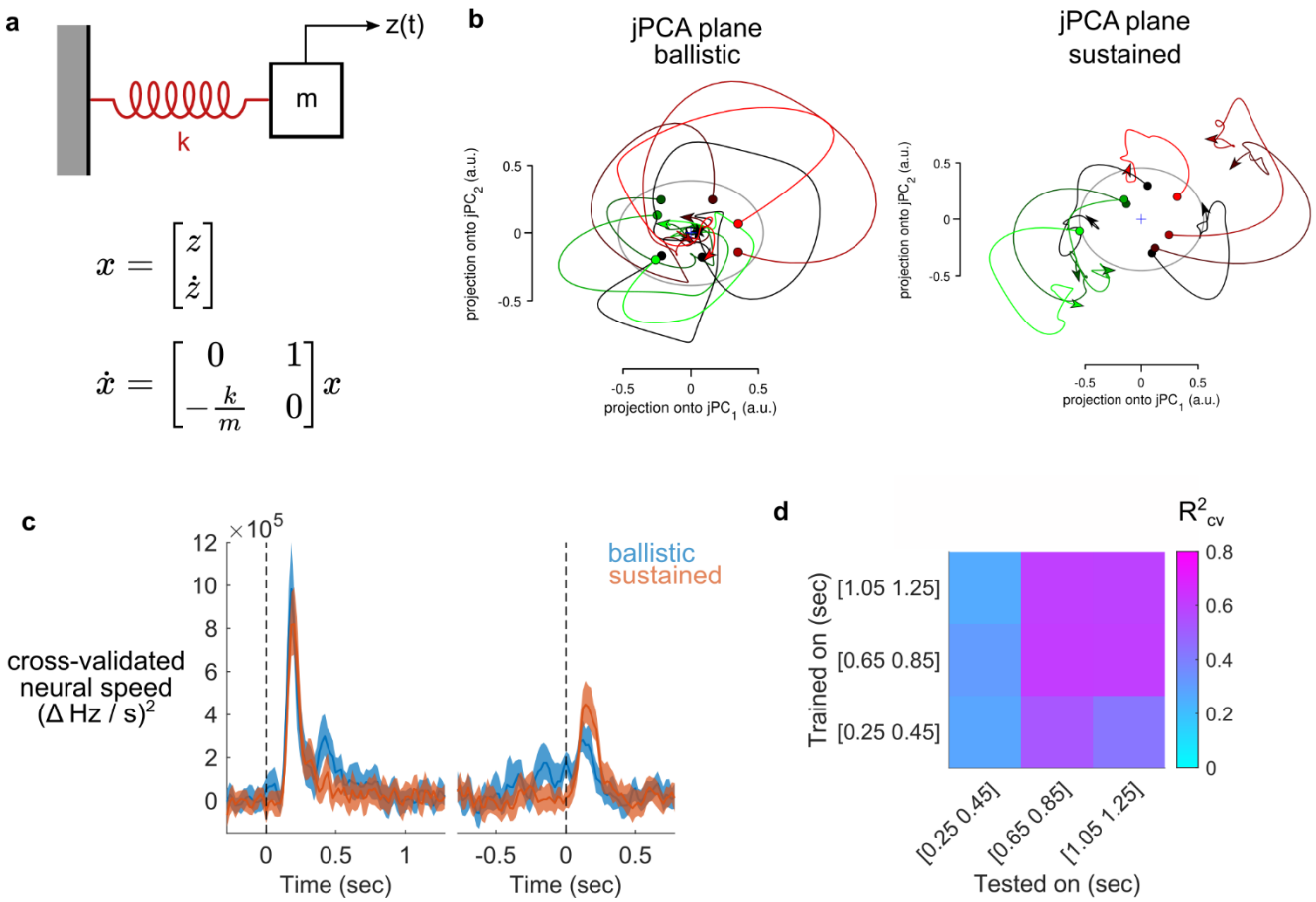

Figure 4.3. MC population dynamics during ballistic and sustained BCI movements.
(**a**) A simple example of an autonomous dynamical system: a spring-mass system.
(**b**) jPCA shows rotational dynamics begins similarly for ballistic and sustained movements, but freezes in place during sustained movement intent.
(**c**) Cross-validated neural speed is high at movement initiation and offset. During sustained movement intent, neural speed is slow.
(**d**) Within- and across-time regression shows changing directional coding dependent on temporal context.

4.4 Discussion

4.4.1 Rigid dynamics versus flexible control of motor cortex activity

The motor cortex's precise mechanisms have been debated for decades. Recent studies have highlighted how the motor cortex (MC) can be modeled as an autonomous pattern generator during arm movement (Churchland et al., 2012; Shenoy et al., 2013; Pandarinath et al., 2015, 2018a, 2018b; Sussillo et al., 2015; Vyas et al., 2020). Given the similarities between able-bodied movements and brain-computer interface (BCI) control (Hochberg et al., 2006; Hwang et al., 2013; Golub et al., 2016; Guan et al., 2022b), an open question was whether autonomous dynamics would also dictate MC activity during BCI control. BCI control provides a unique opportunity to study MC activity, and the results have important implications for decoder design.

We found that participant JJ could produce MC activity during BCI control beyond the constraints of the autonomous dynamical systems hypothesis. During able-bodied-like ballistic movements, MC activity reproduced previously described oscillatory dynamics (Figure 4.3) (Churchland et al., 2012). When necessary for sustained BCI movements, participant JJ could easily sustain MC activity (Figure 4.2) rather than strictly following autonomous dynamics. Interestingly, the MC activity was shared between the onsets of both the ballistic and sustained movements, despite the aDSH hypothesis that different initial conditions would lead to different movements (Shenoy et al., 2013; Vyas et al., 2020). The sustained MC activity effectively paused the dynamics until the target was reached, at which point the offset dynamics continued (Figure 4.3). We summarize these results in Figure 4.4.

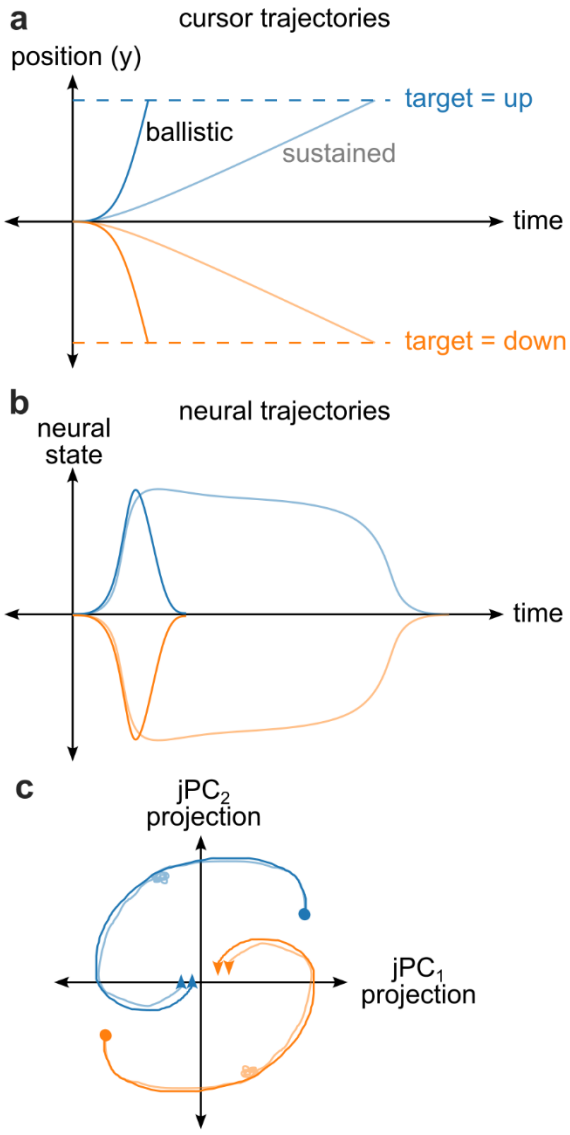

Figure 4.4. Summary diagram
(**a**) Example cursor trajectories for ballistic (opaque lines) and sustained (translucent lines) movements to targets in the up (blue) and down (orange) direction.
(**b**) Initial neural trajectories are shared between ballistic (opaque lines) and sustained (translucent lines) BCI movements to each target (blue and orange), but sustained movements generate sustained neural activity.
(**c**) jPCA visualization of neural trajectories to two targets (blue and orange). When compared to ballistic movements (opaque lines), population activity during sustained movements (translucent lines) pauses the dynamics (visualized as squiggles halfway along trajectory).

Our results indicate that an autonomous dynamical system is too strict a model for the wide temporal scales of possible BCI movements. Similar results and interpretations have been reported anecdotally

(Stavisky, 2016), although we did not find any other preprints or published reports that directly studied this.

These results should not be construed to mean that MC has absolutely no constraints on neural activity. A series of studies have examined how the covariance structure of MC during natural movement (also known as a "neural manifold") constrains one's ability to generate arbitrary activity (Sadtler et al., 2014; Golub et al., 2018; Oby et al., 2019). Neural activity patterns within this natural covariance structure are much easier to generate than outside it. However, our results indicate that there are not constraints on the dynamical trajectories to reach the different points on this manifold.

Our results raises the question that autonomous neural dynamics during reaching are partially a function of the behavioral task and its timescales, rather than an innate property of motor cortex. What may seem like intrinsic dynamics may appear more like behavioral dynamics at different timescales. As shown here, dynamics learned from one behavioral timescale may not apply to similar behaviors performed at shorter or longer timescales. This was also one of the original pitfalls of standard representational modeling (RM); RM found neurons tuned to as many variables as were tested, because oftentimes variables are highly correlated. Similarly, without joint behavioral-neural dynamics modeling (Sani et al., 2021) or without higher-dimensional tasks (Gao et al., 2017), it can be difficult to disentangle intrinsic neural dynamics from behavioral dynamics.

4.4.2 Switching decoders for brain-computer interfaces

Most previous demonstrations of neural prosthetics have used stationary algorithms like linear regression to decode movement velocity (Collinger et al., 2013c). Our results both explain the success of stationary algorithms, like linear regression, as well as outline paths forward for better decoding. Due to the difficulty of controlling modern BCIs, BCI trajectory control often spans multiple seconds, in which the sustained neural activity takes precedent over shorter dynamical transients. In this regime, real-time sensitivity (Shanechi et al., 2016, 2017) and fast error correction (Even-Chen et al., 2017) are more important than perfect first-time decoding. As BCIs begin to better approximate able-bodied precision (Sussillo et al., 2016; Willett et al., 2021; Willsey et al., 2022), the sustained-component of neural activity becomes shorter, and the dynamical transients take up larger proportions of the movement duration.

To further improve decoding, decoders may want to take temporal structure into account, for example explicitly modeling the different phases of BCI movement as motor intent switches from a resting state to a moving state (Sachs et al., 2016; Dekleva et al., 2021). Our results suggest that decoders should be sensitive to a minimum of 3 temporal contexts during movement execution: movement onset, sustained intent, and movement offset. An additional hold state (Sachs et al., 2016; Inoue et al., 2018) and rest state (Velliste et al., 2014) may also be useful for certain applications.

4.4.3 Sensory and non-sensory inputs to motor cortex

Under a dynamical systems framework, the divergence in dynamics between sustained and ballistic movements indicates that the recorded population receives different inputs between the two movement conditions. An open question is where these inputs originate from. During able-bodied reaches, the motor cortex receives rich proprioceptive inputs from S1, which can exhibit similar rotational dynamics (Kalidindi et al., 2021), as well as transformed visual information (Eisenberg et al., 2011) potentially from the posterior parietal cortex (PPC).

Other recent studies have also challenged the autonomous dynamical systems hypothesis by showing that somatosensory input can drive much of the motor cortical activity observed during movement execution (Suresh et al., 2020; Kalidindi et al., 2021). For BCI users moving a cursor with a paralyzed effector, as in our study, somatosensory feedback is severed. Are the observed inputs to motor cortex during sustained activity the direct result of visual feedback or something else? A BCI perturbation study found that visuomotor feedback is initially isolated from the BCI in an output-orthogonal dimension (Stavisky et al., 2017b), suggesting that such inputs would occupy a different subspace until the movement goal was updated otherwise. Furthermore, visual feedback of cursor position only weakly affects MC activity in the absence of movement (Stavisky et al., 2018). However, a more targeted study would be necessary to rule out visual feedback as the direct modulation for MC activity.

To fully determine whether the observed MC inputs are visually driven, we have collected preliminary data where the BCI participant attempted to general similar movements, but where visual feedback was removed by a mask. Our preliminary analysis indicates that MC dynamics and sustained activity are shared between baseline and masked trials. This suggests that the inputs to MC that distinguish sustained from ballistic movements originate from some non-sensory area.

These inputs could from a few candidate areas. First, the thalamus provides time-varying inputs to the motor cortex in mice to enable reaching (Sauerbrei et al., 2020). Second, the supplementary motor area (SMA) tracks timing and context signals that indicate when to start or stop a movement (Gámez et al., 2019; Russo et al., 2020). Finally, the cerebellum and posterior parietal cortex (PPC) compute internal models for sensorimotor control (Mulliken et al., 2008a; Shadmehr and Krakauer, 2008; Franklin and Wolpert, 2011; Guan et al., 2022b), and these may input to MC for goal-directed movements.

4.4.4 Unifying neural dynamics and flexible feedback

Feedback is a core part of flexible movement generation, but the aDSH largely disregards feedback (in the form of external inputs). A complementary framework, optimal feedback control (OFC) (Todorov and Jordan, 2002; Scott, 2004; Shadmehr and Krakauer, 2008; Franklin and Wolpert, 2011), has highlighted the importance of feedback for flexible movement generation. Whereas aDSH asserts that movement execution is predetermined by the initial state and intrinsic dynamics, OFC computes movement controls on-the-fly, taking into account the difference between the current and desired state of effectors. This helps us understand behavior for movements that cannot be predicted at preparation time, such as controlling a new effector (Collinger et al., 2013c; Wodlinger et al., 2015), rapidly adapting to visual target and obstacle modifications (Dimitriou et al., 2013; Nashed et al., 2014; Stavisky et al., 2017b) or load perturbations (Nashed et al., 2014; Cluff and Scott, 2015). Many OFC models posit MC as a feedback controller that integrates information from somatosensory, cerebellar and other areas to achieve the behavioral goal (Scott, 2016). OFC is often formulated as a cost minimization (Diedrichsen et al., 2010).

OFC and the dynamical systems literature have often stood in opposition to or in isolation from each other. However, given both the prevalence of dynamical system tools and the importance of feedback to BCI control, clearly both frameworks provide utility to understanding motor control. A recent review has made an interesting effort to unify OFC and neural dynamical systems (NDS) under the idea of dynamical feedback control (DFC) (Versteeg and Miller, 2022). Additional

experiments may help determine whether this framework can better explain observed phenomena and improve BCI decoding for neuroprosthetic applications.

4.5 Methods

4.5.1 Data collection

4.5.1.1 Study participant

The study participant JJ is a right-handed, tetraplegic man. Approximately 3 years before this study, he sustained a spinal cord injury at cervical level C4-C5. He has residual movement in his upper arms, but he cannot move or feel his hands. As part of a BCI clinical study (ClinicalTrials.gov Identifier: NCT01958086), participant JJ was implanted with two 96-channel Neuroport Utah electrode arrays (Blackrock Microsystems Inc.). He consented to this study after understanding its nature, objectives, and potential risks. All procedures were approved by the Institutional Review Boards of California Institute of Technology, Casa Colina Hospital and Centers for Healthcare, and the University of California, Los Angeles.

4.5.1.2 Multielectrode array implant location

Participant JJ was implanted with two 96-channel NeuroPort Utah electrode arrays about 20 months after injury. One array was implanted near the hand knob of the left motor cortex (MC). A second array was implanted in the superior parietal lobule (SPL) of the left posterior parietal cortex (PPC). Both arrays were used for online BCI decoding, although our analyses here only describe data from the MC implant. More details regarding the methodology for functional localization and implantation can be found in (Guan et al., 2022a).

4.5.1.3 Neural data preprocessing

Using the NeuroPort system (Blackrock Microsystems), neural signals were recorded from the electrode arrays, amplified, analog bandpass-filtered (0.3 Hz to 7.5 kHz), and digitized (30 kHz, 250 nV resolution). A digital high-pass filter (250 Hz) was then applied to each electrode.
Threshold crossings were detected at a threshold of –3.5 x RMS (root-mean-square of an electrode's voltage time-series). Threshold crossings were used as features for in-session BCI control for the Ballistic-Sustained task. For in-session BCI control during the Radial-Grid and Masked-Radial-Grid tasks, we used neural network-extracted features per electrode (Haghi et al., 2021). For offline analyses, we used k-medoids clustering on each electrode to spike-sort the threshold crossing waveforms. The first $n \in \{2, 3, 4\}$ principal components were used as input features to k-medoids, where n was selected for each electrode to account for 95% of waveform variance. The gap criteria (Tibshirani et al., 2001) was used to determine the number of waveform clusters for each electrode.

4.5.2 Experimental setup

4.5.2.1 Recording sessions

Experiments were conducted in recording sessions at Casa Colina Hospital and Centers for Healthcare. All tasks were performed with participant JJ seated in his motorized wheelchair with his

hands resting on his lap or an adjacent armrest. Participant JJ viewed text cues on a 27-inch LCD monitor that occupied approximately 40 degrees of visual angle.
Each session consisted of a series of 2–5 minute, uninterrupted "runs" of the task. The participant rested for a couple minutes between runs as needed.

4.5.2.2 Center-out-and-back calibration task

The center-out-and-back task (e.g. (Jarosiewicz et al., 2013; Kao et al., 2015)) was used to calibrate the decoder for each session. First, a computer controlled the cursor as it moved out to targets and back to the center. The participant simultaneously attempted to move his thumb as though he was controlling the cursor via a thumb joystick. Using this calibration data, we trained a decoder to predict cursor velocity from neural activity.

After open-loop calibration, the participant performed the center-out-and-back task with a relatively low gain. Partial computer assistance was sometimes applied to the cursor trajectories. The purpose of this follow-up task was to collect more data to train the decoder, as recommended by (Jarosiewicz et al., 2013).

On some sessions, the participant repeated the task with a small number of repetitions, so he could familiarize himself with the decoder behavior (Willett et al., 2017b).

4.5.2.3 Center-out brain-computer interface task with variable gain-scaling

The subject used a cursor BCI to complete the center-out task (Georgopoulos et al., 1982; Jarosiewicz et al., 2013) under two decoder gain parameters: high gain for ballistic reaches, and low gain for sustained reaches. The reach duration was tuned to approximately 500 ms (ballistic) or 2 seconds (sustained) using a velocity gain parameter of the neural decoder (Willett et al., 2017b). The ballistic-movement condition is designed to resemble prior NHP reaching experiments. Since closed-loop decoders cannot match the speed and accuracy of NHP behavior, we add computer assistance (error rail, see below Methods) to allow ballistic movements without the need for online corrections.

4.5.2.4 Near-Far center-out brain-computer interface task

We performed an additional center-out task variant to simulate sustained versus ballistic reaches. In the Near-Far variant, targets were positioned at different distances from the center (Supplementary Figure 4.2). The participant was instructed to move the cursor to the target as soon as the target appeared and then relax once the target was reached. Near targets resulted in shorter movement durations (ballistic). Far targets resulted in longer movement durations (sustained). This is functionally similar to modulating the decoder gain directly (Willett et al., 2017a), as was done in the previous Sustained-Ballistic task.

4.5.2.5 Near-Far with mask/delay center-out brain-computer interface task

During able-bodied movement, it can be difficult to dissociate neural activity related to motor output from neural activity related to sensory input (Golub et al., 2015; Kalidindi et al., 2021). When using a paralyzed effector, brain-computer interface control decouples somatosensory feedback from the

motor output. However, visual feedback is still present and could influence motor-related activity, albeit indirectly (Stavisky et al., 2017b).

To isolate the effects of motor intent, we re-ran the Near-Far center-out BCI task with masked trials interleaved (Supplementary Figure 4.3). During the intertrial interval (ITI), the cursor was fixed at the center. A cue indicated the target, during which the participant remained resting. A Delay period separated the visual input in time. The participant was instructed to not (attempt to) move up to this point. Next, the movement phase differed between standard and masked trials. The Go phase of standard trials were like the Go phase in the standard Near-Far task, with participants moving when the target was re-selected, and relaxing once reached (Supplementary Figure 4.2). During masked trials, the participant moved the cursor similarly to trials where he had no visual feedback, relaxing when he had acquired the target. The participant reported that he paced his masked reaches by internally counting to the same intervals as in the standard reaches.

4.5.2.6 Target grid task

The Target Grid task (Nuyujukian et al., 2015) consisted of 5×5 targets arranged in a square grid, resembling an on-screen keyboard interface. Targets were selected randomly one at a time (without replacement within a block), and the participant moved the cursor to each target as fast as possible. The participant was required to hold the cursor within the target acceptance region for 0.5 seconds to complete each trial. The next target was cued immediately after. This task paradigm generates a variety of movement directions and distances (when compared to the standard 8-target center-out task).

4.5.2.7 Computer-assisted control: weighted average

Weighted-average computer assistance blends the decoded velocity with a vector directly towards the target. This type of computer assistance has previously described as "attraction assistance" (Velliste et al., 2008). Assistance values ranged from 0 (full BCI control) to 0.5 (assisted BCI control), where a value of 1 corresponds to full computer control.

4.5.2.8 Computer-assisted control: error rail

Error rail attenuates the components of the decoded velocity that are not directly towards the target. Denoting the direct cursor-target vector as $\vec{d}$, This is accomplished by decomposing the decoding cursor velocity $\vec{v}$ into the component parallel to the target direction $\vec{v}_{\parallel}$ and the component orthogonal to the target direction $\vec{v}_{\perp}$. With assistance value K, the assisted cursor velocity $\hat{v}$ is:

$$\hat{v}_{\perp} = (1-K)\,\vec{v}_{\perp}$$
$$\hat{v}_{\parallel} = \begin{cases} \vec{v}_{\parallel} & if \quad \vec{v}_{\parallel} \cdot \vec{d} > 0 \\ (1-K)\vec{v}_{\parallel} & \text{otherwise} \end{cases}$$
$$\hat{v} = \hat{v}_{\perp} + \hat{v}_{\parallel}\,.$$

Equation 4.5

The assistance value K was specified for each run and ranged from 0 (full BCI control) to 0.3, where a value of 1 restricts the decoder to motion directly towards the target. Error rail is similar in some ways to orthoimpedance (Collinger et al., 2013c; Wodlinger et al., 2015). But also attenuated parallel-component velocities in the reverse direction

4.5.3 Statistical analysis

4.5.3.1 jPCA analysis of rotational structure

We applied jPCA to the spike-sorted neural recordings to uncover oscillatory dynamics, as described previously in (Churchland et al., 2012). We used the ballistic movement window to fit the pre-processing parameters (soft normalization and mean-centering) and jPCA parameters (PCA and axis rotation). Based on known visual system delays , the movement window was assumed to start 150ms after target presentation. We selected the movement window to ended near the average target acquisition time (Figure 4.1), 600ms after target presentation. We then applied jPCA (with the previously fit parameters) to visualize entire trials, including the latter part of sustained movements or the movement relaxation phase.

We tested our jPCA results against the null hypothesis that the rotational dynamics are a byproduct of the population firing rate's smoothness and tuning properties. We used tensor maximum entropy (TME) (Elsayed and Cunningham, 2017) to generate surrogate datasets with the same covariances across neurons, conditions (i.e., targets), and time. jPCA was applied to each surrogate dataset to generate a null distribution for testing statistical significance.

4.5.3.2 Neural population speed

A related study (Kao et al., 2015) defines neural population speed as $\|\boldsymbol{r}_{k+1} - \boldsymbol{r}_k\|_2$. We use a similar definition here while addressing one statistical drawback in the original formulation: noise biases Euclidean distances upward (Walther et al., 2016). In other words, adding independent Gaussian noise to the firing rates increases $\|\boldsymbol{r}_{k+1} - \boldsymbol{r}_k\|_2$**,** even when the true neural population speed does not change otherwise**.** To find an unbiased estimate of the neural speed, it is useful to cross-validate speed estimates across independent partitions of trial repetitions (Walther et al., 2016):

$$\|\dot{r}\|_{cv}^2 \coloneqq (\boldsymbol{r}_{k+1} - \boldsymbol{r}_k)_A \left(\frac{\Sigma_A + \Sigma_B}{2}\right)^{-1} (\boldsymbol{r}_{k+1} - \boldsymbol{r}_k)_B^T$$

Equation 4.6

where A and B indicate independent partitions of the trials, Σ is the (regularized (Ledoit and Wolf, 2003)) noise covariance matrix, $\boldsymbol{r}_k$ are the firing rate vectors for time index k stacked across the respective partition's trials. This is sometimes normalized by the number of neurons. The units of $\|\dot{r}\|_{cv}^2$ are $(\text{Hz} \,/\, s)^2$.

The cross-validated squared neural speed $\|\dot{r}\|_{cv}^2$ estimates the noise-normalized magnitude of the neural velocity that is consistent across trial repetitions. Here, we often abbreviate this metric as "neural speed," although it is often referred to as the cross-validated Mahalanobis distance elsewhere (Walther et al., 2016).

4.5.4 Closed-loop decoding pipelines

4.5.4.1 Neural dynamical filter (NDF)

During the sustained and ballistic BCI cursor task, we preprocessed the neural activity by binning spike counts at non-overlapping 30-ms bins, z-scoring the firing rates for each channel, and reducing the dimensionality to the first 15 principal components. We decoded movement intent from the reduced-dimensionality population activity using the neural dynamical filter (NDF) (Kao et al., 2015) with a 10-dimensional latent state. NDF learns a latent-state linear dynamical system of the neural population activity. For online decoding, NDF linearly predicts kinematics from the dynamics-filtered latent states. The NDF is described in detail in (Kao et al., 2015).

4.5.4.2 Linear regression with neural-network-extracted broadband features

In later tasks, recordings yielded few high-SNR waveforms, so we switched from threshold-crossing rates to broadband features. We used a temporal convolutional neural network (denoted "FENet") to extract features from 30kHz-sampled raw voltage timeseries (Haghi et al., 2021). These features can intuitively be thought of as highly-processed local field potentials (LFPs).
Before inputting to the linear decoder, we preprocessed FENet features in a series of steps. First, we z-scored input features. Next, to prevent unexpected channel noise from disproportionately degrading decoding, we bound the z-scored values between [–3, 6] (σ). Because FENet generates multiple (K=8) features per electrode, we used partial-least squares regression to reduce this number to (K=2) informative features for each electrode. Next, we reduced feature dimensionality by using partial least squares to predict the input features smoothed by an 800-ms minimum-jerk kernel; this is analogous to a linear autoencoder and helps to denoise data that is expected to be autocorrelated. Finally, the firing rates were smoothed with an exponential filter (time-constant = 585ms).

4.6 Acknowledgments

Thank you, JJ, for your participation. Tyson Aflalo, Jorge Gámez de Leon, and Kelly Kadlec were close collaborators on this project, which is part of a long-term collaboration with Emily Rosario and Ausaf Bari.

4.7 Supplementary Material

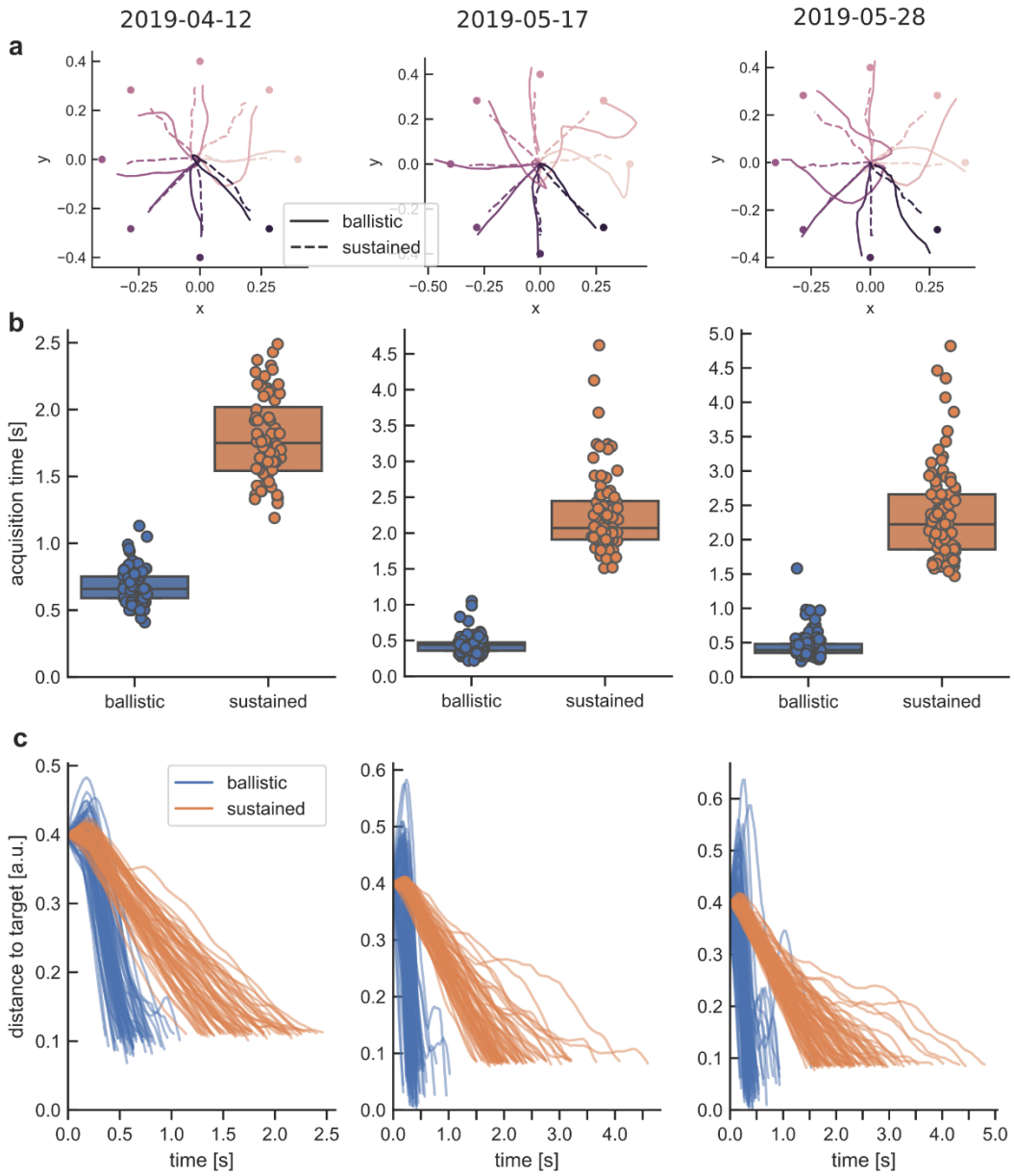

Supplementary Figure 4.1. Behavioral kinematics for all sessions of ballistic and sustained BCI cursor movements.
(**a**) Example single-trial cursor trajectories for each session.
(**b**) Target acquisition time. Each circle indicates a single trial, and box-plot lines indicate the lower quartile, median, and upper quartile, respectively.
(**c**) Distance-to-target in normalized screen units. Each line indicates a single trial.

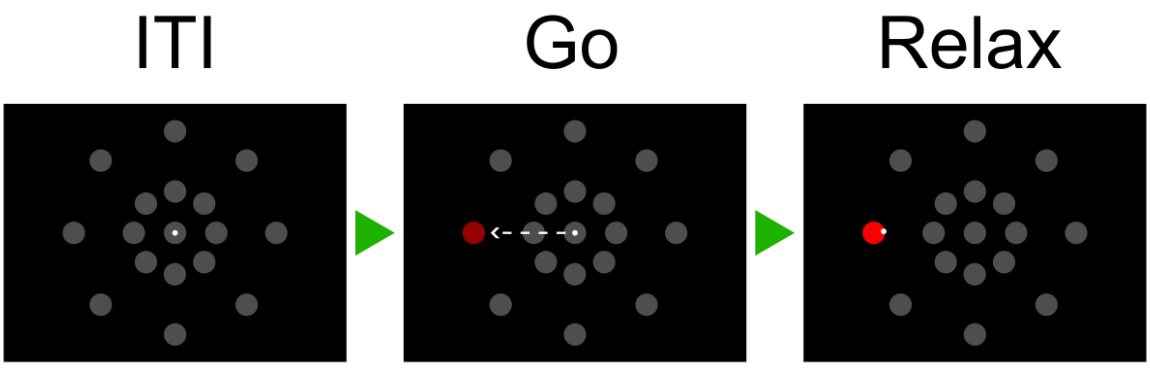

Supplementary Figure 4.2. Near and far center-out task
Task that emulates ballistic and sustained reaches through targets near and distant from the center-start. Dashed arrow visualizes intended movement direction for reference but was not shown during the actual task.

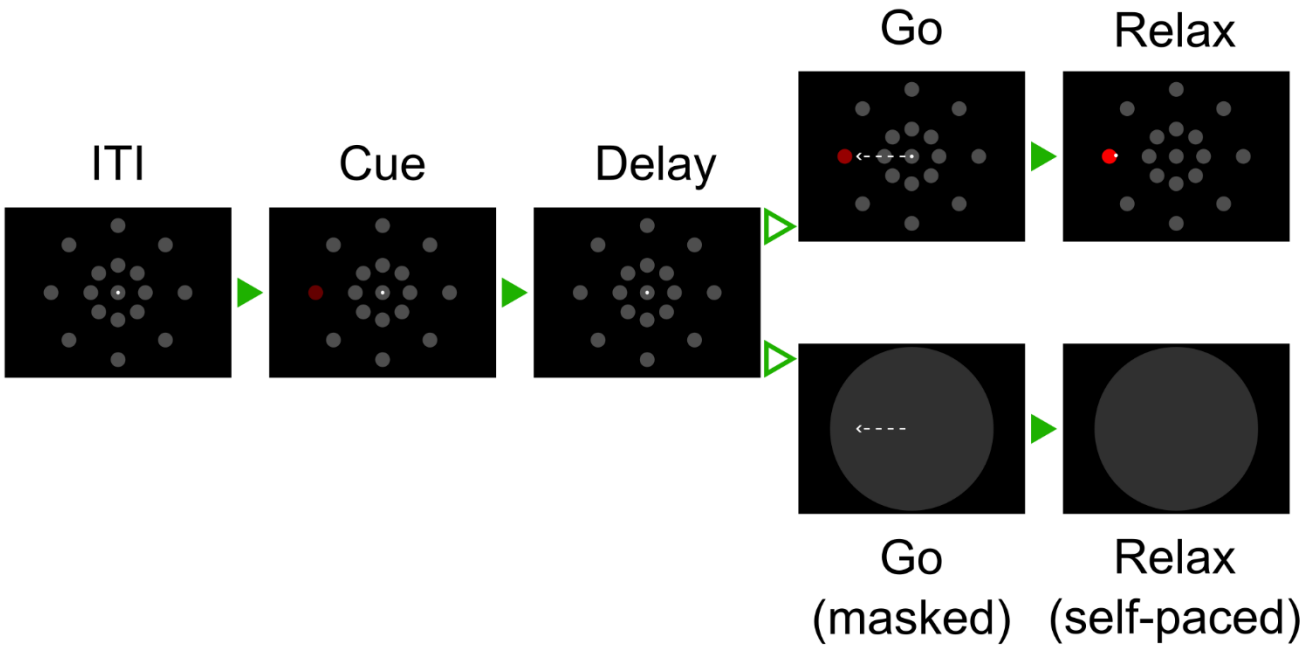

Supplementary Figure 4.3. Near and far center-out task with instructed delay and interleaved masking.

This task included different distances for sustained and ballistic reaches. On interleaved trials, a target / cursor mask Dashed arrow visualizes the instructed movement direction for reference, although it was not shown in the actual experiment. The cursor was fixed at the center during the ITI, Cue, and Delay phases, and the participant was instructed to not move during these periods. During the baseline Go variant, the participant moved the cursor to the target and relaxed once the target was acquired. During the masked Go variant, the participant moved the cursor to the remembered target and relaxed based on self-pacing.

5 Conclusions

Dexterous hand movements are important for everyday tasks (Yan et al., 2020), and restoring hand function is a top priority for people with tetraplegia (Anderson, 2004; Snoek et al., 2004; Collinger et al., 2013a). In this dissertation, we demonstrate that brain-computer interfaces could help to restore fine motor function. Finger-related cortical circuits in two tetraplegic participants remained functional even years after paralysis, allowing neural decoding of finger movements in a variety of tasks. Decoding performance was strong even in the grasping areas of the posterior parietal cortex (PPC), outside of the primary sensorimotor cortex. These findings suggest that manual dexterity may be supported by a broader neuronal network than is commonly thought. By combining signals from both the motor cortex and posterior parietal cortex, we were able to achieve state-of-the-art finger classification accuracies. We further studied the temporal structure of neural activity during BCI control. External inputs, such as sensory feedback, are important for robust BCI control during everyday usage.

5.1 Next steps: a neuroprosthetic assistant through hybrid control

To fully benefit tetraplegic people, neuroprosthetic systems will need the ability to manipulate objects for everyday tasks, such as eating. Unfortunately, this kind of dexterity (Yan et al., 2020) far exceeds current decoding capabilities. Without substantial advancements in recording yield, hand decoding may be limited to only two fingers for continuous control (Nason et al., 2021; Willsey et al., 2022) or only discrete control for all ten fingers, as described here. Even after recording yields improve, BCIs lack the spinal cord circuitry that implements important control loops, such as regulating contact forces for grasping fragile objects (Downey et al., 2017; Weiler et al., 2019).

In the past decade, several studies have taken a parallel, hybrid approach to augment neuroprosthetic control. Building off advances in computing, (Katyal et al., 2014; Downey et al., 2016; Muelling et al., 2017) blended BCI control with vision-guided autonomous robotics. In these demonstrations, BCIs commanded the high-level trajectory while computer assistance inferred target objects and stabilizes the robotic arm during grasping. This approach can be further integrated with eye-tracking for sensor fusion with neuroprosthetic control (McMullen et al., 2014). Since these initial demonstrations, real-time computer vision algorithms have improved substantially. It may soon be possible for computer vision assistance to infer a library of grasp options for each object, which can be combined with BCI control for real-time dexterous control.

References

Adams, R.A., Shipp, S., Friston, K.J., 2013. Predictions not commands: active inference in the motor system. Brain Struct. Funct. 218, 611–643. doi:10.1007/s00429-012-0475-5

Aflalo, T., Chivukula, S., Zhang, C., Rosario, E.R., Pouratian, N., Andersen, R.A., 2022. Cognition through internal models: Mirror neurons as one manifestation of a broader mechanism. BioRxiv. doi:10.1101/2022.09.06.506071

Aflalo, T., Kellis, S., Klaes, C., Lee, B., Shi, Y., Pejsa, K., Shanfield, K., Hayes-Jackson, S., Aisen, M., Heck, C., Liu, C., Andersen, R.A., 2015. Neurophysiology. Decoding motor imagery from the posterior parietal cortex of a tetraplegic human. Science 348, 906–910. doi:10.1126/science.aaa5417

Aflalo, T., Zhang, C.Y., Rosario, E.R., Pouratian, N., Orban, G.A., Andersen, R.A., 2020. A shared neural substrate for action verbs and observed actions in human posterior parietal cortex. Sci. Adv. 6. doi:10.1126/sciadv.abb3984

Aflalo, T.N., Graziano, M.S.A., 2006. Partial tuning of motor cortex neurons to final posture in a free-moving paradigm. Proc. Natl. Acad. Sci. USA 103, 2909–2914. doi:10.1073/pnas.0511139103

Aflalo, T.N., Graziano, M.S.A., 2007. Relationship between unconstrained arm movements and single-neuron firing in the macaque motor cortex. J. Neurosci. 27, 2760–2780. doi:10.1523/JNEUROSCI.3147-06.2007

Ajiboye, A.B., Willett, F.R., Young, D.R., Memberg, W.D., Murphy, B.A., Miller, J.P., Walter, B.L., Sweet, J.A., Hoyen, H.A., Keith, M.W., Peckham, P.H., Simeral, J.D., Donoghue, J.P., Hochberg, L.R., Kirsch, R.F., 2017. Restoration of reaching and grasping movements through brain-controlled muscle stimulation in a person with tetraplegia: a proof-of-concept demonstration. Lancet 389, 1821–1830. doi:10.1016/S0140-6736(17)30601-3

Allison, J.D., Meador, K.J., Loring, D.W., Figueroa, R.E., Wright, J.C., 2000. Functional MRI cerebral activation and deactivation during finger movement. Neurology 54, 135–142. doi:10.1212/wnl.54.1.135

Andersen, R.A., Aflalo, T., 2022. Preserved cortical somatotopic and motor representations in tetraplegic humans. Curr. Opin. Neurobiol. 74, 102547. doi:10.1016/j.conb.2022.102547

Andersen, R.A., Aflalo, T., Kellis, S., 2019. From thought to action: The brain-machine interface in posterior parietal cortex. Proc. Natl. Acad. Sci. USA. doi:10.1073/pnas.1902276116

Andersen, R.A., Andersen, K.N., Hwang, E.J., Hauschild, M., 2014. Optic ataxia: from Balint's syndrome to the parietal reach region. Neuron 81, 967–983. doi:10.1016/j.neuron.2014.02.025

Andersen, R.A., Essick, G.K., Siegel, R.M., 1985. Encoding of spatial location by posterior parietal neurons. Science 230, 456–458. doi:10.1126/science.4048942

Andersen, R.A., Essick, G.K., Siegel, R.M., 1987. Neurons of area 7 activated by both visual stimuli and oculomotor behavior. Exp. Brain Res. 67, 316–322. doi:10.1007/bf00248552

Andersen, R.A., Snyder, L.H., Bradley, D.C., Xing, J., 1997. Multimodal representation of space in the posterior parietal cortex and its use in planning movements. Annu. Rev. Neurosci. 20, 303–330. doi:10.1146/annurev.neuro.20.1.303

Anderson, K.D., 2004. Targeting recovery: priorities of the spinal cord-injured population. J. Neurotrauma 21, 1371–1383. doi:10.1089/neu.2004.21.1371

Anumanchipalli, G.K., Chartier, J., Chang, E.F., 2019. Speech synthesis from neural decoding of spoken sentences. Nature 568, 493–498. doi:10.1038/s41586-019-1119-1

Arbuckle, S.A., Weiler, J., Kirk, E.A., Rice, C.L., Schieber, M., Pruszynski, J.A., Ejaz, N., Diedrichsen, J., 2020. Structure of population activity in primary motor cortex for single finger flexion and extension. J. Neurosci. 40, 9210–9223. doi:10.1523/JNEUROSCI.0999-20.2020

Ariani, G., Pruszynski, J.A., Diedrichsen, J., 2022. Motor planning brings human primary somatosensory cortex into action-specific preparatory states. Elife 11. doi:10.7554/eLife.69517

Armenta Salas, M., Bashford, L., Kellis, S., Jafari, M., Jo, H., Kramer, D., Shanfield, K., Pejsa, K., Lee, B., Liu, C.Y., Andersen, R.A., 2018. Proprioceptive and cutaneous sensations in humans elicited by intracortical microstimulation. Elife 7. doi:10.7554/eLife.32904

Armour, B.S., Courtney-Long, E.A., Fox, M.H., Fredine, H., Cahill, A., 2016. Prevalence and Causes of Paralysis-United States, 2013. Am. J. Public Health 106, 1855–1857. doi:10.2105/AJPH.2016.303270

Baldwin, M.K.L., Cooke, D.F., Goldring, A.B., Krubitzer, L., 2018. Representations of Fine Digit Movements in Posterior and Anterior Parietal Cortex Revealed Using Long-Train Intracortical Microstimulation in Macaque Monkeys. Cereb. Cortex 28, 4244–4263. doi:10.1093/cercor/bhx279

Baseler, H.A., Gouws, A., Haak, K.V., Racey, C., Crossland, M.D., Tufail, A., Rubin, G.S., Cornelissen, F.W., Morland, A.B., 2011. Large-scale remapping of visual cortex is absent in adult humans with macular degeneration. Nat. Neurosci. 14, 649–655. doi:10.1038/nn.2793

Bernardi, S., Benna, M.K., Rigotti, M., Munuera, J., Fusi, S., Salzman, C.D., 2020. The geometry of abstraction in the hippocampus and prefrontal cortex. Cell 183, 954–967.e21. doi:10.1016/j.cell.2020.09.031

Billard, A., Kragic, D., 2019. Trends and challenges in robot manipulation. Science 364. doi:10.1126/science.aat8414

Binkofski, F., Dohle, C., Posse, S., Stephan, K.M., Hefter, H., Seitz, R.J., Freund, H.J., 1998. Human anterior intraparietal area subserves prehension: a combined lesion and functional MRI activation study. Neurology 50, 1253–1259. doi:10.1212/wnl.50.5.1253

Bockbrader, M., 2019. Upper limb sensorimotor restoration through brain–computer interface technology in tetraparesis. Current Opinion in Biomedical Engineering 11, 85–101. doi:10.1016/j.cobme.2019.09.002

Bonnasse-Gahot, L., Nadal, J.-P., 2008. Neural coding of categories: information efficiency and optimal population codes. J. Comput. Neurosci. 25, 169–187. doi:10.1007/s10827-007-0071-5

Bouton, C.E., Shaikhouni, A., Annetta, N.V., Bockbrader, M.A., Friedenberg, D.A., Nielson, D.M., Sharma, G., Sederberg, P.B., Glenn, B.C., Mysiw, W.J., Morgan, A.G., Deogaonkar, M., Rezai, A.R., 2016. Restoring cortical control of functional movement in a human with quadriplegia. Nature 533, 247–250. doi:10.1038/nature17435

Brainard, D.H., 1997. The Psychophysics Toolbox. Spat Vis. 10, 433–436. doi:10.1163/156856897X00357

Brandman, D.M., Hosman, T., Saab, J., Burkhart, M.C., Shanahan, B.E., Ciancibello, J.G., Sarma, A.A., Milstein, D.J., Vargas-Irwin, C.E., Franco, B., Kelemen, J., Blabe, C., Murphy, B.A., Young, D.R., Willett, F.R., Pandarinath, C., Stavisky, S.D., Kirsch, R.F., Walter, B.L., Bolu Ajiboye, A., Cash, S.S., Eskandar, E.N., Miller, J.P., Sweet, J.A., Shenoy, K.V., Henderson, J.M., Jarosiewicz, B., Harrison, M.T., Simeral, J.D., Hochberg, L.R., 2018. Rapid calibration of an intracortical brain-computer interface for people with tetraplegia. J. Neural Eng. 15, 026007. doi:10.1088/1741-2552/aa9ee7

Bruurmijn, M.L.C.M., Pereboom, I.P.L., Vansteensel, M.J., Raemaekers, M.A.H., Ramsey, N.F., 2017. Preservation of hand movement representation in the sensorimotor areas of amputees. Brain 140, 3166–3178. doi:10.1093/brain/awx274

Bundy, D.T., Szrama, N., Pahwa, M., Leuthardt, E.C., 2018. Unilateral, 3D arm movement kinematics are encoded in ipsilateral human cortex. J. Neurosci. 38, 10042–10056. doi:10.1523/JNEUROSCI.0015-18.2018

Buneo, C.A., Andersen, R.A., 2006. The posterior parietal cortex: sensorimotor interface for the planning and online control of visually guided movements. Neuropsychologia 44, 2594–2606. doi:10.1016/j.neuropsychologia.2005.10.011

Carmena, J.M., Lebedev, M.A., Crist, R.E., O'Doherty, J.E., Santucci, D.M., Dimitrov, D.F., Patil, P.G., Henriquez, C.S., Nicolelis, M.A.L., 2003. Learning to control a brain-machine interface for reaching and grasping by primates. PLoS Biol. 1, E42. doi:10.1371/journal.pbio.0000042

Cavina-Pratesi, C., Connolly, J.D., Monaco, S., Figley, T.D., Milner, A.D., Schenk, T., Culham, J.C., 2018. Human neuroimaging reveals the subcomponents of grasping, reaching and pointing actions. Cortex 98, 128–148. doi:10.1016/j.cortex.2017.05.018

Chestek, C.A., Gilja, V., Nuyujukian, P., Foster, J.D., Fan, J.M., Kaufman, M.T., Churchland, M.M., Rivera-Alvidrez, Z., Cunningham, J.P., Ryu, S.I., Shenoy, K.V., 2011. Long-term stability of neural prosthetic control signals from silicon cortical arrays in rhesus macaque motor cortex. J. Neural Eng. 8, 045005. doi:10.1088/1741-2560/8/4/045005

Chivukula, S., Zhang, C.Y., Aflalo, T., Jafari, M., Pejsa, K., Pouratian, N., Andersen, R.A., 2021. Neural encoding of actual and imagined touch within human posterior parietal cortex. Elife 10. doi:10.7554/eLife.61646

Churchland, M.M., Cunningham, J.P., Kaufman, M.T., Foster, J.D., Nuyujukian, P., Ryu, S.I., Shenoy, K.V., 2012. Neural population dynamics during reaching. Nature 487, 51–56. doi:10.1038/nature11129

Churchland, M.M., Cunningham, J.P., Kaufman, M.T., Ryu, S.I., Shenoy, K.V., 2010. Cortical preparatory activity: representation of movement or first cog in a dynamical machine? Neuron 68, 387–400. doi:10.1016/j.neuron.2010.09.015

Churchland, M.M., Shenoy, K.V., 2007. Temporal complexity and heterogeneity of single-neuron activity in premotor and motor cortex. J. Neurophysiol. 97, 4235–4257. doi:10.1152/jn.00095.2007

Clancy, K.B., Koralek, A.C., Costa, R.M., Feldman, D.E., Carmena, J.M., 2014. Volitional modulation of optically recorded calcium signals during neuroprosthetic learning. Nat. Neurosci. 17, 807–809. doi:10.1038/nn.3712

Cluff, T., Scott, S.H., 2015. Apparent and actual trajectory control depend on the behavioral context in upper limb motor tasks. J. Neurosci. 35, 12465–12476. doi:10.1523/JNEUROSCI.0902-15.2015

Cohen, J., 1988. Statistical power analysis for the behavioral sciences, 2nd ed. Lawrence Erlbaum Associates, New Jersey, NJ. doi:10.4324/9780203771587

Collinger, J.L., Boninger, M.L., Bruns, T.M., Curley, K., Wang, W., Weber, D.J., 2013a. Functional priorities, assistive technology, and brain-computer interfaces after spinal cord injury. J Rehabil Res Dev 50, 145–160. doi:10.1682/jrrd.2011.11.0213

Collinger, J.L., Foldes, S., Bruns, T.M., Wodlinger, B., Gaunt, R., Weber, D.J., 2013b. Neuroprosthetic technology for individuals with spinal cord injury. J Spinal Cord Med 36, 258–272. doi:10.1179/2045772313Y.0000000128

Collinger, J.L., Gaunt, R.A., Schwartz, A.B., 2018. Progress towards restoring upper limb movement and sensation through intracortical brain-computer interfaces. Current Opinion in Biomedical Engineering 8, 84–92. doi:10.1016/j.cobme.2018.11.005

Collinger, J.L., Wodlinger, B., Downey, J.E., Wang, W., Tyler-Kabara, E.C., Weber, D.J., McMorland, A.J.C., Velliste, M., Boninger, M.L., Schwartz, A.B., 2013c. High-performance neuroprosthetic control by an individual with tetraplegia. Lancet 381, 557–564. doi:10.1016/S0140-6736(12)61816-9

Cooke, D.F., Taylor, C.S.R., Moore, T., Graziano, M.S.A., 2003. Complex movements evoked by microstimulation of the ventral intraparietal area. Proc. Natl. Acad. Sci. USA 100, 6163–6168. doi:10.1073/pnas.1031751100

Dabagia, M., Kording, K.P., Dyer, E.L., 2022. Aligning latent representations of neural activity. Nat. Biomed. Eng. doi:10.1038/s41551-022-00962-7

Degenhart, A.D., Bishop, W.E., Oby, E.R., Tyler-Kabara, E.C., Chase, S.M., Batista, A.P., Yu, B.M., 2020. Stabilization of a brain-computer interface via the alignment of low-dimensional spaces of neural activity. Nat. Biomed. Eng. 4, 672–685. doi:10.1038/s41551-020-0542-9

Dekleva, B.M., Weiss, J.M., Boninger, M.L., Collinger, J.L., 2021. Generalizable cursor click decoding using grasp-related neural transients. J. Neural Eng. 18. doi:10.1088/1741-2552/ac16b2

Desmurget, M., Grafton, S., 2000. Forward modeling allows feedback control for fast reaching movements. Trends Cogn. Sci. (Regul. Ed.) 4, 423–431. doi:10.1016/s1364-6613(00)01537-0

Diedrichsen, J., Berlot, E., Mur, M., Schütt, H.H., Shahbazi, M., Kriegeskorte, N., 2021. Comparing representational geometries using whitened unbiased-distance-matrix similarity. Neurons, Behavior, Data analysis, and Theory. doi:10.51628/001c.27664

Diedrichsen, J., Kriegeskorte, N., 2017. Representational models: A common framework for understanding encoding, pattern-component, and representational-similarity analysis. PLoS Comput. Biol. 13, e1005508. doi:10.1371/journal.pcbi.1005508

Diedrichsen, J., Shadmehr, R., Ivry, R.B., 2010. The coordination of movement: optimal feedback control and beyond. Trends Cogn. Sci. (Regul. Ed.) 14, 31–39. doi:10.1016/j.tics.2009.11.004

Diedrichsen, J., Wiestler, T., Krakauer, J.W., 2013. Two distinct ipsilateral cortical representations for individuated finger movements. Cereb. Cortex 23, 1362–1377. doi:10.1093/cercor/bhs120

Dienes, Z., 2014. Using Bayes to get the most out of non-significant results. Front. Psychol. 5, 781. doi:10.3389/fpsyg.2014.00781

Dimitriou, M., Wolpert, D.M., Franklin, D.W., 2013. The temporal evolution of feedback gains rapidly update to task demands. J. Neurosci. 33, 10898–10909. doi:10.1523/JNEUROSCI.5669-12.2013

Downey, J.E., Brane, L., Gaunt, R.A., Tyler-Kabara, E.C., Boninger, M.L., Collinger, J.L., 2017. Motor cortical activity changes during neuroprosthetic-controlled object interaction. Sci. Rep. 7, 16947. doi:10.1038/s41598-017-17222-3

Downey, J.E., Quick, K.M., Schwed, N., Weiss, J.M., Wittenberg, G.F., Boninger, M.L., Collinger, J.L., 2020. The motor cortex has independent representations for ipsilateral and contralateral arm movements but correlated representations for grasping. Cereb. Cortex 30, 5400–5409. doi:10.1093/cercor/bhaa120

Downey, J.E., Weiss, J.M., Muelling, K., Venkatraman, A., Valois, J.-S., Hebert, M., Bagnell, J.A., Schwartz, A.B., Collinger, J.L., 2016. Blending of brain-machine interface and vision-guided autonomous robotics improves neuroprosthetic arm performance during grasping. J Neuroeng Rehabil 13, 28. doi:10.1186/s12984-016-0134-9

Dudoit, S., Fridlyand, J., Speed, T.P., 2002. Comparison of Discrimination Methods for the Classification of Tumors Using Gene Expression Data. J. Am. Stat. Assoc. 97, 77–87. doi:10.1198/016214502753479248

Dunnett, C.W., 1964. New Tables for Multiple Comparisons with a Control. Biometrics 20, 482. doi:10.2307/2528490

Eickhoff, S.B., Constable, R.T., Yeo, B.T.T., 2018. Topographic organization of the cerebral cortex and brain cartography. Neuroimage 170, 332–347. doi:10.1016/j.neuroimage.2017.02.018

Eisenberg, M., Shmuelof, L., Vaadia, E., Zohary, E., 2011. The representation of visual and motor aspects of reaching movements in the human motor cortex. J. Neurosci. 31, 12377–12384. doi:10.1523/JNEUROSCI.0824-11.2011

Ejaz, N., Hamada, M., Diedrichsen, J., 2015. Hand use predicts the structure of representations in sensorimotor cortex. Nat. Neurosci. 18, 1034–1040. doi:10.1038/nn.4038

Elsayed, G.F., Cunningham, J.P., 2017. Structure in neural population recordings: an expected byproduct of simpler phenomena? Nat. Neurosci. 20, 1310–1318. doi:10.1038/nn.4617

Elsayed, G.F., Lara, A.H., Kaufman, M.T., Churchland, M.M., Cunningham, J.P., 2016. Reorganization between preparatory and movement population responses in motor cortex. Nat. Commun. 7, 13239. doi:10.1038/ncomms13239

Ethier, C., Oby, E.R., Bauman, M.J., Miller, L.E., 2012. Restoration of grasp following paralysis through brain-controlled stimulation of muscles. Nature 485, 368–371. doi:10.1038/nature10987

Evarts, E.V., 1968. Relation of pyramidal tract activity to force exerted during voluntary movement. J. Neurophysiol. 31, 14–27. doi:10.1152/jn.1968.31.1.14

Even-Chen, N., Stavisky, S.D., Kao, J.C., Ryu, S.I., Shenoy, K.V., 2017. Augmenting intracortical brain-machine interface with neurally driven error detectors. J. Neural Eng. 14, 066007. doi:10.1088/1741-2552/aa8dc1

Fetz, E.E., 1969. Operant conditioning of cortical unit activity. Science 163, 955–958. doi:10.1126/science.163.3870.955

Fetz, E.E., 1992. Are movement parameters recognizably coded in the activity of single neurons? Behav. Brain Sci. 15, 679–690.

Fifer, M.S., McMullen, D.P., Osborn, L.E., Thomas, T.M., Christie, B.P., Nickl, R.W., Candrea, D.N., Pohlmeyer, E.A., Thompson, M.C., Anaya, M.A., Schellekens, W., Ramsey, N.F., Bensmaia, S.J., Anderson, W.S., Wester, B.A., Crone, N.E., Celnik, P.A., Cantarero, G.L., Tenore, F.V., 2021. Intracortical somatosensory stimulation to elicit fingertip sensations in an individual with spinal cord injury. Neurology. doi:10.1212/WNL.0000000000013173

Flesher, S.N., Collinger, J.L., Foldes, S.T., Weiss, J.M., Downey, J.E., Tyler-Kabara, E.C., Bensmaia, S.J., Schwartz, A.B., Boninger, M.L., Gaunt, R.A., 2016. Intracortical microstimulation of human somatosensory cortex. Sci. Transl. Med. 8, 361ra141. doi:10.1126/scitranslmed.aaf8083

Flesher, S.N., Downey, J.E., Weiss, J.M., Hughes, C.L., Herrera, A.J., Tyler-Kabara, E.C., Boninger, M.L., Collinger, J.L., Gaunt, R.A., 2021. A brain-computer interface that evokes tactile sensations improves robotic arm control. Science 372, 831–836. doi:10.1126/science.abd0380

Flint, R.D., Wright, Z.A., Scheid, M.R., Slutzky, M.W., 2013. Long term, stable brain machine interface performance using local field potentials and multiunit spikes. J. Neural Eng. 10, 056005. doi:10.1088/1741-2560/10/5/056005

Fougner, A., Stavdahl, O., Kyberd, P.J., Losier, Y.G., Parker, P.A., 2012. Control of upper limb prostheses: terminology and proportional myoelectric control-a review. IEEE Trans Neural Syst Rehabil Eng 20, 663–677. doi:10.1109/TNSRE.2012.2196711

Frankland, S.M., Greene, J.D., 2020. Concepts and compositionality: in search of the brain's language of thought. Annu. Rev. Psychol. 71, 273–303. doi:10.1146/annurev-psych-122216-011829

Franklin, D.W., Wolpert, D.M., 2011. Computational mechanisms of sensorimotor control. Neuron 72, 425–442. doi:10.1016/j.neuron.2011.10.006

Friel, K.M., Barbay, S., Frost, S.B., Plautz, E.J., Hutchinson, D.M., Stowe, A.M., Dancause, N., Zoubina, E.V., Quaney, B.M., Nudo, R.J., 2005. Dissociation of sensorimotor deficits after rostral versus caudal lesions in the primary motor cortex hand representation. J. Neurophysiol. 94, 1312–1324. doi:10.1152/jn.01251.2004

Fu, Z., Beam, D., Chung, J.M., Reed, C.M., Mamelak, A.N., Adolphs, R., Rutishauser, U., 2022. The geometry of domain-general performance monitoring in the human medial frontal cortex. Science 376, eabm9922. doi:10.1126/science.abm9922

Gail, A., Klaes, C., Westendorff, S., 2009. Implementation of spatial transformation rules for goal-directed reaching via gain modulation in monkey parietal and premotor cortex. J. Neurosci. 29, 9490–9499. doi:10.1523/JNEUROSCI.1095-09.2009

Gallego, J.A., Perich, M.G., Chowdhury, R.H., Solla, S.A., Miller, L.E., 2020. Long-term stability of cortical population dynamics underlying consistent behavior. Nat. Neurosci. 23, 260–270. doi:10.1038/s41593-019-0555-4

Gallese, V., Murata, A., Kaseda, M., Niki, N., Sakata, H., 1994. Deficit of hand preshaping after muscimol injection in monkey parietal cortex. Neuroreport 5, 1525–1529. doi:10.1097/00001756-199407000-00029

Gallivan, J.P., Culham, J.C., 2015. Neural coding within human brain areas involved in actions. Curr. Opin. Neurobiol. 33, 141–149. doi:10.1016/j.conb.2015.03.012

Gallivan, J.P., McLean, D.A., Valyear, K.F., Culham, J.C., 2013. Decoding the neural mechanisms of human tool use. Elife 2, e00425. doi:10.7554/eLife.00425

Gámez, J., Mendoza, G., Prado, L., Betancourt, A., Merchant, H., 2019. The amplitude in periodic neural state trajectories underlies the tempo of rhythmic tapping. PLoS Biol. 17, e3000054. doi:10.1371/journal.pbio.3000054

Ganguly, K., Carmena, J.M., 2009. Emergence of a stable cortical map for neuroprosthetic control. PLoS Biol. 7, e1000153. doi:10.1371/journal.pbio.1000153

Gao, P., Trautmann, E., Yu, B.M., Santhanam, G., Ryu, S., Shenoy, K., Ganguli, S., 2017. A theory of multineuronal dimensionality, dynamics and measurement. BioRxiv. doi:10.1101/214262

Georgopoulos, A.P., Ashe, J., Smyrnis, N., Taira, M., 1992. The motor cortex and the coding of force. Science 256, 1692–1695. doi:10.1126/science.256.5064.1692

Georgopoulos, A.P., Kalaska, J.F., Caminiti, R., Massey, J.T., 1982. On the relations between the direction of two-dimensional arm movements and cell discharge in primate motor cortex. J. Neurosci. 2, 1527–1537. doi:10.1523/JNEUROSCI.02-11-01527.1982

Georgopoulos, A.P., Schwartz, A.B., Kettner, R.E., 1986. Neuronal population coding of movement direction. Science 233, 1416–1419. doi:10.1126/science.3749885

Ghez, C., Gordon, J., Ghilardi, M.F., 1995. Impairments of reaching movements in patients without proprioception. II. Effects of visual information on accuracy. J. Neurophysiol. 73, 361–372. doi:10.1152/jn.1995.73.1.361

Gilbert, C.D., Wiesel, T.N., 1992. Receptive field dynamics in adult primary visual cortex. Nature 356, 150–152. doi:10.1038/356150a0

Gilja, V., Nuyujukian, P., Chestek, C.A., Cunningham, J.P., Yu, B.M., Fan, J.M., Churchland, M.M., Kaufman, M.T., Kao, J.C., Ryu, S.I., Shenoy, K.V., 2012. A high-performance neural prosthesis enabled by control algorithm design. Nat. Neurosci. 15, 1752–1757. doi:10.1038/nn.3265

Gilja, V., Pandarinath, C., Blabe, C.H., Nuyujukian, P., Simeral, J.D., Sarma, A.A., Sorice, B.L., Perge, J.A., Jarosiewicz, B., Hochberg, L.R., Shenoy, K.V., Henderson, J.M., 2015. Clinical translation of a high-performance neural prosthesis. Nat. Med. 21, 1142–1145. doi:10.1038/nm.3953

Glasser, M.F., Coalson, T.S., Robinson, E.C., Hacker, C.D., Harwell, J., Yacoub, E., Ugurbil, K., Andersson, J., Beckmann, C.F., Jenkinson, M., Smith, S.M., Van Essen, D.C., 2016. A multi-modal parcellation of human cerebral cortex. Nature 536, 171–178. doi:10.1038/nature18933

Golub, M.D., Chase, S.M., Batista, A.P., Yu, B.M., 2016. Brain-computer interfaces for dissecting cognitive processes underlying sensorimotor control. Curr. Opin. Neurobiol. 37, 53–58. doi:10.1016/j.conb.2015.12.005

Golub, M.D., Sadtler, P.T., Oby, E.R., Quick, K.M., Ryu, S.I., Tyler-Kabara, E.C., Batista, A.P., Chase, S.M., Yu, B.M., 2018. Learning by neural reassociation. Nat. Neurosci. 21, 607–616. doi:10.1038/s41593-018-0095-3

Golub, M.D., Yu, B.M., Chase, S.M., 2015. Internal models for interpreting neural population activity during sensorimotor control. Elife 4. doi:10.7554/eLife.10015

Goodman, J.M., Tabot, G.A., Lee, A.S., Suresh, A.K., Rajan, A.T., Hatsopoulos, N.G., Bensmaia, S., 2019. Postural representations of the hand in the primate sensorimotor cortex. Neuron 104, 1000–1009.e7. doi:10.1016/j.neuron.2019.09.004

Gruenwald, J., Znobishchev, A., Kapeller, C., Kamada, K., Scharinger, J., Guger, C., 2019. Time-Variant Linear Discriminant Analysis Improves Hand Gesture and Finger Movement Decoding for Invasive Brain-Computer Interfaces. Front. Neurosci. 13, 901. doi:10.3389/fnins.2019.00901

Guan, C., Aflalo, T., Kadlec, K., Gámez de Leon, J., Rosario, E.R., Bari, A., Pouratian, N., Andersen, R.A., 2022a. Compositional coding of individual finger movements in human posterior parietal cortex and motor cortex enables ten-finger decoding. medRxiv. doi:10.1101/2022.12.07.22283227

Guan, C., Aflalo, T., Zhang, C.Y., Amoruso, E., Rosario, E.R., Pouratian, N., Andersen, R.A., 2022b. Stability of motor representations after paralysis. Elife 11. doi:10.7554/eLife.74478

Guest, O., Love, B.C., 2017. What the success of brain imaging implies about the neural code. Elife 6. doi:10.7554/eLife.21397

Häger-Ross, C., Schieber, M.H., 2000. Quantifying the independence of human finger movements: comparisons of digits, hands, and movement frequencies. J. Neurosci. 20, 8542–8550.

Haghi, B., Aflalo, T., Kellis, S., Kadlec, K., Pouratian, N., Andersen, R.A., Emami, A., 2021. FENet: Feature Extraction Neural Network for Brain Machine Interfaces. Presented at the Society for Neuroscience Annual Meeting, Society for Neuroscience.

Hall, T.M., de Carvalho, F., Jackson, A., 2014. A common structure underlies low-frequency cortical dynamics in movement, sleep, and sedation. Neuron 83, 1185–1199. doi:10.1016/j.neuron.2014.07.022

Ho, E., Hettick, M., Papageorgiou, D., Poole, A.J., Monge, M., Vomero, M., Gelman, K.R., Hanson, T., Tolosa, V., Mager, M., Rapoport, B.I., 2022. The layer 7 cortical interface: A scalable and minimally invasive brain–computer interface platform. BioRxiv. doi:10.1101/2022.01.02.474656

Ho, J., Tumkaya, T., Aryal, S., Choi, H., Claridge-Chang, A., 2019. Moving beyond P values: data analysis with estimation graphics. Nat. Methods 16, 565–566. doi:10.1038/s41592-019-0470-3

Hochberg, L.R., Bacher, D., Jarosiewicz, B., Masse, N.Y., Simeral, J.D., Vogel, J., Haddadin, S., Liu, J., Cash, S.S., van der Smagt, P., Donoghue, J.P., 2012. Reach and grasp by people with tetraplegia using a neurally controlled robotic arm. Nature 485, 372–375. doi:10.1038/nature11076

Hochberg, L.R., Serruya, M.D., Friehs, G.M., Mukand, J.A., Saleh, M., Caplan, A.H., Branner, A., Chen, D., Penn, R.D., Donoghue, J.P., 2006. Neuronal ensemble control of prosthetic devices by a human with tetraplegia. Nature 442, 164–171. doi:10.1038/nature04970

Hotson, G., McMullen, D.P., Fifer, M.S., Johannes, M.S., Katyal, K.D., Para, M.P., Armiger, R., Anderson, W.S., Thakor, N.V., Wester, B.A., Crone, N.E., 2016. Individual finger control of a modular prosthetic limb using high-density electrocorticography in a human subject. J. Neural Eng. 13, 026017–026017. doi:10.1088/1741-2560/13/2/026017

Hubel, D.H., Wiesel, T.N., 1970. The period of susceptibility to the physiological effects of unilateral eye closure in kittens. J. Physiol. (Lond.) 206, 419–436. doi:10.1113/jphysiol.1970.sp009022

Huggins, J.E., Moinuddin, A.A., Chiodo, A.E., Wren, P.A., 2015. What would brain-computer interface users want: opinions and priorities of potential users with spinal cord injury. Arch. Phys. Med. Rehabil. 96, S38–45.e1. doi:10.1016/j.apmr.2014.05.028

Hwang, E.J., Bailey, P.M., Andersen, R.A., 2013. Volitional control of neural activity relies on the natural motor repertoire. Curr. Biol. 23, 353–361. doi:10.1016/j.cub.2013.01.027

Ingram, J.N., Körding, K.P., Howard, I.S., Wolpert, D.M., 2008. The statistics of natural hand movements. Exp. Brain Res. 188, 223–236. doi:10.1007/s00221-008-1355-3

Inoue, Y., Mao, H., Suway, S.B., Orellana, J., Schwartz, A.B., 2018. Decoding arm speed during reaching. Nat. Commun. 9, 5243. doi:10.1038/s41467-018-07647-3

Irwin, Z.T., Schroeder, K.E., Vu, P.P., Bullard, A.J., Tat, D.M., Nu, C.S., Vaskov, A., Nason, S.R., Thompson, D.E., Bentley, J.N., Patil, P.G., Chestek, C.A., 2017. Neural control of finger movement via intracortical brain-machine interface. J. Neural Eng. 14, 066004. doi:10.1088/1741-2552/aa80bd

Jain, N., Qi, H.-X., Collins, C.E., Kaas, J.H., 2008. Large-scale reorganization in the somatosensory cortex and thalamus after sensory loss in macaque monkeys. J. Neurosci. 28, 11042–11060. doi:10.1523/JNEUROSCI.2334-08.2008

James, G., Witten, D., Hastie, T., Tibshirani, R., 2013. An Introduction to Statistical Learning, Springer Texts in Statistics. Springer New York, New York, NY. doi:10.1007/978-1-4614-7138-7

Jarosiewicz, B., Masse, N.Y., Bacher, D., Cash, S.S., Eskandar, E., Friehs, G., Donoghue, J.P., Hochberg, L.R., 2013. Advantages of closed-loop calibration in intracortical brain-computer interfaces for people with tetraplegia. J. Neural Eng. 10, 046012. doi:10.1088/1741-2560/10/4/046012

Jarosiewicz, B., Sarma, A.A., Bacher, D., Masse, N.Y., Simeral, J.D., Sorice, B., Oakley, E.M., Blabe, C., Pandarinath, C., Gilja, V., Cash, S.S., Eskandar, E.N., Friehs, G., Henderson, J.M., Shenoy, K.V., Donoghue, J.P., Hochberg, L.R., 2015. Virtual typing by people with tetraplegia using a self-calibrating intracortical brain-computer interface. Sci. Transl. Med. 7, 313ra179. doi:10.1126/scitranslmed.aac7328

Johansson, R.S., Flanagan, J.R., 2009. Coding and use of tactile signals from the fingertips in object manipulation tasks. Nat. Rev. Neurosci. 10, 345–359. doi:10.1038/nrn2621

Jorge, A., Royston, D.A., Tyler-Kabara, E.C., Boninger, M.L., Collinger, J.L., 2020. Classification of individual finger movements using intracortical recordings in human motor cortex. Neurosurgery 87, 630–638. doi:10.1093/neuros/nyaa026

Jozwik, K.M., Kriegeskorte, N., Mur, M., 2016. Visual features as stepping stones toward semantics: Explaining object similarity in IT and perception with non-negative least squares. Neuropsychologia 83, 201–226. doi:10.1016/j.neuropsychologia.2015.10.023

Kakei, S., Hoffman, D.S., Strick, P.L., 1999. Muscle and movement representations in the primary motor cortex. Science 285, 2136–2139. doi:10.1126/science.285.5436.2136

Kalidindi, H.T., Cross, K.P., Lillicrap, T.P., Omrani, M., Falotico, E., Sabes, P.N., Scott, S.H., 2021. Rotational dynamics in motor cortex are consistent with a feedback controller. Elife 10. doi:10.7554/eLife.67256

Kambi, N., Halder, P., Rajan, R., Arora, V., Chand, P., Arora, M., Jain, N., 2014. Large-scale reorganization of the somatosensory cortex following spinal cord injuries is due to brainstem plasticity. Nat. Commun. 5, 3602. doi:10.1038/ncomms4602

Kao, J.C., Nuyujukian, P., Ryu, S.I., Churchland, M.M., Cunningham, J.P., Shenoy, K.V., 2015. Single-trial dynamics of motor cortex and their applications to brain-machine interfaces. Nat. Commun. 6, 7759. doi:10.1038/ncomms8759

Karpowicz, B.M., Ali, Y.H., Wimalasena, L.N., Sedler, A.R., Keshtkaran, M.R., Bodkin, K., Ma, X., Miller, L.E., Pandarinath, C., 2022. Stabilizing brain-computer interfaces through alignment of latent dynamics. BioRxiv. doi:10.1101/2022.04.06.487388

Katyal, K.D., Johannes, M.S., Kellis, S., Aflalo, T., Klaes, C., McGee, T.G., Para, M.P., Shi, Y., Lee, B., Pejsa, K., Liu, C., Wester, B.A., Tenore, F., Beaty, J.D., Ravitz, A.D., Andersen, R.A., McLoughlin, M.P., 2014. A collaborative BCI approach to autonomous control of a prosthetic limb system, in: 2014 IEEE International Conference on Systems, Man, and Cybernetics (SMC). Presented at the 2014 IEEE International Conference on Systems, Man and Cybernetics - SMC, IEEE, pp. 1479–1482. doi:10.1109/SMC.2014.6974124

Kaufman, M.T., Churchland, M.M., Ryu, S.I., Shenoy, K.V., 2014. Cortical activity in the null space: permitting preparation without movement. Nat. Neurosci. 17, 440–448. doi:10.1038/nn.3643

Kaufman, M.T., Seely, J.S., Sussillo, D., Ryu, S.I., Shenoy, K.V., Churchland, M.M., 2016. The largest response component in the motor cortex reflects movement timing but not movement type. eNeuro 3. doi:10.1523/ENEURO.0085-16.2016

Keck, T., Mrsic-Flogel, T.D., Vaz Afonso, M., Eysel, U.T., Bonhoeffer, T., Hübener, M., 2008. Massive restructuring of neuronal circuits during functional reorganization of adult visual cortex. Nat. Neurosci. 11, 1162–1167. doi:10.1038/nn.2181

Kieliba, P., Clode, D., Maimon-Mor, R.O., Makin, T.R., 2021. Robotic hand augmentation drives changes in neural body representation. Sci. Robot. 6. doi:10.1126/scirobotics.abd7935

Kietzmann, T.C., Spoerer, C.J., Sörensen, L.K.A., Cichy, R.M., Hauk, O., Kriegeskorte, N., 2019. Recurrence is required to capture the representational dynamics of the human visual system. Proc. Natl. Acad. Sci. USA 116, 21854–21863. doi:10.1073/pnas.1905544116

Kikkert, S., Kolasinski, J., Jbabdi, S., Tracey, I., Beckmann, C.F., Johansen-Berg, H., Makin, T.R., 2016. Revealing the neural fingerprints of a missing hand. Elife 5. doi:10.7554/eLife.15292

Kikkert, S., Pfyffer, D., Verling, M., Freund, P., Wenderoth, N., 2021. Finger somatotopy is preserved after tetraplegia but deteriorates over time. Elife 10. doi:10.7554/eLife.67713

Kim, H., Mnih, A., 2018. Disentangling by factorising. International Conference on Machine Learning 2649.

Kim, S.-P., Simeral, J.D., Hochberg, L.R., Donoghue, J.P., Black, M.J., 2008. Neural control of computer cursor velocity by decoding motor cortical spiking activity in humans with tetraplegia. J. Neural Eng. 5, 455–476. doi:10.1088/1741-2560/5/4/010

Klaes, C., Kellis, S., Aflalo, T., Lee, B., Pejsa, K., Shanfield, K., Hayes-Jackson, S., Aisen, M., Heck, C., Liu, C., Andersen, R.A., 2015. Hand shape representations in the human posterior parietal cortex. J. Neurosci. 35, 15466–15476. doi:10.1523/JNEUROSCI.2747-15.2015

Kleinfeld, D., Luan, L., Mitra, P.P., Robinson, J.T., Sarpeshkar, R., Shepard, K., Xie, C., Harris, T.D., 2019. Can One Concurrently Record Electrical Spikes from Every Neuron in a Mammalian Brain? Neuron 103, 1005–1015. doi:10.1016/j.neuron.2019.08.011

Kobak, D., Brendel, W., Constantinidis, C., Feierstein, C.E., Kepecs, A., Mainen, Z.F., Qi, X.-L., Romo, R., Uchida, N., Machens, C.K., 2016. Demixed principal component analysis of neural population data. Elife 5. doi:10.7554/eLife.10989

Kriegeskorte, N., Diedrichsen, J., 2016. Inferring brain-computational mechanisms with models of activity measurements. Philos. Trans. R. Soc. Lond. B, Biol. Sci. 371. doi:10.1098/rstb.2016.0278

Kriegeskorte, N., Mur, M., Bandettini, P., 2008a. Representational similarity analysis - connecting the branches of systems neuroscience. Front. Syst. Neurosci. 2, 4. doi:10.3389/neuro.06.004.2008

Kriegeskorte, N., Mur, M., Ruff, D.A., Kiani, R., Bodurka, J., Esteky, H., Tanaka, K., Bandettini, P.A., 2008b. Matching categorical object representations in inferior temporal cortex of man and monkey. Neuron 60, 1126–1141. doi:10.1016/j.neuron.2008.10.043

Kriegeskorte, N., Wei, X.-X., 2021. Neural tuning and representational geometry. Nat. Rev. Neurosci. 22, 703–718. doi:10.1038/s41583-021-00502-3

Lang, C.E., Schieber, M.H., 2003. Differential impairment of individuated finger movements in humans after damage to the motor cortex or the corticospinal tract. J. Neurophysiol. 90, 1160–1170. doi:10.1152/jn.00130.2003

Lang, C.E., Schieber, M.H., 2004a. Human finger independence: limitations due to passive mechanical coupling versus active neuromuscular control. J. Neurophysiol. 92, 2802–2810. doi:10.1152/jn.00480.2004

Lang, C.E., Schieber, M.H., 2004b. Reduced muscle selectivity during individuated finger movements in humans after damage to the motor cortex or corticospinal tract. J. Neurophysiol. 91, 1722–1733. doi:10.1152/jn.00805.2003

Lawrence, D.G., Kuypers, H.G., 1968. The functional organization of the motor system in the monkey. I. The effects of bilateral pyramidal lesions. Brain 91, 1–14.

Lebedev, M.A., Ossadtchi, A., Mill, N.A., Urpí, N.A., Cervera, M.R., Nicolelis, M.A.L., 2019. Analysis of neuronal ensemble activity reveals the pitfalls and shortcomings of rotation dynamics. Sci. Rep. 9, 18978. doi:10.1038/s41598-019-54760-4

Ledoit, O., Wolf, M., 2003. Improved estimation of the covariance matrix of stock returns with an application to portfolio selection. Journal of Empirical Finance 10, 603–621. doi:10.1016/S0927-5398(03)00007-0

Li, Y., Wang, Y., Cui, H., 2022. Posterior parietal cortex predicts upcoming movement in dynamic sensorimotor control. Proc. Natl. Acad. Sci. USA 119, e2118903119. doi:10.1073/pnas.2118903119

Lillicrap, T.P., Scott, S.H., 2013. Preference distributions of primary motor cortex neurons reflect control solutions optimized for limb biomechanics. Neuron 77, 168–179. doi:10.1016/j.neuron.2012.10.041

Logothetis, N.K., Pauls, J., Augath, M., Trinath, T., Oeltermann, A., 2001. Neurophysiological investigation of the basis of the fMRI signal. Nature 412, 150–157. doi:10.1038/35084005

Luan, L., Robinson, J.T., Aazhang, B., Chi, T., Yang, K., Li, X., Rathore, H., Singer, A., Yellapantula, S., Fan, Y., Yu, Z., Xie, C., 2020. Recent advances in electrical neural interface engineering: minimal invasiveness, longevity, and scalability. Neuron 108, 302–321. doi:10.1016/j.neuron.2020.10.011

Ma, X., Rizzoglio, F., Perreault, E.J., Miller, L.E., Kennedy, A., 2022. Using adversarial networks to extend brain computer interface decoding accuracy over time. BioRxiv. doi:10.1101/2022.08.26.504777

Makin, T.R., Bensmaia, S.J., 2017. Stability of sensory topographies in adult cortex. Trends Cogn. Sci. (Regul. Ed.) 21, 195–204. doi:10.1016/j.tics.2017.01.002

Mars, R.B., Jbabdi, S., Sallet, J., O'Reilly, J.X., Croxson, P.L., Olivier, E., Noonan, M.P., Bergmann, C., Mitchell, A.S., Baxter, M.G., Behrens, T.E.J., Johansen-Berg, H., Tomassini, V., Miller, K.L., Rushworth, M.F.S., 2011. Diffusion-weighted imaging tractography-based parcellation of the human parietal cortex and comparison with human and macaque resting-state functional connectivity. J. Neurosci. 31, 4087–4100. doi:10.1523/JNEUROSCI.5102-10.2011

McMullen, D.P., Hotson, G., Katyal, K.D., Wester, B.A., Fifer, M.S., McGee, T.G., Harris, A., Johannes, M.S., Vogelstein, R.J., Ravitz, A.D., Anderson, W.S., Thakor, N.V., Crone, N.E., 2014. Demonstration of a semi-autonomous hybrid brain-machine interface using human intracranial EEG, eye tracking, and computer vision to control a robotic upper limb prosthetic. IEEE Trans Neural Syst Rehabil Eng 22, 784–796. doi:10.1109/TNSRE.2013.2294685

McNamee, D., Wolpert, D.M., 2019. Internal models in biological control. Annu. Rev. Control Robot. Auton. Syst. 2, 339–364. doi:10.1146/annurev-control-060117-105206

Merzenich, M.M., Nelson, R.J., Stryker, M.P., Cynader, M.S., Schoppmann, A., Zook, J.M., 1984. Somatosensory cortical map changes following digit amputation in adult monkeys. J. Comp. Neurol. 224, 591–605. doi:10.1002/cne.902240408

Miall, R.C., Rosenthal, O., Ørstavik, K., Cole, J.D., Sarlegna, F.R., 2019. Loss of haptic feedback impairs control of hand posture: a study in chronically deafferented individuals when grasping and lifting objects. Exp. Brain Res. 237, 2167–2184. doi:10.1007/s00221-019-05583-2

Michaels, J.A., Schaffelhofer, S., Agudelo-Toro, A., Scherberger, H., 2020. A goal-driven modular neural network predicts parietofrontal neural dynamics during grasping. Proc. Natl. Acad. Sci. USA 117, 32124–32135. doi:10.1073/pnas.2005087117

Michaels, J.A., Scherberger, H., 2018. Population coding of grasp and laterality-related information in the macaque fronto-parietal network. Sci. Rep. 8, 1710. doi:10.1038/s41598-018-20051-7

Moran, D.W., Schwartz, A.B., 1999. Motor cortical representation of speed and direction during reaching. J. Neurophysiol. 82, 2676–2692. doi:10.1152/jn.1999.82.5.2676

Morey, R.D., Rouder, J.N., Jamil, T., Morey, M.R., 2015. Package "bayesfactor". URLh http://cran/r-projectorg/web/packages/BayesFactor/BayesFactor pdf i (accessed 1006 15).

Morey, R.D., Wagenmakers, E.-J., 2014. Simple relation between Bayesian order-restricted and point-null hypothesis tests. Stat Probab Lett 92, 121–124. doi:10.1016/j.spl.2014.05.010

Moritz, C.T., Fetz, E.E., 2011. Volitional control of single cortical neurons in a brain-machine interface. J. Neural Eng. 8, 025017. doi:10.1088/1741-2560/8/2/025017

Moses, D.A., Metzger, S.L., Liu, J.R., Anumanchipalli, G.K., Makin, J.G., Sun, P.F., Chartier, J., Dougherty, M.E., Liu, P.M., Abrams, G.M., Tu-Chan, A., Ganguly, K., Chang, E.F., 2021. Neuroprosthesis for Decoding Speech in a Paralyzed Person with Anarthria. N. Engl. J. Med. 385, 217–227. doi:10.1056/NEJMoa2027540

Muelling, K., Venkatraman, A., Valois, J.-S., Downey, J.E., Weiss, J., Javdani, S., Hebert, M., Schwartz, A.B., Collinger, J.L., Bagnell, J.A., 2017. Autonomy infused teleoperation with application to brain computer interface controlled manipulation. Auton. Robots 41, 1401–1422. doi:10.1007/s10514-017-9622-4

Mulliken, G.H., Musallam, S., Andersen, R.A., 2008a. Forward estimation of movement state in posterior parietal cortex. Proc. Natl. Acad. Sci. USA 105, 8170–8177. doi:10.1073/pnas.0802602105

Mulliken, G.H., Musallam, S., Andersen, R.A., 2008b. Decoding trajectories from posterior parietal cortex ensembles. J. Neurosci. 28, 12913–12926. doi:10.1523/JNEUROSCI.1463-08.2008

Murata, A., Gallese, V., Luppino, G., Kaseda, M., Sakata, H., 2000. Selectivity for the shape, size, and orientation of objects for grasping in neurons of monkey parietal area AIP. J. Neurophysiol. 83, 2580–2601. doi:10.1152/jn.2000.83.5.2580

Musk, E., Neuralink, 2019. An Integrated Brain-Machine Interface Platform With Thousands of Channels. J. Med. Internet Res. 21, e16194. doi:10.2196/16194

Nardone, R., Höller, Y., Brigo, F., Seidl, M., Christova, M., Bergmann, J., Golaszewski, S., Trinka, E., 2013. Functional brain reorganization after spinal cord injury: systematic review of animal and human studies. Brain Res. 1504, 58–73. doi:10.1016/j.brainres.2012.12.034

Nashed, J.Y., Crevecoeur, F., Scott, S.H., 2014. Rapid online selection between multiple motor plans. J. Neurosci. 34, 1769–1780. doi:10.1523/JNEUROSCI.3063-13.2014

Nason, S.R., Mender, M.J., Vaskov, A.K., Willsey, M.S., Ganesh Kumar, N., Kung, T.A., Patil, P.G., Chestek, C.A., 2021. Real-time linear prediction of simultaneous and independent movements of two finger groups using an intracortical brain-machine interface. Neuron 109, 3164–3177.e8. doi:10.1016/j.neuron.2021.08.009

Nili, H., Wingfield, C., Walther, A., Su, L., Marslen-Wilson, W., Kriegeskorte, N., 2014. A toolbox for representational similarity analysis. PLoS Comput. Biol. 10, e1003553. doi:10.1371/journal.pcbi.1003553

Nuyujukian, P., Albites Sanabria, J., Saab, J., Pandarinath, C., Jarosiewicz, B., Blabe, C.H., Franco, B., Mernoff, S.T., Eskandar, E.N., Simeral, J.D., Hochberg, L.R., Shenoy, K.V., Henderson, J.M., 2018. Cortical control of a tablet computer by people with paralysis. PLoS One 13, e0204566. doi:10.1371/journal.pone.0204566

Nuyujukian, P., Fan, J.M., Kao, J.C., Ryu, S.I., Shenoy, K.V., 2015. A high-performance keyboard neural prosthesis enabled by task optimization. IEEE Trans. Biomed. Eng. 62, 21–29. doi:10.1109/TBME.2014.2354697

Nuyujukian, P., Kao, J.C., Fan, J.M., Stavisky, S.D., Ryu, S.I., Shenoy, K.V., 2014. Performance sustaining intracortical neural prostheses. J. Neural Eng. 11, 066003. doi:10.1088/1741-2560/11/6/066003

O'Shea, D.J., Duncker, L., Goo, W., Sun, X., Vyas, S., Trautmann, E.M., Diester, I., Ramakrishnan, C., Deisseroth, K., Sahani, M., Shenoy, K.V., 2022. Direct neural perturbations reveal a dynamical mechanism for robust computation. BioRxiv. doi:10.1101/2022.12.16.520768

Oby, E.R., Golub, M.D., Hennig, J.A., Degenhart, A.D., Tyler-Kabara, E.C., Yu, B.M., Chase, S.M., Batista, A.P., 2019. New neural activity patterns emerge with long-term learning. Proc. Natl. Acad. Sci. USA 116, 15210–15215. doi:10.1073/pnas.1820296116

Omrani, M., Kaufman, M.T., Hatsopoulos, N.G., Cheney, P.D., 2017. Perspectives on classical controversies about the motor cortex. J. Neurophysiol. 118, 1828–1848. doi:10.1152/jn.00795.2016

Orban, G.A., Caruana, F., 2014. The neural basis of human tool use. Front. Psychol. 5, 310. doi:10.3389/fpsyg.2014.00310

Orsborn, A.L., Moorman, H.G., Overduin, S.A., Shanechi, M.M., Dimitrov, D.F., Carmena, J.M., 2014. Closed-loop decoder adaptation shapes neural plasticity for skillful neuroprosthetic control. Neuron 82, 1380–1393. doi:10.1016/j.neuron.2014.04.048

Overduin, S.A., d Avella, A., Carmena, J.M., Bizzi, E., 2012. Microstimulation activates a handful of muscle synergies. Neuron 76, 1071–1077. doi:10.1016/j.neuron.2012.10.018

Pandarinath, C., Ames, K.C., Russo, A.A., Farshchian, A., Miller, L.E., Dyer, E.L., Kao, J.C., 2018a. Latent Factors and Dynamics in Motor Cortex and Their Application to Brain-Machine Interfaces. J. Neurosci. 38, 9390–9401. doi:10.1523/JNEUROSCI.1669-18.2018

Pandarinath, C., Gilja, V., Blabe, C.H., Nuyujukian, P., Sarma, A.A., Sorice, B.L., Eskandar, E.N., Hochberg, L.R., Henderson, J.M., Shenoy, K.V., 2015. Neural population dynamics in human motor cortex during movements in people with ALS. Elife 4, e07436. doi:10.7554/eLife.07436

Pandarinath, C., Nuyujukian, P., Blabe, C.H., Sorice, B.L., Saab, J., Willett, F.R., Hochberg, L.R., Shenoy, K.V., Henderson, J.M., 2017. High performance communication by people with paralysis using an intracortical brain-computer interface. Elife 6. doi:10.7554/eLife.18554

Pandarinath, C., O'Shea, D.J., Collins, J., Jozefowicz, R., Stavisky, S.D., Kao, J.C., Trautmann, E.M., Kaufman, M.T., Ryu, S.I., Hochberg, L.R., Henderson, J.M., Shenoy, K.V., Abbott, L.F., Sussillo, D., 2018b. Inferring single-trial neural population dynamics using sequential auto-encoders. Nat. Methods 15, 805–815. doi:10.1038/s41592-018-0109-9

Paninski, L., Fellows, M.R., Hatsopoulos, N.G., Donoghue, J.P., 2004. Spatiotemporal tuning of motor cortical neurons for hand position and velocity. J. Neurophysiol. 91, 515–532. doi:10.1152/jn.00587.2002

Penfield, W., Boldrey, E., 1937. Somatic motor and sensory representation in the cerebral cortex of man as studied by electrical stimulation. Brain 60, 389–443. doi:10.1093/brain/60.4.389

Perge, J.A., Homer, M.L., Malik, W.Q., Cash, S., Eskandar, E., Friehs, G., Donoghue, J.P., Hochberg, L.R., 2013. Intra-day signal instabilities affect decoding performance in an intracortical neural interface system. J. Neural Eng. 10, 036004. doi:10.1088/1741-2560/10/3/036004

Pons, T.P., Garraghty, P.E., Cusick, C.G., Kaas, J.H., 1985. The somatotopic organization of area 2 in macaque monkeys. J. Comp. Neurol. 241, 445–466. doi:10.1002/cne.902410405

Pons, T.P., Garraghty, P.E., Ommaya, A.K., Kaas, J.H., Taub, E., Mishkin, M., 1991. Massive cortical reorganization after sensory deafferentation in adult macaques. Science 252, 1857–1860. doi:10.1126/science.1843843

Pruszynski, J.A., Flanagan, J.R., Johansson, R.S., 2018. Fast and accurate edge orientation processing during object manipulation. Elife 7. doi:10.7554/eLife.31200

Qi, H.X., Stepniewska, I., Kaas, J.H., 2000. Reorganization of primary motor cortex in adult macaque monkeys with long-standing amputations. J. Neurophysiol. 84, 2133–2147. doi:10.1152/jn.2000.84.4.2133

Rathelot, J.-A., Dum, R.P., Strick, P.L., 2017. Posterior parietal cortex contains a command apparatus for hand movements. Proc. Natl. Acad. Sci. USA 114, 4255–4260. doi:10.1073/pnas.1608132114

Rathelot, J.-A., Strick, P.L., 2009. Subdivisions of primary motor cortex based on cortico-motoneuronal cells. Proc. Natl. Acad. Sci. USA 106, 918–923. doi:10.1073/pnas.0808362106

Rolls, E.T., Deco, G., Huang, C.-C., Feng, J., 2022. The human posterior parietal cortex: effective connectome, and its relation to function. Cereb. Cortex. doi:10.1093/cercor/bhac266

Russo, A.A., Bittner, S.R., Perkins, S.M., Seely, J.S., London, B.M., Lara, A.H., Miri, A., Marshall, N.J., Kohn, A., Jessell, T.M., Abbott, L.F., Cunningham, J.P., Churchland, M.M., 2018. Motor Cortex Embeds Muscle-like Commands in an Untangled Population Response. Neuron 97, 953–966.e8. doi:10.1016/j.neuron.2018.01.004

Russo, A.A., Khajeh, R., Bittner, S.R., Perkins, S.M., Cunningham, J.P., Abbott, L.F., Churchland, M.M., 2020. Neural Trajectories in the Supplementary Motor Area and Motor Cortex Exhibit Distinct Geometries, Compatible with Different Classes of Computation. Neuron 107, 745–758.e6. doi:10.1016/j.neuron.2020.05.020

Rutishauser, U., Aflalo, T., Rosario, E.R., Pouratian, N., Andersen, R.A., 2018. Single-Neuron Representation of Memory Strength and Recognition Confidence in Left Human Posterior Parietal Cortex. Neuron 97, 209–220.e3. doi:10.1016/j.neuron.2017.11.029

Sachs, N.A., Ruiz-Torres, R., Perreault, E.J., Miller, L.E., 2016. Brain-state classification and a dual-state decoder dramatically improve the control of cursor movement through a brain-machine interface. J. Neural Eng. 13, 016009. doi:10.1088/1741-2560/13/1/016009

Sadtler, P.T., Quick, K.M., Golub, M.D., Chase, S.M., Ryu, S.I., Tyler-Kabara, E.C., Yu, B.M., Batista, A.P., 2014. Neural constraints on learning. Nature 512, 423–426. doi:10.1038/nature13665

Sainburg, R.L., Ghilardi, M.F., Poizner, H., Ghez, C., 1995. Control of limb dynamics in normal subjects and patients without proprioception. J. Neurophysiol. 73, 820–835.

Sakellaridi, S., Christopoulos, V.N., Aflalo, T., Pejsa, K.W., Rosario, E.R., Ouellette, D., Pouratian, N., Andersen, R.A., 2019. Intrinsic Variable Learning for Brain-Machine Interface Control by Human Anterior Intraparietal Cortex. Neuron 102, 694–705.e3. doi:10.1016/j.neuron.2019.02.012

Sani, O.G., Abbaspourazad, H., Wong, Y.T., Pesaran, B., Shanechi, M.M., 2021. Modeling behaviorally relevant neural dynamics enabled by preferential subspace identification. Nat. Neurosci. 24, 140–149. doi:10.1038/s41593-020-00733-0

Sauerbrei, B.A., Guo, J.-Z., Cohen, J.D., Mischiati, M., Guo, W., Kabra, M., Verma, N., Mensh, B., Branson, K., Hantman, A.W., 2020. Cortical pattern generation during dexterous movement is input-driven. Nature 577, 386–391. doi:10.1038/s41586-019-1869-9

Saxena, S., Russo, A.A., Cunningham, J., Churchland, M.M., 2022. Motor cortex activity across movement speeds is predicted by network-level strategies for generating muscle activity. Elife 11. doi:10.7554/eLife.67620

Schaffelhofer, S., Scherberger, H., 2016. Object vision to hand action in macaque parietal, premotor, and motor cortices. Elife 5. doi:10.7554/eLife.15278

Schellekens, W., Petridou, N., Ramsey, N.F., 2018. Detailed somatotopy in primary motor and somatosensory cortex revealed by Gaussian population receptive fields. Neuroimage 179, 337–347. doi:10.1016/j.neuroimage.2018.06.062

Schellekens, W., Thio, M., Badde, S., Winawer, J., Ramsey, N., Petridou, N., 2021. A touch of hierarchy. Population Receptive Fields reveal fingertip integration in Brodmann areas in human primary somatosensory cortex. BioRxiv. doi:10.1101/2021.01.15.426783

Scheperjans, F., Eickhoff, S.B., Hömke, L., Mohlberg, H., Hermann, K., Amunts, K., Zilles, K., 2008. Probabilistic maps, morphometry, and variability of cytoarchitectonic areas in the human superior parietal cortex. Cereb. Cortex 18, 2141–2157. doi:10.1093/cercor/bhm241

Schieber, M.H., 1991. Individuated finger movements of rhesus monkeys: a means of quantifying the independence of the digits. J. Neurophysiol. 65, 1381–1391. doi:10.1152/jn.1991.65.6.1381

Schieber, M.H., 2001. Constraints on somatotopic organization in the primary motor cortex. J. Neurophysiol. 86, 2125–2143. doi:10.1152/jn.2001.86.5.2125

Schieber, M.H., Hibbard, L.S., 1993. How somatotopic is the motor cortex hand area? Science 261, 489–492. doi:10.1126/science.8332915

Schieber, M.H., Poliakov, A.V., 1998. Partial inactivation of the primary motor cortex hand area: effects on individuated finger movements. J. Neurosci. 18, 9038–9054.

Schmitzer-Torbert, N., Jackson, J., Henze, D., Harris, K., Redish, A.D., 2005. Quantitative measures of cluster quality for use in extracellular recordings. Neuroscience 131, 1–11. doi:10.1016/j.neuroscience.2004.09.066

Schütt, H.H., Lin, B., Diedrichsen, J., Kriegeskorte, N., 2019. Python Representational Similarity Analysis toolbox (rsatoolbox). GitHub.

Scott, S.H., 2004. Optimal feedback control and the neural basis of volitional motor control. Nat. Rev. Neurosci. 5, 532–546. doi:10.1038/nrn1427

Scott, S.H., 2008. Inconvenient truths about neural processing in primary motor cortex. J. Physiol. (Lond.) 586, 1217–1224. doi:10.1113/jphysiol.2007.146068

Scott, S.H., 2016. A Functional Taxonomy of Bottom-Up Sensory Feedback Processing for Motor Actions. Trends Neurosci. 39, 512–526. doi:10.1016/j.tins.2016.06.001

Seelke, A.M.H., Padberg, J.J., Disbrow, E., Purnell, S.M., Recanzone, G., Krubitzer, L., 2012. Topographic Maps within Brodmann's Area 5 of macaque monkeys. Cereb. Cortex 22, 1834–1850. doi:10.1093/cercor/bhr257

Serruya, M.D., Hatsopoulos, N.G., Paninski, L., Fellows, M.R., Donoghue, J.P., 2002. Instant neural control of a movement signal. Nature 416, 141–142. doi:10.1038/416141a

Shadmehr, R., Krakauer, J.W., 2008. A computational neuroanatomy for motor control. Exp. Brain Res. 185, 359–381. doi:10.1007/s00221-008-1280-5

Shadmehr, R., Smith, M.A., Krakauer, J.W., 2010. Error correction, sensory prediction, and adaptation in motor control. Annu. Rev. Neurosci. 33, 89–108. doi:10.1146/annurev-neuro-060909-153135

Shanechi, M.M., 2016. Brain-Machine interface control algorithms. IEEE Trans Neural Syst Rehabil Eng. doi:10.1109/TNSRE.2016.2639501

Shanechi, M.M., Orsborn, A.L., Carmena, J.M., 2016. Robust Brain-Machine Interface Design Using Optimal Feedback Control Modeling and Adaptive Point Process Filtering. PLoS Comput. Biol. 12, e1004730. doi:10.1371/journal.pcbi.1004730

Shanechi, M.M., Orsborn, A.L., Moorman, H.G., Gowda, S., Dangi, S., Carmena, J.M., 2017. Rapid control and feedback rates enhance neuroprosthetic control. Nat. Commun. 8, 13825. doi:10.1038/ncomms13825

Shenoy, K.V., Sahani, M., Churchland, M.M., 2013. Cortical control of arm movements: a dynamical systems perspective. Annu. Rev. Neurosci. 36, 337–359. doi:10.1146/annurev-neuro-062111-150509

Simone, L., Viganò, L., Fornia, L., Howells, H., Leonetti, A., Puglisi, G., Bellacicca, A., Bello, L., Cerri, G., 2021. Distinct functional and structural connectivity of the human hand-knob supported by intraoperative findings. J. Neurosci. doi:10.1523/JNEUROSCI.1574-20.2021

Singh, A., Tetreault, L., Kalsi-Ryan, S., Nouri, A., Fehlings, M.G., 2014. Global prevalence and incidence of traumatic spinal cord injury. Clin Epidemiol 6, 309–331. doi:10.2147/CLEP.S68889

Smirnakis, S.M., Brewer, A.A., Schmid, M.C., Tolias, A.S., Schüz, A., Augath, M., Inhoffen, W., Wandell, B.A., Logothetis, N.K., 2005. Lack of long-term cortical reorganization after macaque retinal lesions. Nature 435, 300–307. doi:10.1038/nature03495

Snoek, G.J., IJzerman, M.J., Hermens, H.J., Maxwell, D., Biering-Sorensen, F., 2004. Survey of the needs of patients with spinal cord injury: impact and priority for improvement in hand function in tetraplegics. Spinal Cord 42, 526–532. doi:10.1038/sj.sc.3101638

Snyder, L.H., Batista, A.P., Andersen, R.A., 1997. Coding of intention in the posterior parietal cortex. Nature 386, 167–170. doi:10.1038/386167a0

Sobinov, A.R., Bensmaia, S.J., 2021. The neural mechanisms of manual dexterity. Nat. Rev. Neurosci. 22, 741–757. doi:10.1038/s41583-021-00528-7

Sollmann, N., Bulubas, L., Tanigawa, N., Zimmer, C., Meyer, B., Krieg, S.M., 2017. The variability of motor evoked potential latencies in neurosurgical motor mapping by preoperative navigated transcranial magnetic stimulation. BMC Neurosci. 18, 5. doi:10.1186/s12868-016-0321-4

Stavisky, S.D., 2016. Advancing Motor Neural Prosthesis Robustness and Neuroscience. Stanford University.

Stavisky, S.D., Kao, J.C., Nuyujukian, P., Pandarinath, C., Blabe, C., Ryu, S.I., Hochberg, L.R., Henderson, J.M., Shenoy, K.V., 2018. Brain-machine interface cursor position only weakly affects monkey and human motor cortical activity in the absence of arm movements. Sci. Rep. 8, 16357. doi:10.1038/s41598-018-34711-1

Stavisky, S.D., Kao, J.C., Ryu, S.I., Shenoy, K.V., 2017a. Trial-by-Trial Motor Cortical Correlates of a Rapidly Adapting Visuomotor Internal Model. J. Neurosci. 37, 1721–1732. doi:10.1523/JNEUROSCI.1091-16.2016

Stavisky, S.D., Kao, J.C., Ryu, S.I., Shenoy, K.V., 2017b. Motor Cortical Visuomotor Feedback Activity Is Initially Isolated from Downstream Targets in Output-Null Neural State Space Dimensions. Neuron 95, 195–208.e9. doi:10.1016/j.neuron.2017.05.023

Stavisky, S.D., Willett, F.R., Wilson, G.H., Murphy, B.A., Rezaii, P., Avansino, D.T., Memberg, W.D., Miller, J.P., Kirsch, R.F., Hochberg, L.R., Ajiboye, A.B., Druckmann, S., Shenoy, K.V., Henderson, J.M., 2019. Neural ensemble dynamics in dorsal motor cortex during speech in people with paralysis. Elife 8. doi:10.7554/eLife.46015

Suresh, A.K., Goodman, J.M., Okorokova, E.V., Kaufman, M., Hatsopoulos, N.G., Bensmaia, S.J., 2020. Neural population dynamics in motor cortex are different for reach and grasp. Elife 9. doi:10.7554/eLife.58848

Sussillo, D., Churchland, M.M., Kaufman, M.T., Shenoy, K.V., 2015. A neural network that finds a naturalistic solution for the production of muscle activity. Nat. Neurosci. 18, 1025–1033. doi:10.1038/nn.4042

Sussillo, D., Nuyujukian, P., Fan, J.M., Kao, J.C., Stavisky, S.D., Ryu, S., Shenoy, K., 2012. A recurrent neural network for closed-loop intracortical brain-machine interface decoders. J. Neural Eng. 9, 026027. doi:10.1088/1741-2560/9/2/026027

Sussillo, D., Stavisky, S.D., Kao, J.C., Ryu, S.I., Shenoy, K.V., 2016. Making brain-machine interfaces robust to future neural variability. Nat. Commun. 7, 13749. doi:10.1038/ncomms13749

Taylor, D.M., Tillery, S.I.H., Schwartz, A.B., 2002. Direct cortical control of 3D neuroprosthetic devices. Science 296, 1829–1832. doi:10.1126/science.1070291

Tibshirani, R., Walther, G., Hastie, T., 2001. Estimating the number of clusters in a data set via the gap statistic. J Royal Statistical Soc B 63, 411–423. doi:10.1111/1467-9868.00293

Todorov, E., Jordan, M.I., 2002. Optimal feedback control as a theory of motor coordination. Nat. Neurosci. 5, 1226–1235. doi:10.1038/nn963

Tunik, E., Ortigue, S., Adamovich, S.V., Grafton, S.T., 2008. Differential recruitment of anterior intraparietal sulcus and superior parietal lobule during visually guided grasping revealed by electrical neuroimaging. J. Neurosci. 28, 13615–13620. doi:10.1523/JNEUROSCI.3303-08.2008

Velliste, M., Kennedy, S.D., Schwartz, A.B., Whitford, A.S., Sohn, J.-W., McMorland, A.J.C., 2014. Motor cortical correlates of arm resting in the context of a reaching task and implications for prosthetic control. J. Neurosci. 34, 6011–6022. doi:10.1523/JNEUROSCI.3520-13.2014

Velliste, M., Perel, S., Spalding, M.C., Whitford, A.S., Schwartz, A.B., 2008. Cortical control of a prosthetic arm for self-feeding. Nature 453, 1098–1101. doi:10.1038/nature06996

Versteeg, C., Miller, L., 2022. Dynamical feedback control: motor cortex as an optimal feedback controller based on neural dynamics. doi:10.20944/preprints202201.0428.v1

Vyas, S., Even-Chen, N., Stavisky, S.D., Ryu, S.I., Nuyujukian, P., Shenoy, K.V., 2018. Neural population dynamics underlying motor learning transfer. Neuron 97, 1177–1186.e3. doi:10.1016/j.neuron.2018.01.040

Vyas, S., Golub, M.D., Sussillo, D., Shenoy, K.V., 2020. Computation through neural population dynamics. Annu. Rev. Neurosci. 43, 249–275. doi:10.1146/annurev-neuro-092619-094115

Walther, A., Nili, H., Ejaz, N., Alink, A., Kriegeskorte, N., Diedrichsen, J., 2016. Reliability of dissimilarity measures for multi-voxel pattern analysis. Neuroimage 137, 188–200. doi:10.1016/j.neuroimage.2015.12.012

Wandelt, Sarah K., Bjånes, D.A., Pejsa, K., Lee, B., Liu, C., Andersen, R.A., 2022. Online internal speech decoding from single neurons in a human participant. medRxiv. doi:10.1101/2022.11.02.22281775

Wandelt, Sarah K, Kellis, S., Bjånes, D.A., Pejsa, K., Lee, B., Liu, C., Andersen, R.A., 2022. Decoding grasp and speech signals from the cortical grasp circuit in a tetraplegic human. Neuron 110, 1777–1787.e3. doi:10.1016/j.neuron.2022.03.009

Wang, J., Yang, Y., Fan, L., Xu, J., Li, C., Liu, Y., Fox, P.T., Eickhoff, S.B., Yu, C., Jiang, T., 2015. Convergent functional architecture of the superior parietal lobule unraveled with multimodal neuroimaging approaches. Hum. Brain Mapp. 36, 238–257. doi:10.1002/hbm.22626

Wang, W., Collinger, J.L., Degenhart, A.D., Tyler-Kabara, E.C., Schwartz, A.B., Moran, D.W., Weber, D.J., Wodlinger, B., Vinjamuri, R.K., Ashmore, R.C., Kelly, J.W., Boninger, M.L., 2013. An electrocorticographic brain interface in an individual with tetraplegia. PLoS One 8, e55344. doi:10.1371/journal.pone.0055344

Weiler, J., Gribble, P.L., Pruszynski, J.A., 2019. Spinal stretch reflexes support efficient hand control. Nat. Neurosci. 22, 529–533. doi:10.1038/s41593-019-0336-0

Wessberg, J., Stambaugh, C.R., Kralik, J.D., Beck, P.D., Laubach, M., Chapin, J.K., Kim, J., Biggs, S.J., Srinivasan, M.A., Nicolelis, M.A., 2000. Real-time prediction of hand trajectory by ensembles of cortical neurons in primates. Nature 408, 361–365. doi:10.1038/35042582

Wesselink, D.B., van den Heiligenberg, F.M., Ejaz, N., Dempsey-Jones, H., Cardinali, L., Tarall-Jozwiak, A., Diedrichsen, J., Makin, T.R., 2019. Obtaining and maintaining cortical hand representation as evidenced from acquired and congenital handlessness. Elife 8. doi:10.7554/eLife.37227

Whitlock, J.R., 2017. Posterior parietal cortex. Curr. Biol. 27, R691–R695. doi:10.1016/j.cub.2017.06.007

Willett, F.R., Avansino, D.T., Hochberg, L.R., Henderson, J.M., Shenoy, K.V., 2021. High-performance brain-to-text communication via handwriting. Nature 593, 249–254. doi:10.1038/s41586-021-03506-2

Willett, F.R., Deo, D.R., Avansino, D.T., Rezaii, P., Hochberg, L.R., Henderson, J.M., Shenoy, K.V., 2020. Hand knob area of premotor cortex represents the whole body in a compositional way. Cell 181, 396–409.e26. doi:10.1016/j.cell.2020.02.043

Willett, F., Kunz, E., Fan, C., Avansino, D., Wilson, G., Choi, E.Y., Kamdar, F., Hochberg, L.R., Druckmann, S., Shenoy, K.V., Henderson, J.M., 2023. A high-performance speech neuroprosthesis. BioRxiv. doi:10.1101/2023.01.21.524489

Willett, F.R., Murphy, B.A., Memberg, W.D., Blabe, C.H., Pandarinath, C., Walter, B.L., Sweet, J.A., Miller, J.P., Henderson, J.M., Shenoy, K.V., Hochberg, L.R., Kirsch, R.F., Ajiboye, A.B., 2017a. Signal-independent noise in intracortical brain-computer interfaces causes movement time properties inconsistent with Fitts' law. J. Neural Eng. 14, 026010. doi:10.1088/1741-2552/aa5990

Willett, F.R., Murphy, B.A., Young, D.R., Memberg, W.D., Blabe, C.H., Pandarinath, C., Franco, B., Saab, J., Walter, B.L., Sweet, J.A., Miller, J.P., Henderson, J.M., Shenoy, K.V., Simeral, J.D., Jarosiewicz, B., Hochberg, L.R., Kirsch, R.F., Ajiboye, A.B., 2018. A Comparison of Intention Estimation Methods for Decoder Calibration in Intracortical Brain-Computer Interfaces. IEEE Trans. Biomed. Eng. 65, 2066–2078. doi:10.1109/TBME.2017.2783358

Willett, F.R., Pandarinath, C., Jarosiewicz, B., Murphy, B.A., Memberg, W.D., Blabe, C.H., Saab, J., Walter, B.L., Sweet, J.A., Miller, J.P., Henderson, J.M., Shenoy, K.V., Simeral, J.D., Hochberg, L.R., Kirsch, R.F., Ajiboye, A.B., 2017b. Feedback control policies employed by people using intracortical brain-computer interfaces. J. Neural Eng. 14, 016001. doi:10.1088/1741-2560/14/1/016001

Willett, F.R., Young, D.R., Murphy, B.A., Memberg, W.D., Blabe, C.H., Pandarinath, C., Stavisky, S.D., Rezaii, P., Saab, J., Walter, B.L., Sweet, J.A., Miller, J.P., Henderson, J.M., Shenoy, K.V., Simeral, J.D., Jarosiewicz, B., Hochberg, L.R., Kirsch, R.F., Bolu Ajiboye, A., 2019. Principled BCI decoder design and parameter selection using a feedback control model. Sci. Rep. 9, 8881. doi:10.1038/s41598-019-44166-7

Willsey, M.S., Nason-Tomaszewski, S.R., Ensel, S.R., Temmar, H., Mender, M.J., Costello, J.T., Patil, P.G., Chestek, C.A., 2022. Real-time brain-machine interface in non-human primates achieves high-velocity prosthetic finger movements using a shallow feedforward neural network decoder. Nat. Commun. 13, 6899. doi:10.1038/s41467-022-34452-w

Wodlinger, B., Downey, J.E., Tyler-Kabara, E.C., Schwartz, A.B., Boninger, M.L., Collinger, J.L., 2015. Ten-dimensional anthropomorphic arm control in a human brain-machine interface: difficulties, solutions, and limitations. J. Neural Eng. 12, 016011. doi:10.1088/1741-2560/12/1/016011

Wolpert, D.M., Goodbody, S.J., Husain, M., 1998. Maintaining internal representations: the role of the human superior parietal lobe. Nat. Neurosci. 1, 529–533. doi:10.1038/2245

Wu, W., Shaikhouni, A., Donoghue, J.P., Black, M.J., 2004. Closed-loop neural control of cursor motion using a Kalman filter. Conf. Proc. IEEE Eng. Med. Biol. Soc. 2004, 4126–4129. doi:10.1109/IEMBS.2004.1404151

Yan, Y., Goodman, J.M., Moore, D.D., Solla, S.A., Bensmaia, S.J., 2020. Unexpected complexity of everyday manual behaviors. Nat. Commun. 11, 3564. doi:10.1038/s41467-020-17404-0

Yousry, T.A., Schmid, U.D., Alkadhi, H., Schmidt, D., Peraud, A., Buettner, A., Winkler, P., 1997. Localization of the motor hand area to a knob on the precentral gyrus. A new landmark. Brain 120 (Pt 1), 141–157. doi:10.1093/brain/120.1.141

Zhang, C.Y., Aflalo, T., Revechkis, B., Rosario, E.R., Ouellette, D., Pouratian, N., Andersen, R.A., 2017. Partially mixed selectivity in human posterior parietal association cortex. Neuron 95, 697–708.e4. doi:10.1016/j.neuron.2017.06.040